Report No. IITRI-A6088-22

(Final Report, Volume II)

PREDICTION OF NEUTRON INDUCED ACTIVATION
VOLUME II - NAP: PHYSICAL MODELS AND
EXPERIMENTAL VALIDATION

May 14, 1964 through January 31, 1966

Contract No. NAS8-11160
Control No. DCN 1-4-50-01014-01 & S1(1F)
CPB 02-1058064
IITRI Project A6088

Prepared by

David A. Klopp

IIT RESEARCH INSTITUTE
Technology Center
Chicago, Illinois 60616

for

George C. Marshall Space Flight Center
National Aeronautics and Space Administration
Huntsville, Alabama 35812

Attention: PR-EC

Report No. IITRI-A6088-22
(Final Report, Volume II)

PREDICTION OF NEUTRON INDUCED ACTIVATION
VOLUME II - NAP: PHYSICAL MODELS AND
EXPERIMENTAL VALIDATION

Prepared by

David A. Klopp

IIT RESEARCH INSTITUTE
Technology Center
Chicago, Illinois 60616

for

George C. Marshall Space Flight Center
National Aeronautics and Space Administration
Huntsville, Alabama 35812

Attention: PR-EC

FOREWORD

This is Report No. IITRI-A6088-22 of IITRI Project A6088, Contract No. NAS8-11160, entitled "Prediction of Neutron Induced Activation, Volume II - NAP: Physical Models and Experimental Validation." The report covers the period from May 14, 1964, through January 31, 1966.
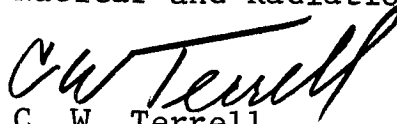
Personnel who made significant contributions to the research reported here include Dr. Gerald Hardie and Dr. Daniel Sperber, who were instrumental in piecing together the (n,p), (n,α), and (n,2n) cross section calculation model, Alvin R. Brauner, who supervised the reactor irradiations, and Donald T. Krebes, who supervised the Van de Graaff irradiations.

<div style="margin-left: 40%;">

Respectfully submitted,
IIT RESEARCH INSTITUTE

D. A. Klopp
Research Physicist

</div>

Approved by:

T. G. Stinchcomb
Acting Manager
Nuclear and Radiation Physics Section

C. W. Terrell
Director
Physics Research

/jh

ABSTRACT

PREDICTION OF NEUTRON INDUCED ACTIVATION
VOLUME II - NAP: PHYSICAL MODELS AND
EXPERIMENTAL VALIDATION

An IBM 7094 computer program was written for the pre-
diction of neutron induced activation. This report describes
the physical models which form the basis for the computer pro-
gramming and the experimental validation of the computer program.
The physical models discussed here include one-dimensional
neutron transport, estimation of neutron activation cross
sections, and time dependence of radioisotope atomic concen-
trations. The experimental validation compares computed
results of the NAP code, including neutron flux distribution,
cross section calculation, and neutron induced gamma ray source
strengths, to experimental data obtained here and from other
laboratories.

TABLE OF CONTENTS

LIST OF TABLES

LIST OF TABLES
(Continued)

LIST OF FIGURES

LIST OF FIGURES
(Continued)

LIST OF FIGURES
(Continued)

A6088 FINAL REPORT

VOLUME II

I.   <u>INTRODUCTION</u>

This volume presents the important physical models used
in the NAP (Neutron Activation Prediction) computer code and
the experimental validation of these models. The NAP program
calculates the neutron induced activation of materials exposed
to any specified neutron flux. This includes the energy
spectrum and intensity of gamma rays emitted during deactivation.
A brief description of the workings of the code, required input
and output, together with flow charts of the calculation, is
given in Volume I - "NAP Code Manual" of this final report series.
A description and listing of the NAP Cross Section Library is
given in Volume III. A similar discussion and listing of the
NAP Gamma Radiation Library is given in Volume IV.

Those portions of the NAP program which required extensive
physical analysis are discussed in this volume. These include
calculation of neutron cross sections, the effect of neutron
self-shielding, and isotopic concentrations as a function of
time. Also discussed in this volume is the experimental
validation of the NAP computer program.

II. PHYSICAL MODELS

A. Synopsis of NAP Program

Volume I of this final report series presents a description of the general structure and computational details of the NAP (Neutron Activation Prediction) computer code, which computes gamma-ray source strengths, doses, and dose rates due to neutron induced activation of materials. This section is an abridgment of that description. Its purpose is to further understanding of the physical models used in the computer code.

A known neutron flux spectrum combined with an intensity normalization describes the neutron flux incident upon the activated materials. The intensity normalization may be time-dependent, but the energy spectrum is assumed to be independent of time. The multigroup neutron flux input is automatically adjusted to be compatible with the neutron energy group boundaries inherent in the NAP Cross Section Library, thus providing maximum flexibility in the definition of the neutron spectrum. The adjustment conserves the flux spectrum integrated over neutron energy. If the activated regions are optically thick, in terms of neutron mean free paths, or if the position where the flux spectrum is given is optically far from the activated materials, the NAP code generates a multigroup neutron transport solution producing spatially-averaged multigroup fluxes for each distinct spatial region. This transport calculation is described fully in Section II-B of this volume. The time dependence of the neutron flux is specified by a series of power normalization factors constant over any specified time interval.

Each spatial region has a uniform, time-dependent isotopic composition. In each region, all of the pertinent decay chains are formulated by a search of the NAP Gamma Radiation Library. The NAP Cross Section Library provides neutron cross sections for most stable isotopes which are decay chain parents. If the required cross sections are

absent from the library, the NAP program will provide an estimation of the desired (n,γ), (n,p), (n,α) and $(n,2n)$ cross sections. The physical models used in the estimation are described in Section II-C of this volume. Using the product of neutron flux and cross section, neutron reaction rates are computed for each decay chain parent. Production and loss rates of daughter isotopes are obtained from half-lives and branching ratios tabulated in the Gamma Radiation Library. The atomic concentration of each isotope in the decay chain is traced out in time using the technique discussed in Section II-D.

The Gamma Radiation Library provides gamma ray energies and relative emission probabilities for all well-known gamma ray emitters. This information is combined with isotopic atom densities to compute gamma ray source strengths as a function of time for each decay chain in each region. The multigroup gamma ray energy boundaries used in the calculations are specified by the problem originator. A regional source strength is computed by summing over all of the decay chains in a given region. Finally, a simple dose and dose rate calculation, ignoring gamma ray attenuation and buildup in materials other than air, is performed for an arbitrary detector position. By proper definition of the desired gamma ray calculations, the NAP output may be used directly as input for most of the common gamma ray attenuation codes.

The above synopsis shows the importance of the neutron transport solution, the cross section calculation, and the computation of radioisotopic atom densities and how these calculations fit into the general structure of the NAP code. Prior to the computer programming, detailed physical analysis of these three basic problems was required. That analysis is reported here. The programming resulting from the analysis is discussed in Volume I.

B.   Neutron Transport in the NAP Code

The NAP program provides a solution for a particular multigroup neutron transport problem. The problem is constrained to treat a maximum of 43 neutron energy groups and a maximum of 20 spatial regions described in one-dimensional plane or spherical geometry. A maximum of 100 spatial mesh points may be used. The forward components of the multigroup angular fluxes at the left or incident boundary are specified as input data. The backward components of the multigroup angular fluxes at the right or exit boundary are assumed to vanish (vacuum boundary condition). A maximum of 10 angular components (5 forward and 5 backward) is permitted. Up-scattering is forbidden, and down-scattering is permitted only to the adjacent neutron energy group. Each region is chemically homogeneous and physically isotropic, and all neutron scattering is isotropic. The problem analysis given here will describe the monoenergetic solution in plane geometry, the monoenergetic solution in spherical geometry, and finally the extension to the multigroup solution.

1.   Monoenergetic Solution in Plane Geometry

The monoenergetic steady-state Boltzmann transport equation applicable to a homogeneous, isotropic medium may be written (ref. 1)

$$\mu \frac{\partial \psi(x,\mu)}{\partial x} + \Sigma_t \psi(x,\mu) = \frac{1}{2}\Sigma_s \int_{-1}^{1} \psi(x,\mu')d\mu' + S(x,\mu) \qquad (1)$$

Plane geometry and isotropic neutron scattering are assumed. Here $\psi(x,\mu)$ is the angular neutron flux, i.e. the number of neutrons per unit volume at the position x, per unit angle traveling in the direction $\cos^{-1}\mu$ with respect to the positive x-axis, multiplied by the neutron speed. $S(x,\mu)$ is a source term, while Σ_s and Σ_t are the macroscopic scattering and total

4

cross sections, respectively, In a multi-region problem, Σ_s and Σ_t are step functions of position.

No exact, explicit solution of equation (1) is known in a finite medium, although various approximate methods have been applied. The spherical harmonics method of solution (ref. 2) is to expand the angular flux and source in a series of Legendre functions trancated at some order L. The resulting solution for the angular flux is called the P_L approximation. Problems in which there is a strong forward bias require a large number of terms in the expansion to obtain the angular flux with reasonable accuracy. Furthermore, the boundary conditions described above cannot be represented simply in the spherical harmonics method. Carlson's S_n method (ref. 3) is to divide the integral from -1 to +1 in equation (1) into n intervals and assume that $\psi(x,\mu)$ varies linearly with μ in each interval. The desired boundary conditions are simple using this method; however no Fortran S_n computer program was found utilizing these boundary conditions.

The NAP neutron transport solution is based on the Wick-Chandrasekhar discrete ordinate method (refs. 3, 4). The integral in equation (1) is approximated by the Legendre-Gauss quadrature formula

$$\int_{-1}^{1} \psi(x,\mu)\,d\mu = \sum_{k=1}^{2N} a_k \psi(x,\mu_k) \tag{2}$$

where the μ_k are the roots of $P_{2N}(\mu) = 0$, and the weights a_k are given by

$$a_k = \frac{1}{N P_{2N-1}(\mu_k) P'_{2N}(\mu_k)} \tag{3}$$

Here $P_{2N-1}(\mu_k)$ is the Legendre polynomial of order 2N-1 and argument μ_k, while the prime denotes differentiation with respect to the argument. The weights and ordinates are given in Table 1 for up to N = 5. The approximation is exact if $\psi(x,\mu)$ is a polynomial of degree $\leq$ 4N-1 in μ. In case a plane collimated neutron beam is incident upon the left boundary, it is useful to have an ordinate at μ = 1. Instead of Legendre-Gauss quadrature, Lobatto quadrature may be used. The formalism is unchanged, but the ordinates and weights differ from those above, and are given in Table 2.

In either case, equation (1) yields the 2N equations

$$\mu_j \frac{\partial \psi(x,\mu_j)}{\partial x} + \Sigma_t \psi(x,\mu_j) = \frac{1}{2} \Sigma_s \sum_{k=1}^{2N} a_k \psi(x,\mu_k) + S(x,\mu_j) \quad (4)$$

for j = 1,2,---,2N. The ordinates and weights are numbered such that

$$\mu_j = -\mu_{N+j} \qquad j = 1,2,\ldots,N \qquad (5)$$

$$a_j = a_{N+j} \qquad j = 1,2,\ldots,N \qquad (6)$$

$$-1 \leq \mu_N < \mu_{N-1} < \ldots < \mu_1 < 0 < \mu_{N+1} < \mu_{N+2} < \ldots < \mu_{2N} \leq 1 \quad (7)$$

If

$$\psi_j(x) = \psi(x,\mu_j) \qquad (8)$$

$$S_j(x) = S(x,\mu_j) \qquad (9)$$

equation (4) becomes

$$\left(\mu_j \frac{d}{dx} + \Sigma_t \right) \psi_j(x) = \frac{1}{2} \Sigma_s \sum_{k=1}^{2N} a_k \psi_k(x) + S_j(x) \qquad (10)$$

Table 1

ORDINATES AND WEIGHTS FOR LEGENDRE-GAUSS QUADRATURE

N	Ordinates (μ_j)	Weights (a_j)
1	$\pm$ 0.5773503	1.0
2	$\pm$ 0.3399810	0.6521452
	$\pm$ 0.8611363	0.3478548
3	$\pm$ 0.2386192	0.4679139
	$\pm$ 0.6612094	0.3607616
	$\pm$ 0.9324695	0.2074006
4	$\pm$ 0.1834346	0.3626838
	$\pm$ 0.5255324	0.3137066
	$\pm$ 0.7966665	0.2223810
	$\pm$ 0.9602899	0.1012285
5	$\pm$ 0.1488743	0.2955242
	$\pm$ 0.4333954	0.2692667
	$\pm$ 0.6794097	0.2190864
	$\pm$ 0.8650634	0.1494514
	$\pm$ 0.9739065	0.0666713

Table 2

ORDINATES AND WEIGHTS FOR LOBATTO QUADRATURE

N	Ordinates (μ_j)	Weights (a_j)
2	$\pm$ 0.447214	5/6
	$\pm$ 1.0	1/6
3	$\pm$ 0.285232	0.554858
	$\pm$ 0.765055	0.378475
	$\pm$ 1.0	0.066667

with the boundary conditions

$$\psi_j(0) \quad \begin{cases} = 0 \text{ for } j = 1,2,\ldots N \\[2em] \text{given for } j = N+1, \ldots, 2N \end{cases}$$

$$\psi_j(L) \quad = 0 \text{ for } j = 1,2,\ldots,N \tag{12}$$

where L is the position of the right boundary.

Following Wilf (ref. 5), the first step in the solution is to define recursively

$$S_j^{(0)}(x) = S_j(x) \tag{13}$$

$$\left(\mu_j \, \frac{d}{dx} + \Sigma_t\right) \psi_j^{(0)}(x) = S_j^{(0)}(x) \tag{14}$$

$$S_j^{(n+1)}(x) = \frac{1}{2} \Sigma_s \sum_{k=1}^{2N} a_k \psi_k^{(n)} + S_j(x) \tag{15}$$

$$\left(\mu_j \, \frac{d}{dx} + \Sigma_t\right) \psi_j^{(n+1)}(x) = S_j^{(n+1)}(x) \tag{16}$$

Convergence of this process is assured in any subcritical medium. The spatial integration of equation (16) has been given by Wilf as

$$\psi_j(x_{m+1}) = \sigma\psi_j(x_m) + W_oS_j(x_m) + W_1S_j(x_{m+1}) \tag{17}$$

where

$$\sigma = \exp\left(-h \, \Sigma_t/\mu_j\right) \tag{18}$$

$$W_o = \frac{1}{\Sigma_t} \left[\frac{\mu_j}{h\Sigma_t} (1 - \sigma) - \sigma \right] \qquad (19)$$

$$W_1 = \frac{1}{\Sigma_t} \left[\frac{\mu_j}{h\Sigma_t} (\sigma - 1) + 1 \right] \qquad (20)$$

The x_m are the spatial mesh points and h is the mesh interval.
The superscripts have been ignored for convenience. The
factors σ, W_o, and W_1 are constant throughout any given region.
Equation (17) is useful for advancing the solution from the
left boundary in the direction of increasing x. A similar
equation may be obtained for advancing the solution from the
right boundary, i.e.

$$\psi_j(x_m) = \frac{1}{\sigma} \left[\psi(x_{m+1}) - W_o S_j(x_m) - W_1 S_j(x_{m+1}) \right] \qquad (21)$$

The NAP program does not provide for a source term
$S(x,\mu)$. It has been included here because it is useful in
the extension to multigroup theory. In general, the procedure
is to use equations (17) and (21) with $S_j^{(0)}(x_n) = S_j(x_n)$ to
obtain first order solutions $\psi_j^{(0)}(x_n)$ for all j. This first
order solution is substituted into equation (15) yielding a
new set of source terms $S_j^{(1)}(x_n)$. These new source terms are
used in equations (17) and (21) to obtain second order solutions
$\psi_j^{(1)}(x_n)$ for all j and n. At the end of each iteration, the
total flux at the right boundary

$$\phi^{(n)}(L) = \int_{-1}^{1} \psi(L,\mu) \, d\mu = \sum_{k=N+1}^{2N} a_k \psi_k(L) \qquad (22)$$

is computed and compared with $\phi^{(n-1)}(L)$. When the fractional
change from one iteration to the next is smaller than some

preassigned convergence criterion, the iteration is halted, and the problem is regarded as solved.

2. Monoenergetic Solution in Spherical Geometry

Goertzel (ref. 6) has extended the discrete ordinate method to spherical geometry. The extension is based upon a comparison of the discrete ordinate equations to the spherical harmonic equations. In spherical geometry, with isotropic neutron scattering, the monoenergetic steady-state transport equation is (ref. 1)

$$\mu \frac{\partial \psi(r,\mu)}{\partial r} + \Sigma_t \psi(r,\mu) + \frac{1-\mu^2}{r} \frac{\partial \psi(r,\mu)}{\partial \mu} = \frac{1}{2} \Sigma_s \int_{-1}^{1} \psi(r,\mu') d\mu' + S(r,\mu) \tag{23}$$

This equation is analogous to equation (1) above. The discrete ordinate form of equation (23) is

$$\left(\mu_j \frac{d}{dr} + \Sigma_t\right)\psi_j(r) + \frac{1}{r} \sum_{k=1}^{2N} K_{jk}\psi_k(r) = \frac{1}{2} \Sigma_s \cdot \sum_{k=1}^{2N} a_k\psi_k(r) + S_j(r) \tag{24}$$

Goertzel, by comparing equation (24) to the spherical harmonics form of equation (23), has shown that for Legendre-Gauss quadrature the K_{jk} are

$$K_{jk} = \frac{2N^2 P_{2N-1}(\mu_j) P_{2N-1}(\mu_k) a_k}{\mu_j - \mu_k} \tag{25}$$

for the off-diagonal elements, and

$$K_{jj} = \mu_j \tag{26}$$

for the diagonal elements.

The procedure used in the plane geometry solution may be employed here by redefining the source term in equation (15) as

$$S_j^{(n+1)}(x) = \frac{1}{2} \Sigma_s \sum_{k=1}^{2N} a_k \psi_k^{(n)}(x) - \frac{1}{x} \sum_{k=1}^{2N} K_{jk} \psi_k(x) + S_j(x)$$

(27)

where now x is the radial coordinate. The rest of the procedure then follows as before.

The extension to cylindrical geometry is considerably more difficult and has not been attempted.

3.   Multigroup Solution

The energy-dependent steady-state Boltzmann equation in a plane homogeneous isotropic medium is (ref. 1)

$$\mu \frac{\partial}{\partial x} \psi(x,E,\mu) + \Sigma_t(E) \psi(x,E,\mu) = \int \Sigma_s(E' \to E, \underline{\Omega}' \to \Omega) \psi(x,E',\underline{\Omega}') dE' d\underline{\Omega}'$$

(28)

with no external sources. Here E is the neutron energy and Σ_s (E'→E,$\underline{\Omega}$'→Ω) is the cross section per unit energy per unit solid angle for changing the neutron energy and direction E', $\underline{\Omega}$' into an energy and direction range dE, d$\underline{\Omega}$ at E,$\underline{\Omega}$. The vector $\underline{\Omega}$ is a unit vector in the direction of neutron velocity. The cross sections are step functions of position x. If the scattering is isotropic,

$$\Sigma_s (E' \to E, \underline{\Omega}' \to \underline{\Omega}) = \frac{1}{4\pi} \Sigma_s(E' \to E)$$

(29)

and equation (28) reduces to

$$\frac{d}{dx} \psi(x,E,\mu) + \Sigma_t(E) \psi(x,E,\mu) = 1/2 \int_{-1}^{1} d\mu \int dE' \Sigma_s(E' \to E) \psi(x,E',\mu')$$

(30)

12

The multigroup method divides the entire neutron energy range into contiguous energy groups. The energy groups are numbered in order of decreasing energy such that the energy limits of group g are E_{g-1} and E_g. The angular flux in each energy group may be described in terms of the group angular flux.

$$\psi_g(x,\mu) = \int_{E_g}^{E_{g-1}} \psi(x,E',\mu)dE' \qquad (31)$$

for the energy group g. Forbidding all energy transfers other than from group g to group g+1, equation (30) becomes

$$\mu \frac{d}{dx}\psi_g(x,\mu) + \Sigma_{g,t}\psi_g(x,\mu) = \frac{1}{2}\Sigma_{g,g}\int_{-1}^{1}\psi_g(x,\mu')d\mu' +$$

$$\frac{1}{2}\Sigma_{g-1,g}\int_{-1}^{1}\psi_{g-1}(x,\mu')d\mu' \qquad (32)$$

Here $\Sigma_{g,t}$ is the total cross section in energy group g, $\Sigma_{g,g}$ is the scattering cross section which does not result in any group transfers, and $\Sigma_{g-1,g}$ is the cross section for neutron slowing-down from group g-1 into group g.

The discrete ordinate technique then gives

$$\left(\mu_j \frac{d}{dx} + \Sigma_{g,t}\right)\psi_g(x,\mu_j) = \frac{1}{2}\Sigma_{g,g}\sum_{k=1}^{2N} a_k\psi_g(x,\mu_k) +$$

$$\frac{1}{2}\Sigma_{g-1,g}\sum_{\ell=1}^{2N} a_\ell\psi_{g-1}(x,\mu_\ell) \qquad (33)$$

13

This has the same form as equation (10) with the slowing-down term acting as a source. Thus the same procedure may be used to solve equation (33). In particular, the process starts by solving for the first group angular flux, which is independent of any slowing down source. The first group flux then provides a slowing down source for the second group flux, and a solution is obtained for the second group flux. This process is repeated until all the group angular fluxes are obtained. The convergence criterion used by the NAP program is neutron energy group-independent. At the completion of the neutron transport problem, spatially averaged neutron energy group fluxes are computed for each region. These average group fluxes are used in computing reaction rates as described in section II-D.

The accuracy and reliability of the discrete ordinate solution of the neutron transport problem is discussed in section III-A.

C.   Cross Section Calculations in the NAP Code

1.   Calculation of (n,p), (n,α), and (n,2n) Cross Sections

Neutron activation is determined by the product of a reaction cross section and neutron flux integrated over energy and, hence, the cross section must be known over a wide energy range for use with a variety of neutron spectra. Since only a few (n,p), (n,α), and (n,2n) cross sections are well-known for energies up to 20 MeV, the NAP program includes subroutines which will calculate these cross sections as a function of energy. Measured (n,p), (n,α), and (n,2n) cross sections are tabulated in the NAP Cross Section Library where available.

The calculation of cross sections uses simple, approximate techniques suggested by Blatt and Weisskopf (ref. 8) and by Moore (ref. 9) and utilized previously by Ringle (ref. 10). The cross sections are written as

$$\sigma(n,b) = \sigma_{cn}(E_n)G(b,E_n) \tag{34}$$

where $\sigma(n,b)$ is the cross section for the (n,b) reaction, $\sigma_{cn}(E_n)$ is the cross section for formation of a compound nucleus by a neutron of energy E_n bombarding the target nucleus, and $G(b,E_n)$ is the compound nucleus branching ratio. Here b represents the emitted particles: p,α, or 2n. The continuum, or strong-interaction, model of the nucleus predicts $\sigma_{cn}(E_n)$ reasonably well for neutron energies greater than one MeV (ref. 8); the statistical model predicts $G(b,E_n)$ reasonably well for neutron energies up to 20 MeV, where direct reaction processes become important (ref. 9).

a.) Compound Nucleus Formation by Neutrons

The compound nucleus formation cross section $\sigma_{cn}(E_n)$ may be written as (ref. 8)

15

$$\sigma_{cn}(E_n) = \frac{\pi R^2}{x^2} \sum_{\ell=0}^{\infty} (2\ell+1)T_{\ell}(E_n) \tag{35}$$

where the $T_{\ell}(E_n)$ are transmission coefficients and x is kR, k being the relative wave number of the incoming neutron, R the nuclear radius. These are

$$k = \left(\frac{2M_n E_n}{\hbar^2}\right)^{1/2} \quad cm^{-1} \tag{36}$$

$$R = 1.5 \times 10^{-13} A^{1/3} \quad cm \tag{37}$$

with M_n the reduced mass of neutron and target nucleus and A the mass number of the target nucleus.

The transmission coefficients $T_{\ell}(E_n)$ are

$$T_{\ell}(E_n) = \frac{4xXV_{\ell}}{x^2 + xV_{\ell}(2X + xV'_{\ell})} \tag{38}$$

with $X = KR$, $K^2 = K_o^2 + k^2$, and $K_o = 10^{13}$ cm^{-1}. The V_{ℓ} and V'_{ℓ} are (ref. 10)

$$V_{\ell}(x) = \left[f^2_{\ell + \frac{1}{2}}(x) + g^2_{\ell + \frac{1}{2}}(x) \right]^{-1} \tag{39}$$

$$V'_{\ell}(x) = x^2 f^2_{\ell + \frac{1}{2}}(x) + x^2 g^2_{\ell - \frac{1}{2}}(x) + \ell^2 f^2_{\ell + \frac{1}{2}}(x) + \ell^2 g^2_{\ell + \frac{1}{2}}(x)$$

$$- 2x\ell f_{\ell - \frac{1}{2}}(x) f_{\ell + \frac{1}{2}}(x) - 2x\ell g_{\ell - \frac{1}{2}}(x) g_{\ell + \frac{1}{2}}(x) \tag{40}$$

The f and g functions are given by

$$f_{\frac{1}{2}}(x) = 1, \qquad\qquad f_{\frac{3}{2}}(x) = 1/x \qquad\qquad (41)$$

$$g_{\frac{1}{2}}(x) = 0, \qquad\qquad g_{\frac{3}{2}}(x) = 1 \qquad\qquad (42)$$

and the recursion relations

$$f_{n+1}(x) = \frac{2n}{x} f_n(x) - f_{n-1}(x) \qquad\qquad (43)$$

$$g_{n+1}(x) = \frac{2n}{x} g_n(x) - g_{n-1}(x) \qquad\qquad (44)$$

In practice, the infinite series indicated in equation (35) must be terminated at some value of ℓ. Blatt and Weisskopf (op. cit.) indicate that for large values of x, more and more terms must be included for reasonable accuracy. Thus the NAP program performs the summation from $\ell = 0$ to $\ell = L$, where L is the smallest integer larger than $4 + x$, but, in no case, larger than 15. Other schemes of determining L have been tested, but none produce significantly different results.

b.) Compound Nucleus Branching Ratio

Using the statistical model (ref. 9), the branching ratio is

$$G(b, E_n) = \frac{F^*(b)}{F(p) + F(\alpha) + F(n)} \qquad\qquad (45)$$

where F(b) is the relative probability that the compound nucelus decays by emission of particle b, and $F^*(b)$ is the

relative probability that the compound nucleus decays by emission of particle b only. The distinction between $F(b)$ and $F^*(b)$ is that $F^*(b)$ relates to emission of particle b only, while $F(b)$ relates to emission of particle (b) possibly followed by emission of a neutron, if sufficient energy is left in the residual nucleus after emission of the first particle. If this distinction is ignored, (n,bn) reactions are not accounted for, leading to error at energies above the threshold for the (n,bn) reaction.

The emission probabilities are given by

$$F(p) = \frac{2M_p}{\hbar^2} \int_0^{E_n+Q_{np}} \sigma_{cp}(E')\rho(E_n+Q_{np}-E')\, E'dE' \tag{46}$$

$$F(\alpha) = \frac{2M_\alpha}{\hbar^2} \int_0^{E_n+Q_{n\alpha}} \sigma_{c\alpha}(E')\rho(E_n+Q_{n\alpha}-E')E'dE' \tag{47}$$

$$F(n) = \frac{2M_n}{\hbar^2} \int_0^{E_n} \sigma_{cn}(E')\rho(E_n-E')E'dE' \tag{48}$$

$$F^*(p) = \frac{2M_p}{\hbar^2} \int_{\epsilon_p}^{E_n+Q_{np}} \sigma_{cp}(E')\rho(E_n+Q_{np}-E')E'dE' \tag{49}$$

$$F^*(\alpha) = \frac{2M_\alpha}{\hbar^2} \int_{\epsilon_\alpha}^{E_n+Q_{n\alpha}} \sigma_c(E')\rho(E_n+Q_{n\alpha}-E')E'dE' \tag{50}$$

$$F^*(2n) = \frac{2M_n}{\hbar^2} \int_0^{E_n-B_n} \sigma_{cn}(E')\rho(E_n-E')E'dE' \tag{51}$$

where

M_b = reduced mass of the particle b and the target nucleus,

Q_{nb} = target nucleus Q value for the (n,b) reaction,

B_n = neutron binding energy in the target nucleus,

ϵ_b = minimum energy with which particle b can be emitted without leaving sufficient excitation energy to emit a neutron,

σ_{cb} = cross section for formation of compound nucleus by particle b bombarding the residual nucleus, and

$\rho(E)$ = residual nucleus level density at energy E.

The quantity ϵ_b is computed in a straightforward manner, if various Q values and binding energies are known. Let E_b^* be the threshold energy for the (n,bn) reaction. In particular,

$$E_p^* = B_p - Q_{np} \tag{52}$$

$$E_\alpha^* = B_\alpha - Q_{n\alpha} \tag{53}$$

where B_p is the neutron binding energy in the residual nucleus after a proton is emitted, and B_α is the neutron binding energy in the residual nucleus after an alpha particle is emitted. For incident neutron energies below the threshold energy E_b^*, there is no (n,bn) reaction, thus ϵ_b vanishes, and $F^*(b)$ is equal to F(b). On the other hand, for incident neutron energies greater than E_b^*, the (n,bn) reaction is possible, and

$$\epsilon_b = E_n - E_b^* \tag{54}$$

The remaining factors in the emission probability expressions are computed as detailed below.

19

c.) Compound Nucleus Formation by Protons and Alpha Particles

Compound nucleus formation cross sections can be obtained (ref. 8) by solving the wave equation for the incoming particle relative to the nucleus and applying appropriate boundary conditions at the nuclear surface. For incoming neutrons, the solutions to the wave equation can be expressed in terms of relatively simple functions. For incoming charged particles, the solutions to the wave equation are Coulomb wave functions which cannot be expressed in terms of elementary functions. Computer subroutines for the evaluation of Coulomb wave functions and subsequent computation of compound nucleus formation cross sections could be incorporated into the NAP program, but the required subroutines would use considerably more computer storage space and operating time than required for the case of incident neutrons. For this reason, the NAP subroutines for the evaluation of compound nucleus formation cross sections due to proton and alpha particle bombardment rely on tabular interpolations of previously calculated cross sections and asymptotic expressions.

The tabulated compound nucleus formation cross sections for incident protons and alpha particles contained in the NAP program were derived from the tables of Blatt and Weisskopf (op. cit.). The Blatt and Weisskopf tables present cross sections as a function of atomic number and the quantity Y, defined as the ratio of incident particle energy to barrier height. These tables cover the range $Y \leqslant 1.8$, while the asymptotic formula

$$\sigma_c \simeq \pi(R + \lambda)^2 \left[1 - \frac{R}{(R + \lambda)Y} \right] \qquad (55)$$

is valid only for $Y \gg 1$. In computing the compound nucleus formation cross section of the residual nucleus, with the target nucleus specified by Z and A, the quantities appearing

in equation (55) are:

1. incident protons

$$R = 1.5 \times A^{1/3} \quad \text{fermis}$$

$$B = 1.442 \ (Z-1)/R \ \text{MeV}$$

$$Y = E/B$$

$$\lambda = \cfrac{\hbar}{\left(2 \ \cfrac{M_p A}{A+1} \cdot E\right)^{1/2}}$$

M_p = proton mass = 1.6742×10^{-24} gm

2. incident alpha particles:

$$R = 1.2 + 1.5 \ (A-3)^{1/3} \quad \text{fermis}$$

$$B = 2.884 \ (Z-2)/R \quad \text{MeV}$$

$$Y = E/B$$

$$\lambda = \cfrac{\hbar}{\left(2 \ \cfrac{M_\alpha(A-3)}{A-1} \cdot E\right)^{1/2}}$$

M_α = alpha particle mass = 6.6442×10^{-24} gm

The asymptotic formula is used for $Y > 4$ in the case of protons and for $Y > 3$ in the case of alpha particles. The Blatt and Weisskopf tabulated cross section values were extended smoothly to the asymptotic values and values from these smooth cruves are used in this transition region.

d.) Level Density

The nuclear level density $\rho(E)$ of the residual nucleus is required in the evaluation of the emission probabilities as

given by equations (46-51) above. The NAP program uses the Fermi gas model (ref. 8) for the level density, i.e.,

$$\rho(e) = Ce^{2\sqrt{aE}} \tag{56}$$

where the coefficients C and $\underline{a}$ depend upon the mass and neutron-proton character of the residual nucleus.

Blatt and Weisskopf (ref. 8) give values of C for odd-A residual nuclei. Ringle (ref. 10) has noted a sharp break in Blatt and Weisskopf's data at A=115, and fits these data by least-squares technique to obtain

$$C(odd\text{-}A) = 0.6441 - 0.0054 \text{ A MeV}^{-1} \text{ for } A \leqslant 115 \tag{57}$$

$$C(odd\text{-}A) = 0.3459 - 0.00013 \text{ A MeV}^{-1} \text{ for } A > 115 \tag{58}$$

where A is the mass number of the residual nucleus. For even-A residual nuclei, Bullock and Moore (ref. 11) have suggested

$$C(odd\text{-}N, odd\text{-}Z) = 2 \text{ } C(odd\text{-}A) \tag{59}$$

$$C(even\text{-}N, even\text{-}Z) = 0.2 \text{ } C(odd\text{-}A) \tag{60}$$

El-Nadi and Wafik (ref. 12) have shown that the coefficient $\underline{a}$ is approximately 0.03A. These values of $\underline{a}$ differ significantly from those given by Blatt and Weisskopf (ref. 8). According to Bullock and Moore (ref. 11), the results of El-Nadi and Wafik are probably better than those of Blatt and Weisskopf in the high mass number region. Ringle (ref. 10) has fitted the Blatt and Weisskopf data in the low mass number region by least squares techniques to obtain

$$a = 0.1825 - 0.0033A + 0.0005 \text{ A}^2 . \text{ MeV}^{-1} \tag{61}$$

where A is the mass number of the residual nucleus. The NAP program uses equation (61 for $A \leq 62$ and uses the El-Nadi and Wafik approximation for $A > 62$.

e.) Q Values and Neutron Binding Energies

The necessary Q values are obtained by using the Wing-Fong mass excess formula (ref. 13). That is, the mass excess $M(Z,A)$ in a nucleus of Z protons and mass number A is given in MeV by

$$M(Z,A) = 0.0089794A^2 - 2.0717A + 33.448$$
$$+ (Z-Z_A)^2 \left[1.629 - (30.11/A^{1/2}) + 215.8/A \right] \quad (62)$$
$$+ (11.51 \, \delta/A^{1/2}) - S$$

where

$$Z_A = A(1 + 0.003 A)/(2 + 0.01 A) \quad (63)$$

$$\delta = \begin{cases} 0 & \text{for odd A} \\ -1 & \text{for even Z, even A} \\ +1 & \text{for odd Z, even A} \end{cases} \quad (64)$$

$$S = \sum_i \frac{a_i(b_i^2 + c_i^2)}{(A-Z-N_i^*)^2 + b_i^2 + c_i^2} + \sum_j \frac{a_j(b_j^2 + c_j^2)}{(Z-Z_j^*)^2 + b_j^2 + c_j^2)} \quad (65)$$

The values of the constants appearing in equation (65) are given in Table 3.

The Q values are calculated from energy balance using the mass excesses,

$$Q(n,p) = 0.7822 + M(Z,A) - M(Z-1,A) \quad (66)$$
$$Q(n,\alpha) = 5.6474 + M(Z,A) - M(Z-2,A-3) \quad (67)$$
$$Q(n,2n) = M(Z,A) - M(Z,A-1) - 8.071 \quad (68)$$

Table 3

CONSTANTS FOR USE IN WING-FONG MASS EXCESS FORMULA

N_i	$A-Z-N_i^*$	a_i	b_i	c_i
28	+	3.49	4.04	0
28	−	3.49	0	1.44
50	+	5.99	5.96	0
50	−	5.99	0	2.88
82	+	5.75	2.49	0
82	−	5.75	0	5.32
126	+	7.76	2.90	0
126	−	7.76	0	5.36
152	+	5.02	6.88	0
152	−	5.02	0	5.29

z_j^*	$Z-z_j^*$	a_j	b_j	c_j
28	+	3.07	2.27	0
28	−	3.07	0	2.27
50	+	2.74	4.31	0
50	−	2.74	0	3.10
82	+	4.22	1.51	0
82	−	4.22	0	2.35

where the Z and A refer to the target nucleus.

Similarly, the neutron binding energies required in equations (51), (52), and (53) are calculated from

$$B_n = - Q(n,2n) \tag{69}$$

$$B_p = 8.071 - M(Z-1,A) + M(Z-1,A-1) \tag{70}$$

$$B_\alpha = 8.071 - M(Z-2,A-3) + M(Z-2,A-4) \tag{71}$$

In summary, the (n,p), (n,α), and (n,2n) cross sections are regarded as the product of the neutron compound nucleus formation cross section and the branching ratio as stated in equation (34). The cross section for compound nucleus formation by incident neutrons is computed using equation (35), while the branching ratio is determined by equation (45) using emission probabilities. The emission probabilities are calculated using equations (46-51). The required cross sections for compound nucleus formation by protons and alpha particles are obtained by interpolation from the tables of Blatt and Weisskopf (ref. 8) or by asymptotic formulae at higher energies. The level densities are computed from the Fermi gas expression, equation (56), while the Q values and neutron binding energies are calculated from the Wing-Fong mass excess formula, equation (62), and energy balance considerations. The validity of this cross section calculation formalism is discussed in section III.

2. Calculation of (n,γ) Cross Section

Two quite different types of (n,γ) cross section calculations are performed by the NAP program. These are computations of effective (n,γ) cross sections in the resolved resonance region when the resonance parameters are known, and estimation of thermal and epithermal (n,γ) cross sections when no cross section information is available.

25

a.) Effective Epithermal (n,γ) Cross Section

Special treatment of large (n,γ) cross section resonances is often required to obtain accurate activation-produced source strengths. Large values of the (n,γ) cross section and strong energy dependence of the cross section result in a neutron flux depletion in the vicinity of the resonance. Although this depletion, or self-shielding, could be handled adequately by the multigroup neutron transport subroutines available in the NAP program, sufficient accuracy would be achieved only by using a finely detailed description of the neutron flux, both as a function of space and of energy. A far more efficient procedure is to utilize special techniques, which have been developed elsewhere, for the solution of this problem.

Effective (n,γ) group cross sections may be written in terms of effective resonance integrals, i.e.,

$$\sigma_g(n,\gamma) = \frac{\sum_i RI_i}{\int_{E_g}^{E_{g-1}} \frac{dE}{E}} + \sigma_g(1/v) \tag{72}$$

Here $\sigma_g(n,\gamma)$ is the effective (n,γ) cross section for energy group g having the energy limits E_{g-1} and E_g, RI_i is the effective resonance integral for the $i\underline{th}$ resonance and the summation is performed over all the resonances in energy group g, and $\sigma_g(1/v)$ is the non-resonance contribution to the group (n,γ) cross section. This non-resonance contribution is generally regarded as having a 1/v energy variation, where v is the neutron velocity. It is assumed throughout this discussion that the neutron flux per unit energy has been normalized to 1/E in the absence of a resonance.

26

The effective resonance integral may be calculated in terms of known resonance parameters for each resonance: the resonance energy E_o, a statistical factor g, the capture width Γ_γ, the fission width Γ_f, and the neutron width Γ_n. Resonance parameters for selected isotopes are contained in the NAP Cross Section Library. A maximum of nine resonances is permitted for each isotope. The non-resonance contribution, $\sigma_g(1/v)$, is also tabulated in the library. The nomenclature of fission width Γ_f has been used here; however in most cases the quantity actually tabulated in the library as Γ_f is not the fission width, but a capture width as defined below. This arises because in many cases it is not the total (n,γ) cross section which is of paramount interest, but the (n,γ) cross section resulting in transitions to a particular isomeric state. For this reason, Γ_γ is the capture width leading to the isomeric state of interest, while Γ_f is the width associated with all other neutron-absorbing transitions not leading to the isomeric state of interest. If no isomeric states of the product nucleus exist, Γ_f is tabulated as zero, unless there is fission.

The effective resonance integral for each resonance is computed using Dresner's formalism (ref. 14),

$$RI = \frac{\sigma_o \Gamma_\gamma \beta}{E_o} J(\xi, \beta) \tag{73}$$

where $J(\xi, \beta)$ is Dresner's J-function, which is discussed below, and ξ is defined by

$$\xi = \Gamma \left(\frac{A}{1.9148 \times 10^{-4} E_o (T + 459.69)} \right)^{1/2} \tag{74}$$

where Γ and E_o are in eV. Here A is the atomic weight of the resonance absorber (which is approximated by the atomic number), Γ is the total width $(\Gamma_\gamma + \Gamma_f + \Gamma_n)$, and T is the temperature of the absorber material in degrees Fahrenheit.

27

The quantity β appearing in equation (73) depends on whether the neutron energy loss in a scattering collision with an absorber nucleus is greater or less than the practical width of the resonance. The practical width of the resonance is that energy interval throughout which the resonance cross section is larger than the non-resonance cross section of the absorbing material. If the neutron energy loss is greater than the practical width, the narrow resonance approximation is used and

$$\beta = \frac{\sigma_m}{\sigma_o}. \tag{75}$$

If the neutron energy loss is less than the practical width, the wide resonance approximation is used and

$$\beta = \frac{\sigma_m \Gamma}{\sigma_o \Gamma_\gamma}. \tag{76}$$

The cross sections σ_o and σ_m appearing in the above formulae require some explanation. The quantity σ_o is simply the peak resonance cross section,

$$\sigma_o = \frac{2.62 \times 10^6 g \Gamma_n}{E_o \Gamma} \text{ barns} \tag{77}$$

where g is the statistical factor and E_o and the widths are in eV. The quantity σ_m is the sum of those scattering, or pseudo-scattering, cross sections representing neutron energy losses larger than the practical width of the resonance, i.e. escape from the resonance. Neutron leakage from the absorbing region is treated by Wigner's rational approximation. That is, a fictitious cross section σ_v represents such leakage. This "volume scattering" cross section depends upon the mean chord length (equal to four times the volume of the region divided by the surface area) of the absorbing region. If $2r$ is the

28

mean chord length, then

$$\sigma_v = \frac{1}{2rN_0} \qquad (78)$$

where N_0 is the atom density of the resonance absorber in the absorbing region. Assuming that all neutrons of energy near the resonance energy which leak out from the absorbing region do not re-enter the absorbing region with energies near the resonance energy, σ_v represents a loss of neutrons from the resonance. Thus the minimum value of σ_m is σ_v. Other contributions to σ_m depend upon the practical width of the resonance and the atomic weights of the constituents of the absorbing region.

Neglecting Doppler broadening of the resonance, it is easily shown that the practical width of the resonance is

$$\Gamma_{pr} = \Gamma \left(\frac{\sigma_0}{\sigma_v + \sigma_p} - 1 \right)^{1/2} \qquad (79)$$

where σ_p is the energy-independent potential scattering cross section of the absorbing region per resonance absorber nucleus. Values of σ_p for all isotopes are tabulated in the cross section library. Then

$$\sigma_p = \sum_i N_i \sigma_{pi} / N_0 \qquad (80)$$

where N_i is the atom density of isotope i in the absorbing region, σ_{pi} is the potential scattering cross section of the isotope i, and the summation is performed over all the constituents of the region. If $\sigma_0 < \sigma_v \sigma_p$, the practical width vanishes, and any scattering event removes neutrons from the resonance. In this case, σ_m achieves its maximum value of $\sigma_v + \sigma_p$. If $\Gamma_{pr} > 0$, there exists some mass number A_{max} such that neutron scattering with an isotope of mass number less than A_{max} results in sufficient energy loss to remove the neutron

from the resonance. This critical mass number is

$$A_{max} = 2 \left(\frac{E_o}{\Gamma_{pr}} - \frac{1}{3}\right) \tag{81}$$

In general, the quantity σ_m is computed by

$$\sigma_m = \sigma_v + \sum_j N_j \sigma_{pj}/N_o \tag{82}$$

where the summation is performed over those isotopes in the absorbing region which have mass numbers less than A_{max}.

Dresner's J function is computed by the NAP program either by interpolation from Dresner's tables (ref. 14) or by approximations due to Dresner or Doherty (ref. 15). If β is greater than 670, the J function is given with sufficient accuracy by

$$J = \frac{\pi}{2\beta} \qquad (\beta > 670) \tag{83}$$

If ξ is less than or equal to 0.05,

$$J = \frac{\sqrt{\pi}\left(\sqrt{\pi} + \dfrac{\xi}{2\beta + \xi\sqrt{\pi}}\right)}{2\beta + \sqrt{\pi}\xi} \qquad (\xi \leq 0.05) \tag{84}$$

which also holds for ξ less than 0.1 if β is greater than 335. If ξ is greater than unity and β is greater than 335,

$$J = \frac{\pi/2}{\sqrt{\beta(1 + \beta)}} \tag{85}$$

and is approximately valid for all β. Dresner's table covers the range $0.1 \leq \xi \leq 1.0$, at ξ intervals of 0.1, and $10^{-5} \leq \beta \leq 2600$. The dependence of J is expressed in terms of the variable j, where

$$\beta = 2^j \times 10^{-5} \tag{86}$$

30

The tabular data covers the range $0 \leqslant j \leqslant 31$ at j intervals of 1.0. For values of ξ and β not covered by the tabular data or the equations above,

$$J = \frac{(\pi/2)(1 + e^x)}{\sqrt{\beta(1 + \beta)}} \tag{87}$$

where

$$
\begin{aligned}
x = \ & -9.823 - 1.9579\,Z + 0.36905\,Z^2 - 0.0025594\,Z^3 \\
& + y(0.29494 - 0.27824\,Z + 0.0010257Z^2 + 0.0032999Z^3) \\
& + y^2(-0.0027388 + 0.0012878Z - 0.000285Z^2 - 0.00011668Z^3) \\
& + 10^{-6}y^3(-1.7541 - 9.6663Z + 2.7508Z^2 + 0.86618Z^3)
\end{aligned} \tag{88}
$$

Here Z is the natural logarithm of ξ and y is $j^{1.4508}$. The selection of the preferred form of the J function is summarized in Table 4.

b.) Estimation of Thermal (n,γ) Cross Sections

Because the NAP program is designed to be a comprehensive computational tool, provision has been made for estimation of (n,γ) cross sections when only the Z and A of the target nucleus are known. There is some physical evidence (ref. 16) that thermal (n,γ) cross sections are dependent upon the even-odd character of the nucleus and the proximity of the number of neutrons in the nucleus to the magic numbers. All measured 2200 m/sec (n,γ) cross section values were collected and then approximated by least-square techniques. The results are shown in Figures 1-4 where the measured values are indicated by the dots and the derived approximations by the solid lines. The cross section dependence on magic number is evident, without taxing one's imagination, only for even-even nuclei. The cross section for odd-A nuclei appear to be independent of the even-odd character of Z (or N). The cross sections for even-even

31

Table 4

PREFERRED APPROXIMATIONS OF $J(\xi, \beta)$

	$\beta < 10^{-5}$	$10^{-5} \leqslant \beta < 335$	$335 < \beta < 670$	$\beta \geqslant 670$
$\xi \leqslant 0.05$	Eq. (84)	Eq. (84)	Eq. (84)	Eq. (83)
$0.05 < \xi < 0.1$	Eq. (87)	Eq. (87)	Eq. (84)	Eq. (83)
$0.1 \leqslant \xi \leqslant 1$	Eq. (87)	Table	Table	Eq. (83)
$\xi > 1$	Eq. (87)	Eq. (87)	Eq. (85)	Eq. (83)
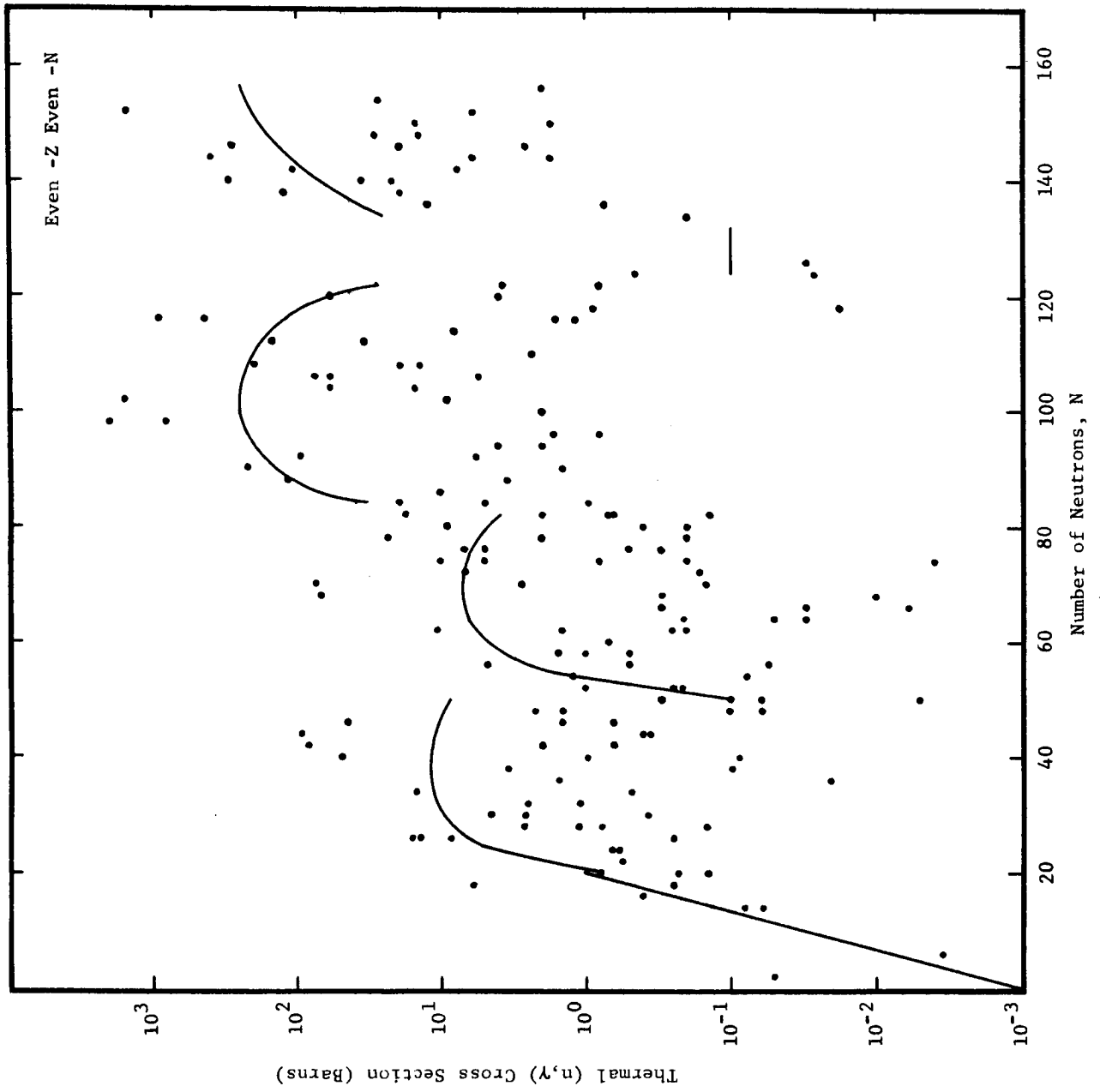
FIGURE 1 - THERMAL CROSS SECTION OF EVEN-EVEN NUCLEI
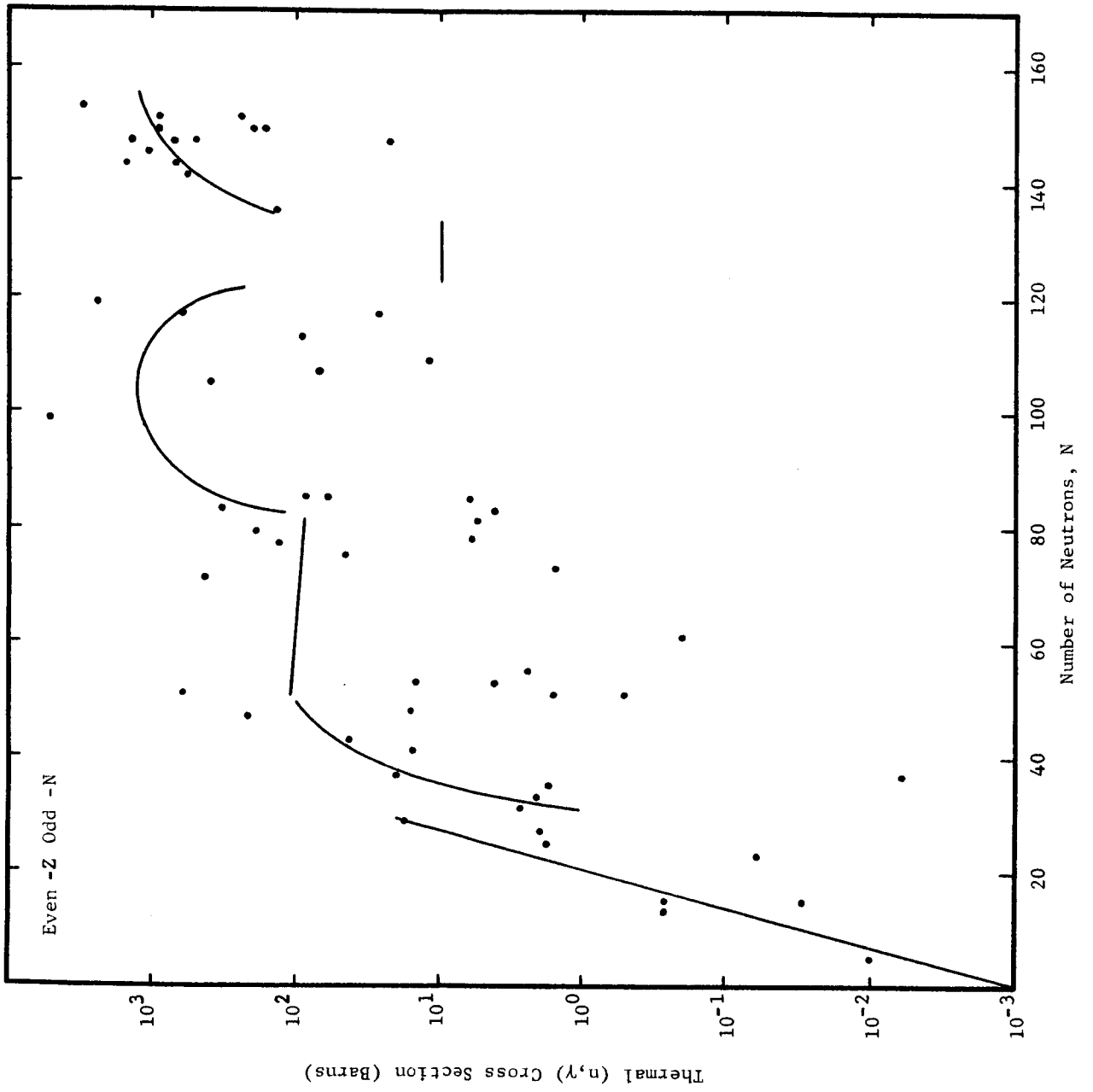
FIGURE 2 - THERMAL CROSS SECTION OF EVEN-ODD NUCLEI

Even -Z Odd -N

Number of Neutrons, N

Thermal (n,γ) Cross Section (Barns)

34
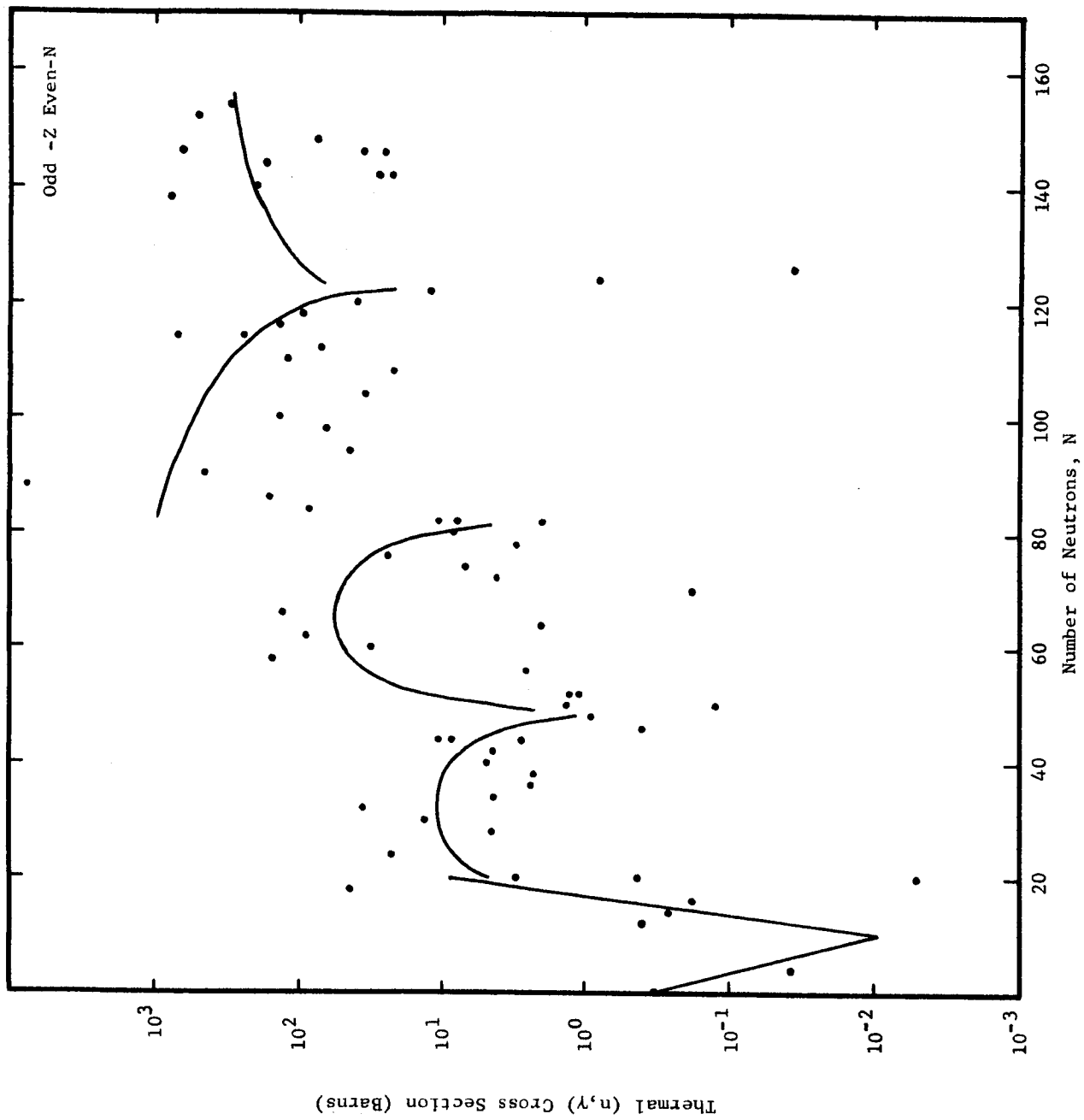
FIGURE 3 - THERMAL CROSS SECTION OF ODD-EVEN NUCLEI
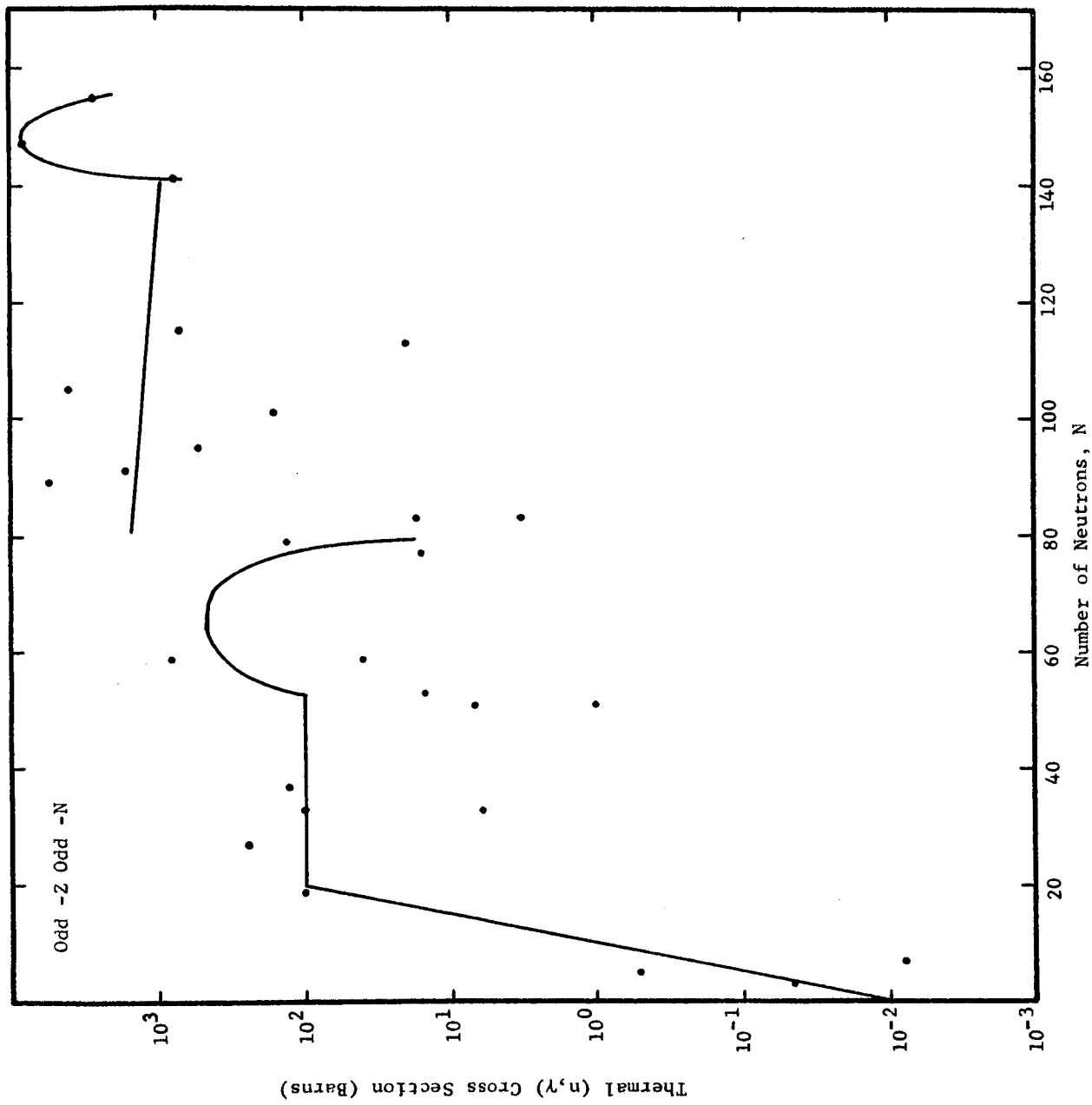
FIGURE 4 - THERMAL CROSS SECTION OF ODD-ODD NUCLEI

36

nuclei appear to be slightly lower than those for odd-A
nuclei, while the cross sections for odd-odd nuclei appear
to be slightly higher than those for odd-A nuclei.
Analytical expressions for the solid lines in the figures are
given below, where σ is the 2200 m/sec value for the (n,γ)
cross section, and N is the number of neutrons in the nucleus.

1. Even-Z even-N nuclei:

$$\sigma = 10^{3(0.05N-1)} \qquad\qquad N < 21$$
$$= -34.61+2.371N-0.03016N^2 \qquad 21 < N < 49$$
$$= -17.92+0.3383N \qquad\qquad 49 < N < 55$$
$$= -104.9+3.195N-0.02278N^2 \qquad 55 < N < 123$$
$$= -6503+131.6N-0.6401N^2 \qquad 83 < N < 123$$
$$= 0.1 \qquad\qquad 123 < N < 133$$
$$= 1520-29.91N+0.1399N^2 \qquad 133 < N$$

2. Even-Z odd-N nuclei:

$$\sigma = 10^{3(0.05N-1)} \qquad\qquad N < 30$$
$$= 181.4-12.95N+0.2302N^2 \qquad 30 < N < 50$$
$$= 148.5-0.7464\ N \qquad\qquad 50 < N < 82$$
$$= -30474+619.86N-3.0243N^2 \qquad 82 < N < 122$$
$$= 10 \qquad\qquad 122 < N < 134$$
$$= 115441-1647.4N+5.988N^2 \qquad 134 < N$$

3. Odd-Z even-N nuclei:

$$\sigma = 10^{-0.46032N-0.15873} \qquad N < 11$$
$$= 0.05N-0.79 \qquad\qquad 11 < N < 21$$
$$= -33.26+2.756N-0.04243N^2 \quad 21 < N < 49$$
$$= -875.2+28.48N-0.2176N^2 \quad 49 < N < 81$$
$$= 2919-23.75N \qquad\qquad 81 < N < 123$$
$$= -2624+33.64N-0.09556N^2 \quad 123 < N$$

4.   Odd-Z, odd-N nuclei:

$$
\begin{aligned}
\delta &= 10^{2(0.1N+1)} & N &< 20 \\
&= 100 & 20 &< N < 52 \\
&= -987+317.7N-2.431N^2 & 52 &< N < 80 \\
&= 2376-10.27N & 80 &< N < 140 \\
&= 2809000+37940N-127.7N^2 & 140 &< N
\end{aligned}
$$

These analytical expressions agree with the measured
values to within two orders of magnitude for most of the data,
although occassionally the error is as large as three orders
of magnitude. It should be emphasized that <u>these formulae
are not intended to generate accurate values of known cross
sections</u>, but are used only to obtain crude estimates of un-
known cross sections.

c.)   Estimation of Epithermal (n,γ) Cross Sections

A crude estimate of unknown epithermal (n,γ) cross sections
is provided by the NAP program by estimating resonance para-
meters and using equation (72) above. The infinitely dilute
(large β) limit of equation (73) is

$$
RI = \frac{\pi\,\delta_o\,\Gamma_\gamma}{2E_o} \tag{89}
$$

If the average energy spacing between resonances is D, then
the total resonance integral due to all the resonances between
the energies E_{g-1} and E_g is, on the average,

$$
RI = \frac{\pi}{2D} \int_{E_g}^{E_{g-1}} \frac{\delta_o\,\Gamma_\gamma}{E}\,dE \tag{90}
$$

Using equation (77) for δ_o, taking the statistical factor as
one-half, assuming that Γ_γ is energy-independent and that the

energy independence of Γ_n is expressed by $\Gamma_n^o \sqrt{E}$ (ref. 14), equation (90) is easily integrated to yield

$$RI = 1.31 \times 10^6 \, \pi \, f \left[x_g - x_{g-1} + \frac{fD}{\Gamma_\gamma} \log \left(\frac{x_{g-1} + \frac{fD}{\Gamma_\gamma}}{x_g + \frac{fD}{\Gamma_\gamma}} \right) \right] \tag{91}$$

where f is the strength function defined as Γ_n^o/D, x_g is $E_g^{-1/2}$, and similarly for x_{g-1}. The epithermal group (n, γ) cross sections are then estimated by substituting equation (91) into equation (72) and assuming that the 1/v contribution arises from the 2200 m/sec value as measured and tabulated, or as estimated above.

The statistical resonance parameters f, D, and Γ_γ required in equation (91) are estimated as follows. Measured values (ref. 17) of the average capture width Γ_γ are shown in Figure 5 as a function of atomic number Z. A least squares fit to this data is represented by

$$\Gamma_\gamma \, (eV) = 1.802 - 0.0765 \, Z + 0.001152 Z^2 - 0.573 \times 10^{-5} Z^3$$
$$(Z \geq 30) \tag{92}$$

Values of Γ_γ given by this expression are shown by the solid line in Figure 5. For small Z, the average capture width is taken as

$$\Gamma_\gamma(eV) = 0.01297 \, Z \qquad (Z < 30) \tag{93}$$

Similarly, values of the average energy spacing between s-wave resonances have been deduced from measured resonance energies (ref. 17) and are shown for odd-Z even-N nuclei in Figure 6 as a function of mass number A. A least squares fit to these data is represented by

$$D(eV) = \exp(12.29 - 0.1058 \, A + 0.2545 \times 10^{-3} \, A^2)$$
$$(odd \, A) \tag{94}$$

39

Figure 5

Average Capture Width
vs.
Atomic Number

Cubic Fit

Γ_γ (ev)

Atomic Number, Z

40

Figure 6

LEVEL SPACING FOR ODD-Z EVEN-N NUCLEI

○ Experimental Points
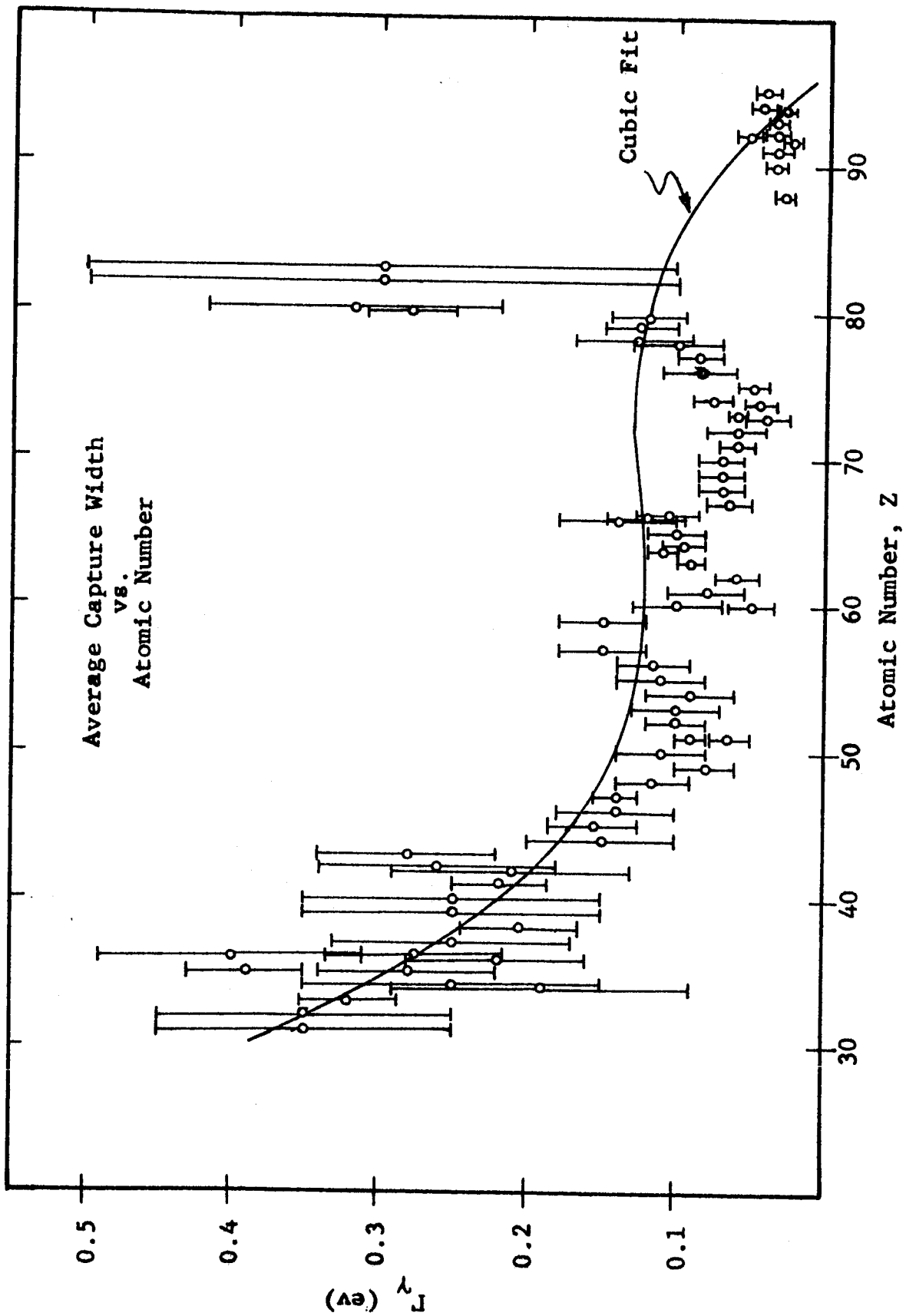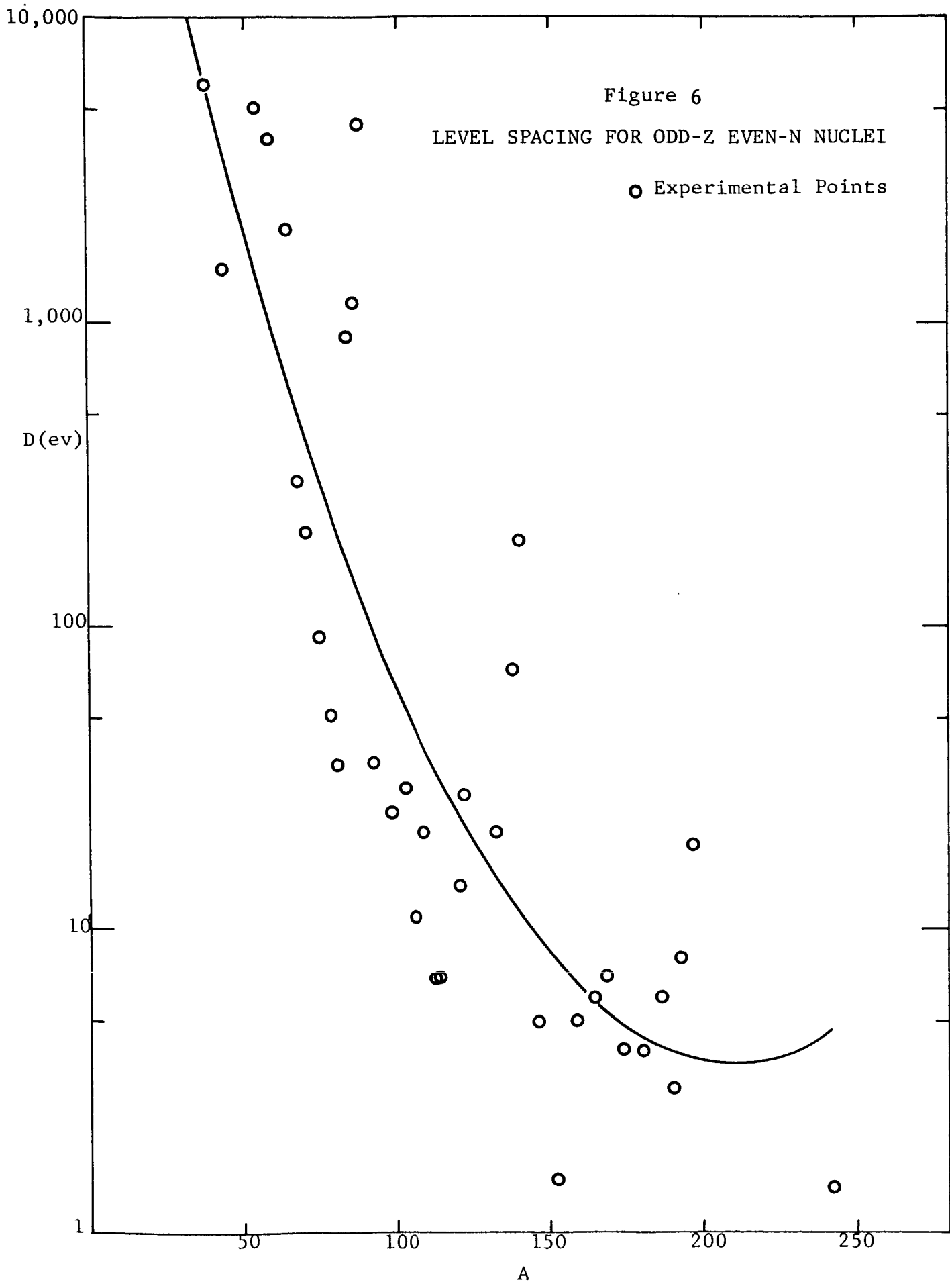
which is illustrated by the solid line in Figure 6. Since D is inversely proportional to the level density, the level spacing for even-A nuclei is taken as

$$D(\text{odd-N, odd-Z}) = 0.5 \ D(\text{odd A}) \tag{95}$$

$$D(\text{even-N, even-Z}) = 5 \ D(\text{odd A}) \tag{96}$$

as in section II-C-1-d above.

Finally, empirically derived values (ref. 18) of the s-wave strength function f are shown in Figure 7 as a function of mass number A. A least squares fit to these data is represented by

$$f(eV^{-1/2}) = (-201.1+12.94 \ A-0.2559 \ A^2+0.002217 \ A^3$$

$$- \ 0.8695 \times 10^{-5} \ A^4 + 0.1264 \times 10^{-7} \ A^5) \times 10^{-4} \tag{97}$$

which is illustrated by the solid line in Figure 7. For small A, the above expression for f yields negative values. If this occurs, the NAP programs takes f as $10^{-5} \ eV^{-1/2}$.

Again it should be emphasized that the thermal and epithermal (n,γ) cross section calculations described above must be regarded as a crude estimation scheme. Better estimates could be obtained, but only at the expense of far greater complexity and loss of generality. In addition, the vast majority of (n,γ) cross sections encountered in the typical NAP problem have been measured. These measured data are utilized in the NAP Cross Section Library, and the calculation scheme described above is used only when the pertinent cross sections are not found in the library.
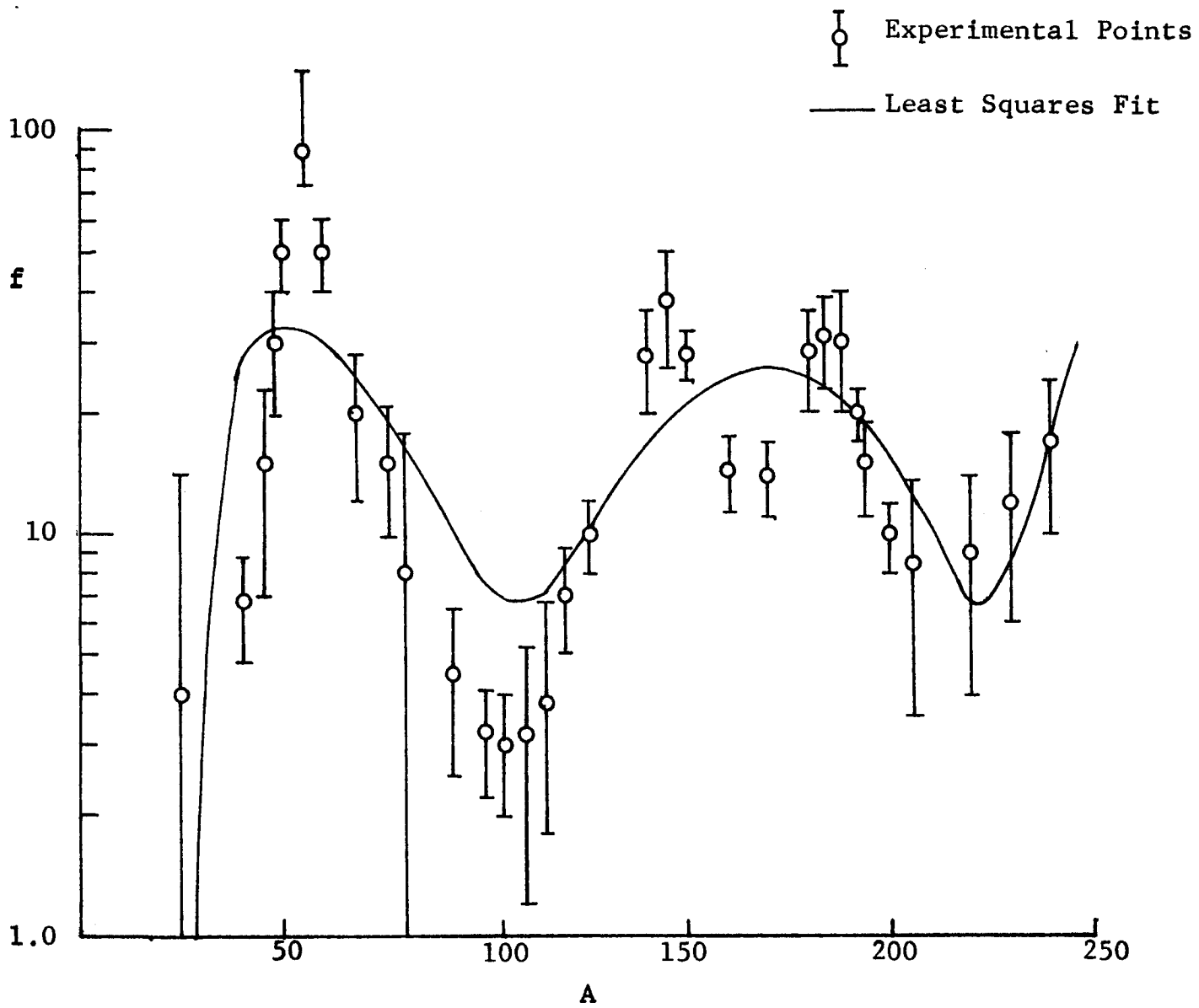
Figure 7

S-wave Strength Function

D. Isotope Concentration as Function of Time

The source strength calculation performed by the NAP program depends upon basic nuclear data which is contained in the NAP Gamma Radiation Library and upon $n_j(t)$, the atom density of isotope j at the time t. The calculation of $n_j(t)$ is based on a scheme suggested by Vondy (ref. 19). This scheme is used to compute the isotopic densities of the members of a radioactive decay chain as a function of time, knowing the production and loss rates of each member in the chain.

The current NAP program assumes a maximum chain length of five members. The chain is assumed to initiate by neutron irradiation of a stable isotope. This stable isotope is transmutted to one or more different isotopes by (n,γ), (n,p), (n,α) and/or $(n,2n)$ reactions. Each succeeding chain member decays away to one or more daughter isotopes. Isomeric states are treated as separate isotopes. Information required to set up the chain is contained in the Gamma Radiation Library.

In many cases, complicated branchings are found to occur in the chain as typified in the schematic representation of neutron irradiation of Ge^{76}:
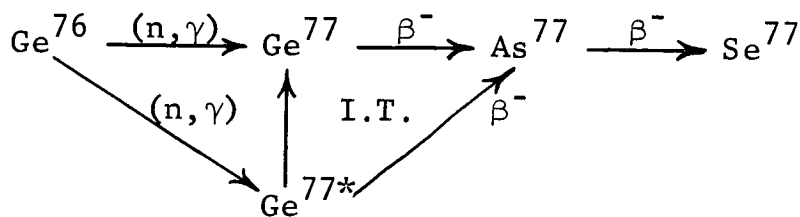
Half-lives, branching ratios, and cross sections have been omitted for clarity. The isomeric state is indicated by an asterisk; the isomeric transition is indicated by I.T.

It would be possible, in principle, to solve the differential equations which describe all the possible chain couplings which exist. However, such a specific treatment could not be altered easily if later data indicated the need to add other couplings. A more basic approach is to resolve each chain,

44

such as the one above, into several sub-chains of nuclides, each isotope in the sub-chain being coupled to a single parent. These sub-chains, which exhibit no branches, can be described by a set of coupled equations which have been solved independently of particular nuclide parameters. The solutions can be applied to all sub-chains. For example, the chain above may be resolved into the three sub-chains:

$$Ge^{76} \xrightarrow{(n,\gamma)} Ge^{77} \xrightarrow{\beta^-} As^{77} \xrightarrow{\beta^-} Se^{77}$$

$$Ge^{76} \xrightarrow{(n,\gamma)} Ge^{77*} \xrightarrow{I.T.} Ge^{77} \xrightarrow{\beta^-} As^{77} \xrightarrow{\beta^-} Se^{77}$$

$$Ge^{77*} \xrightarrow{\beta^-} As^{77} \xrightarrow{\beta^-} Se^{77}$$
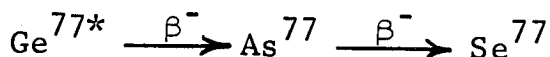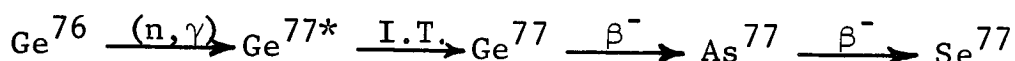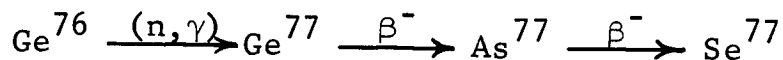
These sub-chains are independent in the sense that the daughter nuclide concentrations in each sub-chain is calculated without regard to other sub-chains. The total concentration of each nuclide is then the sum of the partial concentration from each sub-chain. Similarly, the total gamma source strength due to a given chain is the sum of the partial source strengths from each sub-chain. It may be noted in passing that when isomeric states are produced as a consequence of neutron-induced reactions, it is necessary to have available both the cross section for transitions to the ground state and the cross section for transitions to the isomeric state.

A generalized chain may thus be represented schematically by

$$
\begin{array}{ccccccccc}
n_1 & \xrightarrow{\sigma_i} & n_2 & \xrightarrow{\lambda_2 b_2} & n_3 & \xrightarrow{\lambda_3 b_3} & n_4 & \xrightarrow{\lambda_4 b_4} & n_5 & \xrightarrow{\lambda_5} \\
\Big\downarrow{\sigma_j \atop j \neq i} & & \Big\downarrow{\lambda_2(1-b_2)} & & \Big\downarrow{\lambda_3(1-b_3)} & & \Big\downarrow{\lambda_4(1-b_4)} & & &
\end{array}
$$
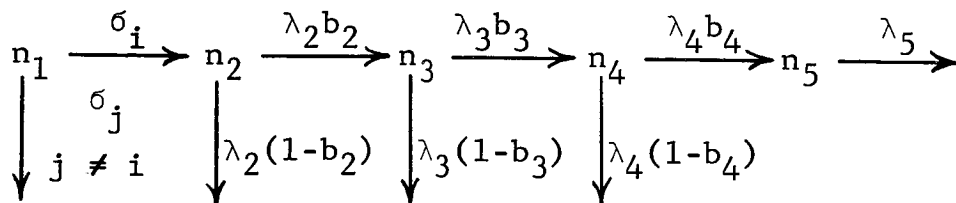
Here σ_i represents a specific neutron-induced reaction leading to a specific nuclide, σ_j represents all other neutron-induced

45

reactions, n_i is the atom density of chain member i, λ_i is the decay constant of member i, and b_i is the probability (branching ratio) that chain member i decays to chain member i + 1. Neutron-induced reactions are assumed to be significant only for the first member of the chain in the current NAP program. Only one isomeric state is permitted for each isotope. In general, eight specific cross sections are required: (n,γ), (n,p), (n,α), $(n,2n)$ cross sections leading to the ground state and (n,γ), (n,p), (n,α), $(n,2n)$ cross sections leading to the isomeric state.

The initial member of the chain is consumed by neutron bombardment according to

$$\frac{d}{dt} \, n_1(t) \;=\; -\int_{t_o}^{t} \int_{0}^{\infty} \sigma_T(E) \emptyset(t',E) \, dt' \tag{98}$$

where σ_T is the sum of all the microscopic (n,γ), (n,p), (n,α), and $(n,2n)$ cross sections of the first member of the chain, E is the incident neutron energy, $\emptyset(t,E)$ is the incident neutron flux as an arbitrary, but defined, function of time and neutron energy, and t_o is the time at which the neutron irradiation commences.

To perform the indicated integration, the time variable is divided into discrete time intervals, not necessarily of equal duration. The magnitude of the neutron flux is assumed constant (possibly zero) throughout each time interval. The energy dependence of the flux (i.e. flux spectrum) is regarded as independent of time. Any spatial variation of the flux is approximated by computing the average flux in each spatial region. This average flux computation is performed by the SHIELD subprogram of NAP using multigroup transport theory and was discussed in section II-B. If Δt is the duration of any particular time interval, and τ is the time at the beginning of the interval, the quantity

46

$$q_1 = P(t) \int_0^\infty \sigma_T(E) \emptyset(E) \, dE \tag{99}$$

is calculated, and then the atom density of the first member of the chain at the time $\tau + \Delta t$ is

$$n_1(\tau + \Delta t) = n_1(\tau) e^{-q_1 \Delta t} \tag{100}$$

Here $P(t)$ is the power level or magnitude of the flux and is constant throughout any given time interval. In this manner, the atom density of the first member of the chain is calculated as a function of time.

The isotopic concentration of the remaining members of the chain satisfies

$$\frac{d}{dt} n_i(t) = S_{i-1} n_{i-1}(t) - q_i n_i(t) \tag{101}$$

where

$$S_1 = P(t) \int_0^\infty \sigma(E) \emptyset(E) \, dE \tag{102}$$

$$S_k = \lambda_k b_k \quad , \quad k = 2,3,4 \tag{103}$$

$$q_k = \lambda_k \quad , \quad k = 2,3,4,5 \tag{104}$$

The cross section $\sigma(E)$ appearing in S_1 depends upon the particular chain under consideration. Vondy (ref. 19) has shown that the general isotopic concentration solution, in a form amenable to digital computer programming, is

$$n_i(\tau + \Delta t) = n_i(\tau) e^{-q_i \Delta t} + \sum_{k=1}^{i-1} \left\{ n_k(\tau) \sum_{j=k}^{i-1} \left(\frac{e^{-q_j \Delta t} - e^{-q_i \Delta t}}{q_i - q_j} \right) \right.$$

$$\left. \left(S_j \prod_{\substack{n=k \\ n \neq j}}^{i-1} \frac{S_n}{q_n - q_j} \right) \right\} \tag{105}$$

For example,

$$n_2(\tau+\Delta t) = n_2(\tau)e^{-q_2\Delta t} + n_1(\tau)S_1 \cdot \frac{e^{-q_1\Delta t} - e^{-q_2\Delta t}}{q_2 - q_1} \tag{106}$$

$$n_3(\tau+\Delta t) = n_3(\tau)e^{-q_3\Delta t} + n_2(\tau)S_2 \cdot \frac{e^{-q_2\Delta t} - e^{-q_3\Delta t}}{q_3 - q_2} \tag{107}$$

$$+ n_1(\tau)S_1S_2 \left[\frac{e^{-q_1\Delta t} - e^{-q_3\Delta t}}{(q_3-q_1)(q_2-q_1)} + \frac{e^{-q_2\Delta t} - e^{-q_3\Delta t}}{(q_3-q_2)(q_1-q_2)} \right]$$

The resulting expression for $n_4(\tau + \Delta t)$ and $n_5(\tau + \Delta t)$ are similar, but lengthy. In this manner, the atom density for each isotope in the chain is traced out as a function of time. The accuracy and reliability of this formalism is discussed in section III.

48

III. EXPERIMENTAL VALIDATION

A.   Neutron Self- Shielding

The NAP neutron transport subroutine, described in section II-B, may be used in a typical NAP problem to calculate the average neutron flux in each energy group in each spatial region. This average flux is then used in computing the various reaction rates leading to gamma activity. The experimental work of Martinez (ref. 20) has been used to validate the NAP neutron transport calculation.

Martinez measured indium foil activation at intervals of 0.001 inch through the interior of a 4 ft x 4 ft x 0.010 inch thick indium sheet located in the central plane of a four-foot graphite cube. Neutrons were supplied by the thermal column of the Livermore Pool Type Reactor to one surface of the graphite cube. The outer surface of the graphite cube was covered with boral, which was black to thermal neutrons, except for an 8 in. x 8 in. source area which permitted neutrons to emanate from the thermal column, diffuse through the graphite, and impinge upon the front face of the indium sheet.

The NAP neutron transport subroutine was used to calculate the thermal neutron flux through the graphite cube and indium sheet using one-dimensional slab geometry. The graphite macroscopic scattering cross section was taken as 0.400 cm^{-1}, and the macroscopic absorption cross section was inferred from an inverse diffusion length measurement by Martinez to be 0.001247 cm^{-1}. The indium density was reported to be 7.31 g/cm^3. The indium microscopic scattering and 2200 m/sec absorption cross sections were taken as 2.2 and 194.6 barns, respectively. Using room temperature values for the Westcott g and s factors (ref. 21), namely 1.019 and 18.7, respectively, the macroscopic thermal absorption average cross

section was taken as

$$\Sigma_a = \frac{\pi T_o}{4T} \ (g + rs) \quad \Sigma_a \ (2200 \ m/sec) = 7.2337 \ cm^{-1}$$

The epithermal index r was estimated as 0.04 from a cadmium ratio measurement by Martinez. The cross sections used in the NAP calculations are summarized in Table 5.

A comparison of the measured and NAP calculated thermal neutron flux is shown in Figure 8 in the absence of the indium sheet, and in Figure 9 for the indium sheet inserted. In these calculations, an isotropic neutron source of infinite extent was assumed at the origin, and four angular ordinates were used. The observed difference between the measured and calculated flux distributions, as shown in Figures 8 and 9, is due to the difference between an infinite source plane (as used in the calculation) and an 8 in. x 8 in. source (as used in the experiment). In order to obtain satisfactory agreement between the calculated and observed flux shape at the rear of the indium sheet, it was necessary to use a small program mesh spacing in the graphite immediately to the rear of the indium.

To obtain a more detailed comparison between the NAP calculations and experiment, additional calculations were performed using different numbers of angular ordinates. To reduce the time involved in the calculations, the flux was assumed incident on the front face of the indium sheet, rather than at the face of the graphite cube. One set of calculations assumed the incident flux as isotropic, the other set assumed an anisotropic incident flux, the degree of anisotropy being obtained from the calculation used to obtain Figure 9. The results of these more detailed calculations are shown in Figures 10 and 11, along with the measured flux and a tabulation of the average flux in the indium foil. Both the calculated and the measured fluxes are normalized to unity at

50

Table 5

CROSS SECTIONS FOR MARTINEZ EXPERIMENT

	Graphite	Indium
$\Sigma_s (cm^{-1})$	0.400	0.0844
$\Sigma_t (cm^{-1})$	0.4012	7.3181

Graphite Cube
with no indium sheet

Figure 8

THERMAL FLUX IN GRAPHITE CUBE

○ Calculated Flux

△ Measured Flux

Graphite Cube with 0.010 inch
Thick Indium Sheet

Figure 9

THERMAL FLUX IN GRAPHITE CUBE
WITH INDIUM SHEET

○ Calculated Flux

△ Measured Flux

self-shielding factor

experimental	
curve A	0.835
curve B	0.945
curve C	0.915
	0.888

isotropic incident flux

A

B

C

Indium foil

Graphite

Distance (mils) from foil front

Distance (cm) from foil rear

Neutron Flux

0.9

0.8

0.7

curve A: 2 angular ordinates
curve B: 4 angular ordinates
curve C: 8 angular ordinates

Figure 10

FLUX IN INDIUM FOIL — ISOTROPIC INCIDENT FLUX

54
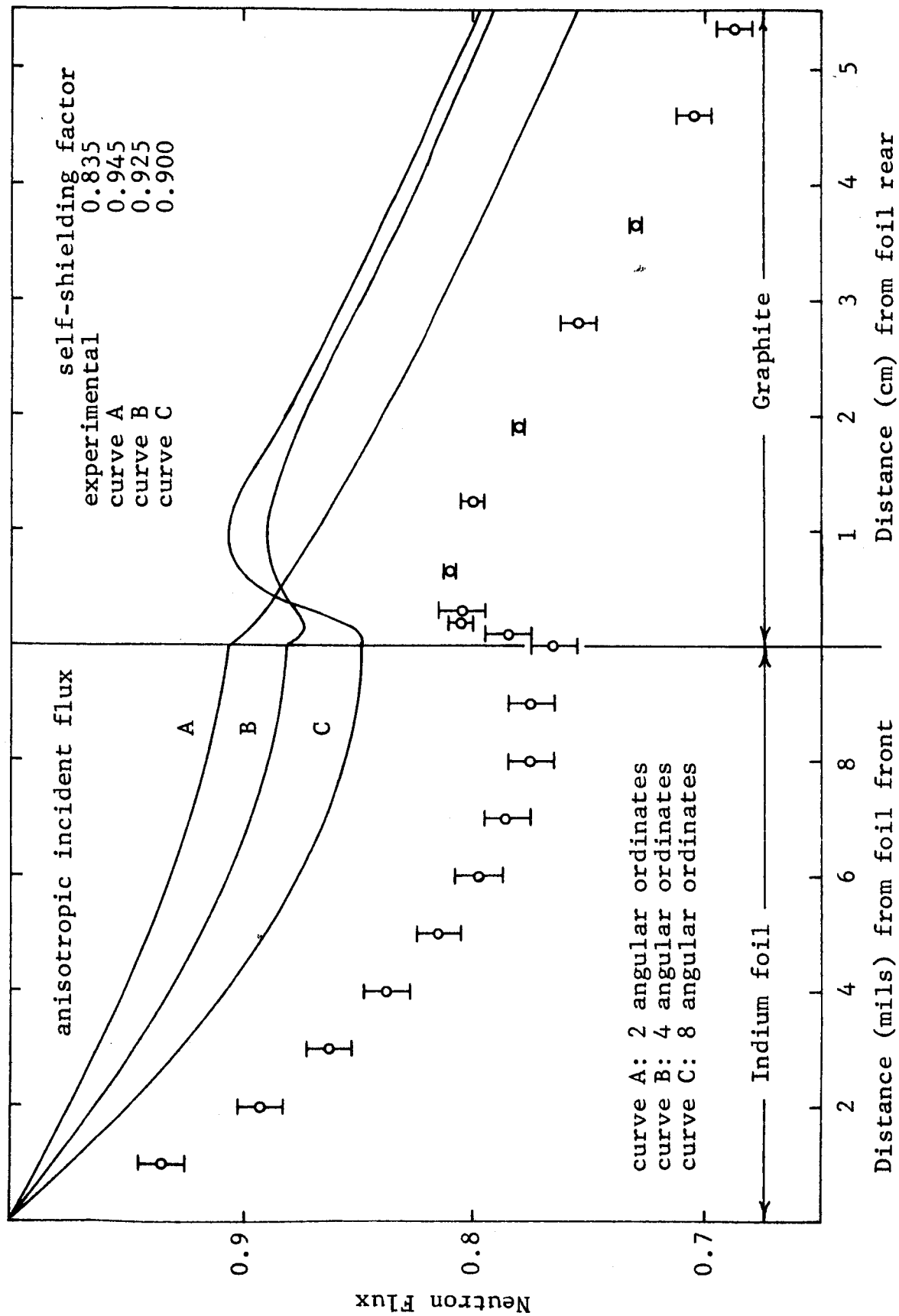
Figure 11

FLUX IN INDIUM — ANISOTROPIC INCIDENT FLUX

55

the front surface of the indium foil. The scale change behind
the foil should be noted in both figures.

The comparisons in Figures 10 and 11 show that for highly
absorptive regions, the NAP calculations underestimate the
amount of self-shielding. This is a characteristic result of
most neutron transport calculations. The calculations using
an isotropic incident flux appear to give better agreement with
experiment, because the increased average path length in the
foil tends to compensate for the underestimate of flux
depression in the foil. The isotropic incident flux calcula-
tions do not predict the rise in the flux shape behind the
foil as well as the anisotropic incident flux calculations.
In any case, eight or more angular ordinates must be used to
approach the measured flux rise.

Because the fluxes have been normalized to unity at the
front surface of the foil, the average flux in the foil is
numerically identical to the self-shielding factor, defined
as the ratio of the average flux to the surface flux. The
calculated self-shielding factors are tabulated in Figures 10
and 11. The most rigorous calculation performed (anisotropic
incident flux, eight angular ordinates) overestimates the
self-shielding factor by about eight per cent. For regions
which are less thick in terms of neutron mean free path, the
error would be smaller. The eight per cent error in self-
shielding factor is regarded as consistent with other errors
inherent in the typical NAP problem, i.e., errors in the
specification of the incident flux, the appropriate cross
sections, and the ensuing gamma ray emission probabilities.
For comparison purposes, it may be noted that the foil
self-shielding factor is often taken as (ref. 22)

$$f = \frac{1}{\tau} \left[\frac{1}{2} - E_3(\tau) \right] \tag{108}$$

where τ is the foil thickness in terms of the absorptive mean

free path. For the indium foil used here, this simple
calculation yields a self-shielding factor of 0.754, which is
in error by ten per cent.

B.   Cross Section Calculations

1.   (n,p) Cross Sections

The NAP code has been used to calculate cross sections for the (n,p) reaction using target nuclei of O^{16}, Al^{27}, P^{31}, S^{32}, K^{39}, and Ni^{58}. The physical model used in the NAP computer program has been described in section II-C-1. Comparisons of calculated and measured (n,p) cross sections are shown in Figures 12-17. In all the figures, the neutron energy is given in the laboratory system.

Figure 12 shows calculated and measured values of the O^{16} (n,p) cross section. The experimental data are from De Juren and Stooksberry (ref. 23). The calculated threshold for the reaction shows fair agreement with experiment and tabulated data shown explicitly in Table 6. The tabulated thresholds are from the Howerton compilation (ref. 28) and are based on the binding energy tabulation of König et al. (ref. 29). Negative thresholds are indicated by Howerton with a zero entry. The calculated O^{16} (n,p) cross sections are in good agreement with the measured data, at least in a gross sense. There is, of course, no mechanism built into the calculational model which will produce resonances, such as that shown in the measured data at about 12 MeV.

Figure 13 shows a similar comparison of calculated and measured values for the Al^{27}(n,p) cross section. The measured data are those quoted in BNL-325 (ref. 24). Because of the large number of measured data points, no attempt has been made to show experimental errors in the figure. Excellent agreement between calculated, measured, and tabulated values of the reaction threshold has been achieved, as shown in Table 6. The calculated and measured values of the cross section as a function of energy are seen to be in excellent agreement.

Similar excellent agreement between calculated and measured values of both the reaction threshold and the (n,p)

Table 6

COMPARISON OF CALCULATED AND TABULATED THRESHOLD ENERGIES

Reaction	Calculated Threshold (MeV)	Tabulated Threshold (MeV)
$O^{16}(n,p)$	9.52	10.22
$O^{16}(n,\alpha)$	3.62	2.35
$O^{16}(n,2n)$	17.50	16.65
$Al^{27}(n,p)$	2.03	1.90
$Al^{27}(n,\alpha)$	2.64	3.25
$Al^{27}(n,2n)$	13.79	13.51
$P^{31}(n,p)$	0.30	0.72
$P^{31}(n,\alpha)$	1.24	2.00
$P^{31}(n,2n)$	13.82	12.71
$S^{32}(n,p)$	0.99	0.95
$S^{32}(n,\alpha)$	- 1.21	0
$S^{32}(n,2n)$	15.36	15.51
$K^{39}(n,p)$	- 2.10	0
$K^{39}(n,\alpha)$	- 0.81	0
$K^{39}(n,2n)$	13.86	13.41
$Ni^{58}(n,p)$	0.04	0
$Ni^{58}(n,\alpha)$	- 2.90	0
$Ni^{58}(n,2n)$	12.62	12.40
$Cu^{63}(n,p)$	- 1.15	0
$Cu^{63}(n,\alpha)$	- 1.96	0
$Cu^{63}(n,2n)$	11.17	11.01
$I^{127}(n,p)$	- 0.02	0
$I^{127}(n,\alpha)$	- 4.50	0
$I^{127}(n,2n)$	9.09	9.22

FIGURE 12

OXYGEN (n,p) CROSS SECTION

σ(n,p) for Al-27

Experimental data
from ref. 24

NEUTRON ENERGY (MEV)

FIGURE 13

ALUMINUM (n,p) CROSS SECTION

FIGURE 14

PHOSPHORUS-31 (n,p) CROSS SECTION
Experimental data from ref. 25

62
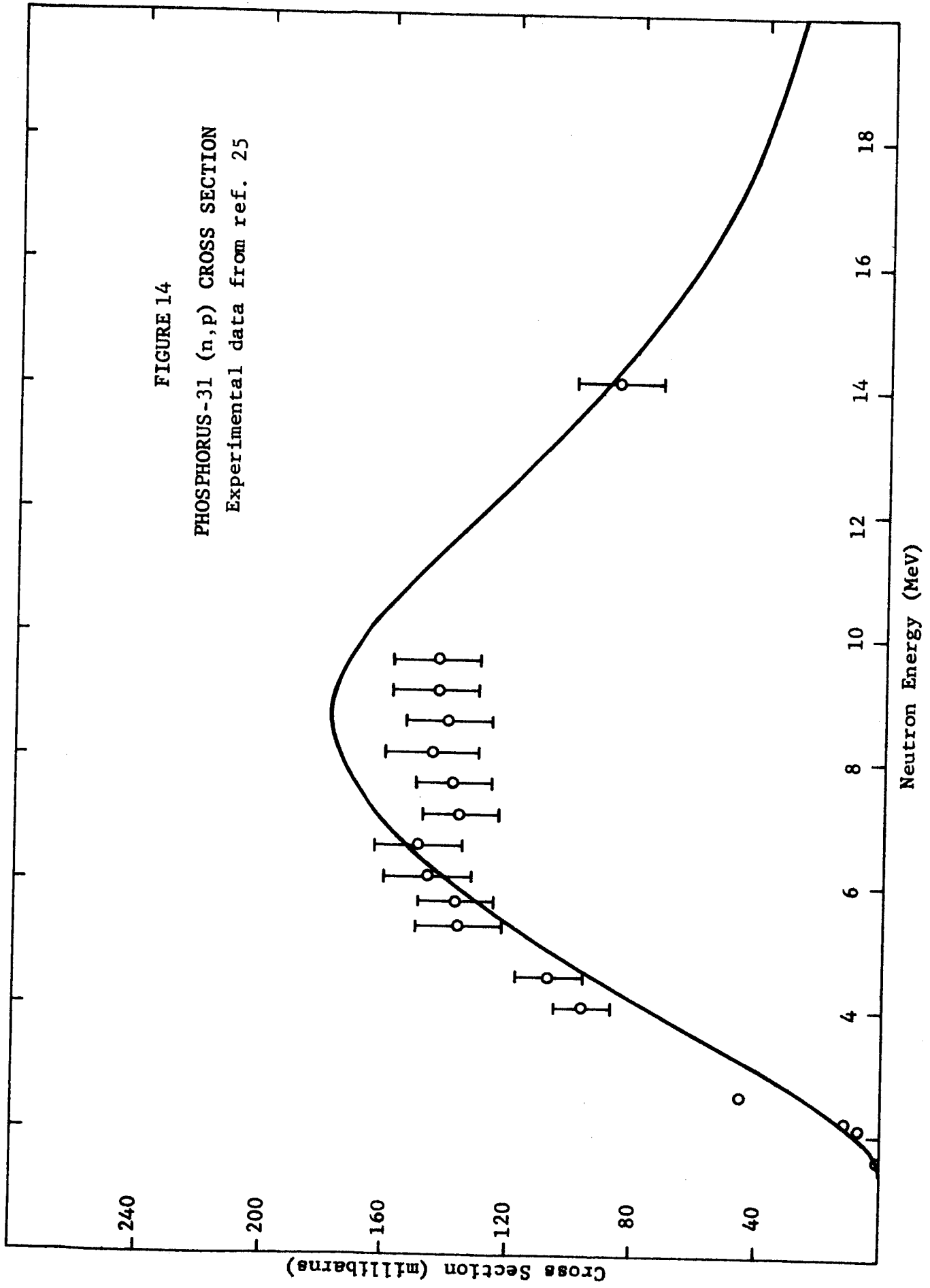
FIGURE 15

SULFUR-32 (n,p) CROSS SECTION
Experimental data from ref. 24

63
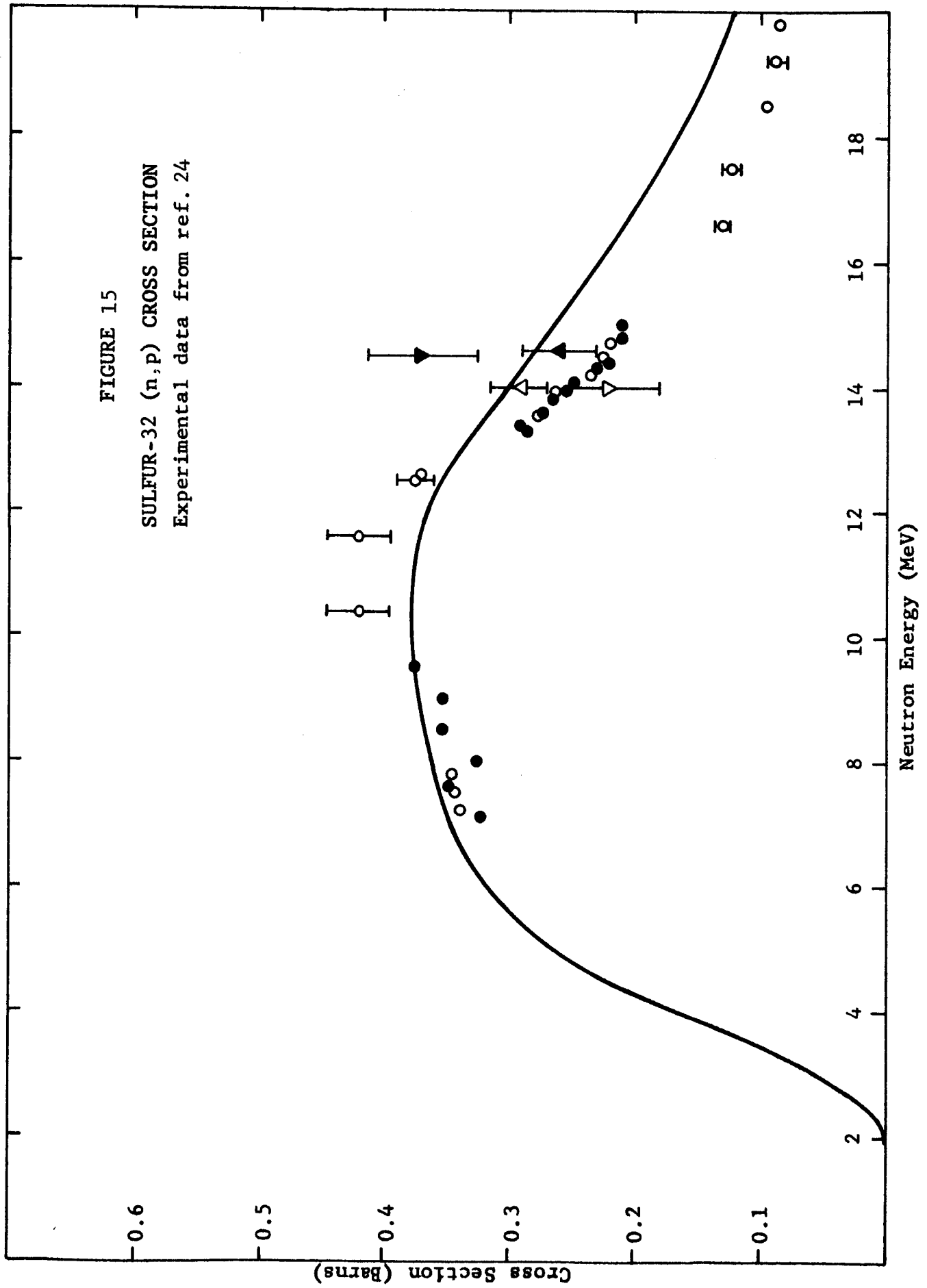
FIGURE 16

POTASSIUM-39 (n,p) CROSS SECTION
Experimental data from ref. 24

64
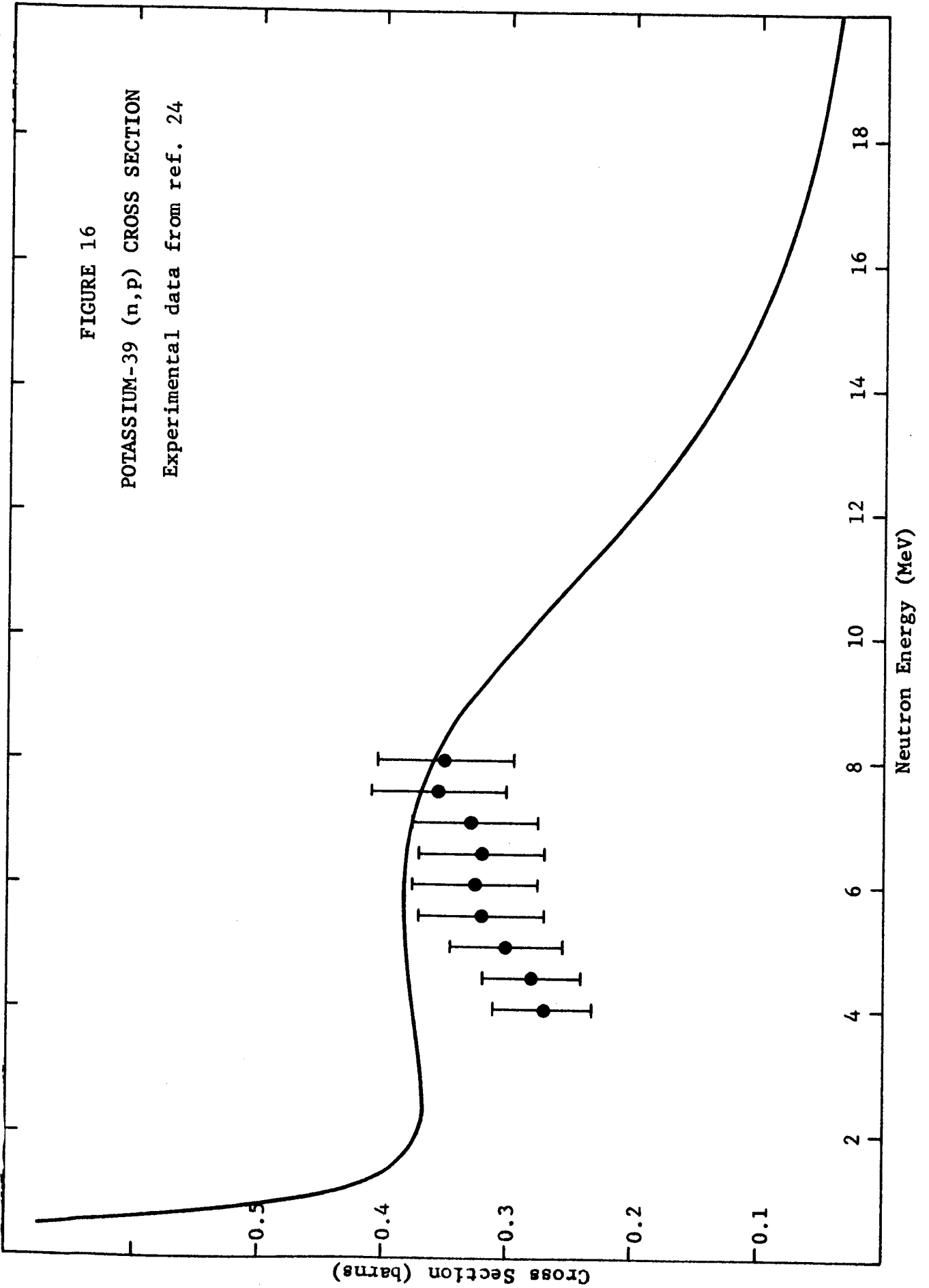
FIGURE 17

NICKEL-58 (n,p) CROSS SECTION

o From ref. 26
△ From ref. 27
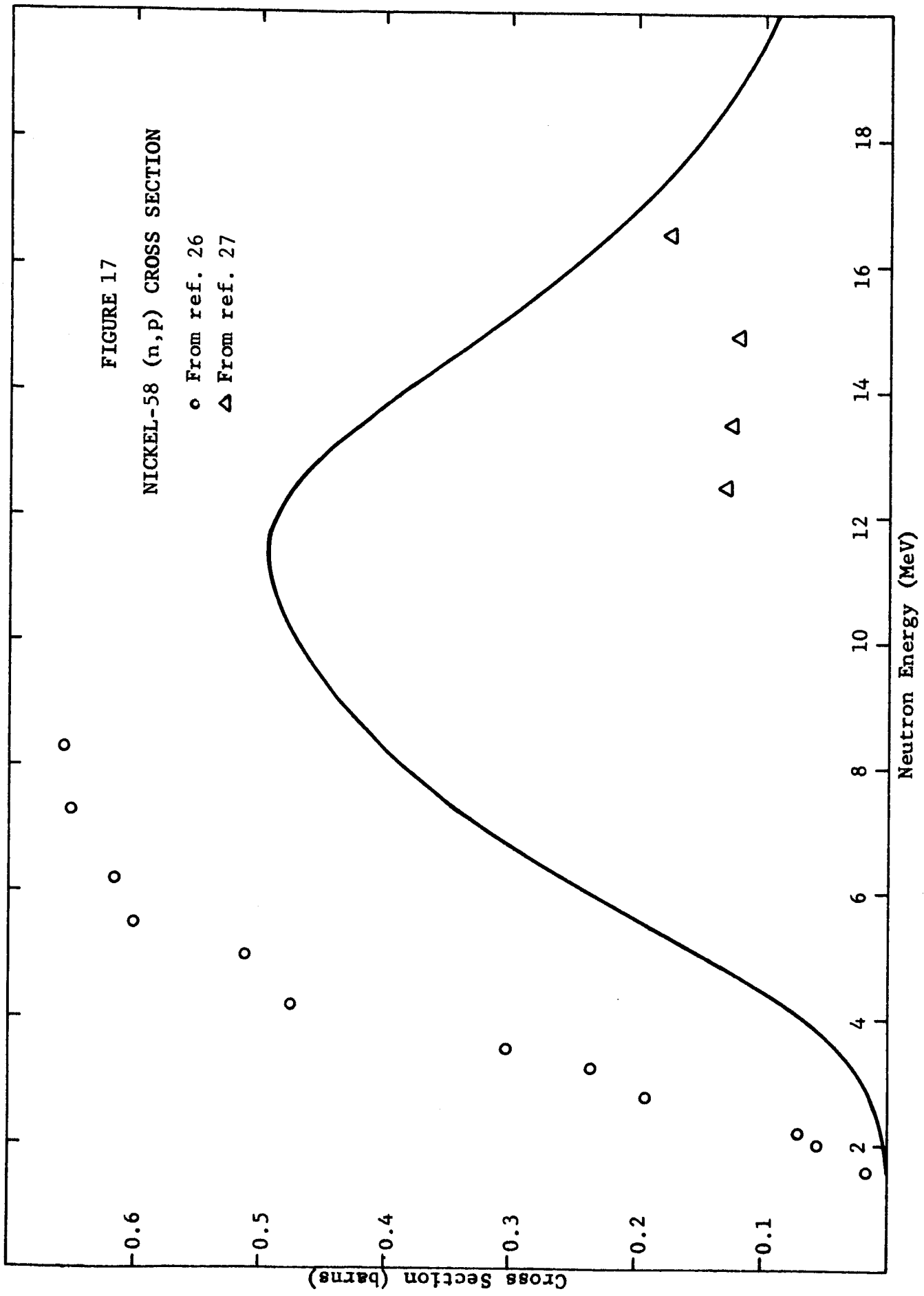
cross section as a function of energy are shown in Figure 14 for P^{31} and Figure 15 for S^{32}. The measured $P^{31}(n,p)$ cross sections are from Forbes (ref. 25), while the measured $S^{32}(n,p)$ cross sections are those quoted by BNL-325 (ref. 24).

Figure 15 shows calculated and measured (n,p) cross sections for K^{39}, which exhibits a negative energy threshold. Again good agreement is observed between the calculated and measured data in the MeV region. The measured values are those quoted in BNL-325 (ref. 24). The reported absorption cross section at 0.0253 eV is 2.1 barns, which appears to be consistent with the NAP calculations.

Finally, Figure 17 shows a comparison between measured and calculated values of the $Ni^{58}(n,p)$ cross section. The measured values are those of Barry (ref. 26) and Jeronymo (ref. 27). The measured values from the two different sources appear to be inconsistent with one another, while the calculated values appear to lie in between the two sets of measurements. Barry has noted that calculated Ni^{58} cross sections, using far more sophisticated models than those used here, have not been in agreement with the measured data and attributes the discrepancy to closed shell effects.

Based on these comparisons between NAP cross section calculations and measured values of cross sections, it is concluded that the NAP code can be used to calculate unknown (n,p) cross sections as a function of energy in the MeV region. The results are accurate to generally better than twenty per cent, except in the vicinity of resonances (such as the 12 MeV resonance in O^{16}), and for some nuclei exhibiting closed shell effects (such as Ni^{58}).

2.   (n,α) Cross Sections

Calculations of (n,α) cross sections, using the NAP code based on the method described in Section II-C-1, are compared with measured (n,α) cross sections for Al^{27}, P^{31}, S^{34}, and

K^{39} in Figures 18-21.

Figure 18 shows the comparison for Al^{27}. The measured data are those quoted in BNL-325 (ref. 24). The measured, calculated, and tabulated values of the threshold are all in good agreement as shown by the figure and Table 6. The calculated and measured values of the cross section are in excellent agreement from the threshold up to about 9 MeV. However, the calculated peak cross section is about twice as large as the measured values, although the shape of the calculated cross section curve as a function of energy is qualitatively correct.

Figure 19 shows a similar comparison in the case of P^{31}. Again the calculated and tabulated threshold values shown in Table 6 are in fair agreement, but the calculated cross sections appear to be about a factor of two higher than the measured data. The measured data are those quoted in BNL-325(ref. 24).

Figures 20 and 21 show similar comparisons in the case of S^{34} and K^{39}, respectively. The measured S^{34} cross section data are from Allen (ref. 30), while that of K^{39} is quoted in BNL-325 (ref. 24). In both cases, the calculated threshold energy appears to be somewhat higher than that consistent with the measured cross section data. There are insufficient measured data to draw any meaningful conclusions concerning the (n,α) cross section calculations in these two cases.

It may be concluded that the NAP code can be used to calculate unknown (n,α) cross sections in the MeV range. The expected accuracy is roughly a factor of two. It may be possible to empirically adjust the NAP computation of the cross section for compound nucleus formation by alpha particles to obtain better agreement with measured (n,α) cross sections. This cannot be done at the present time due to the lack of extensive comparisons between calculated and measured (n,α) cross sections.
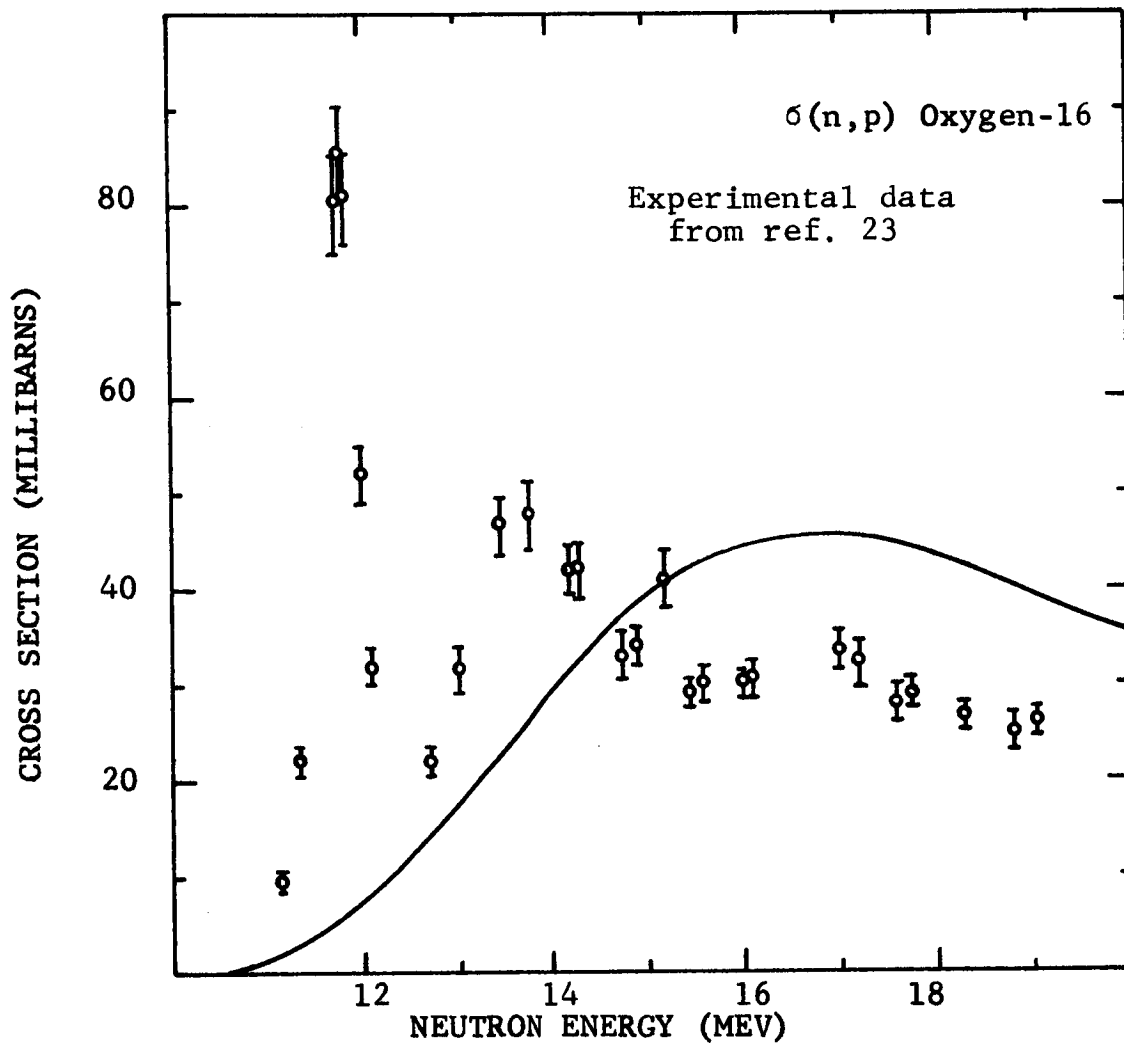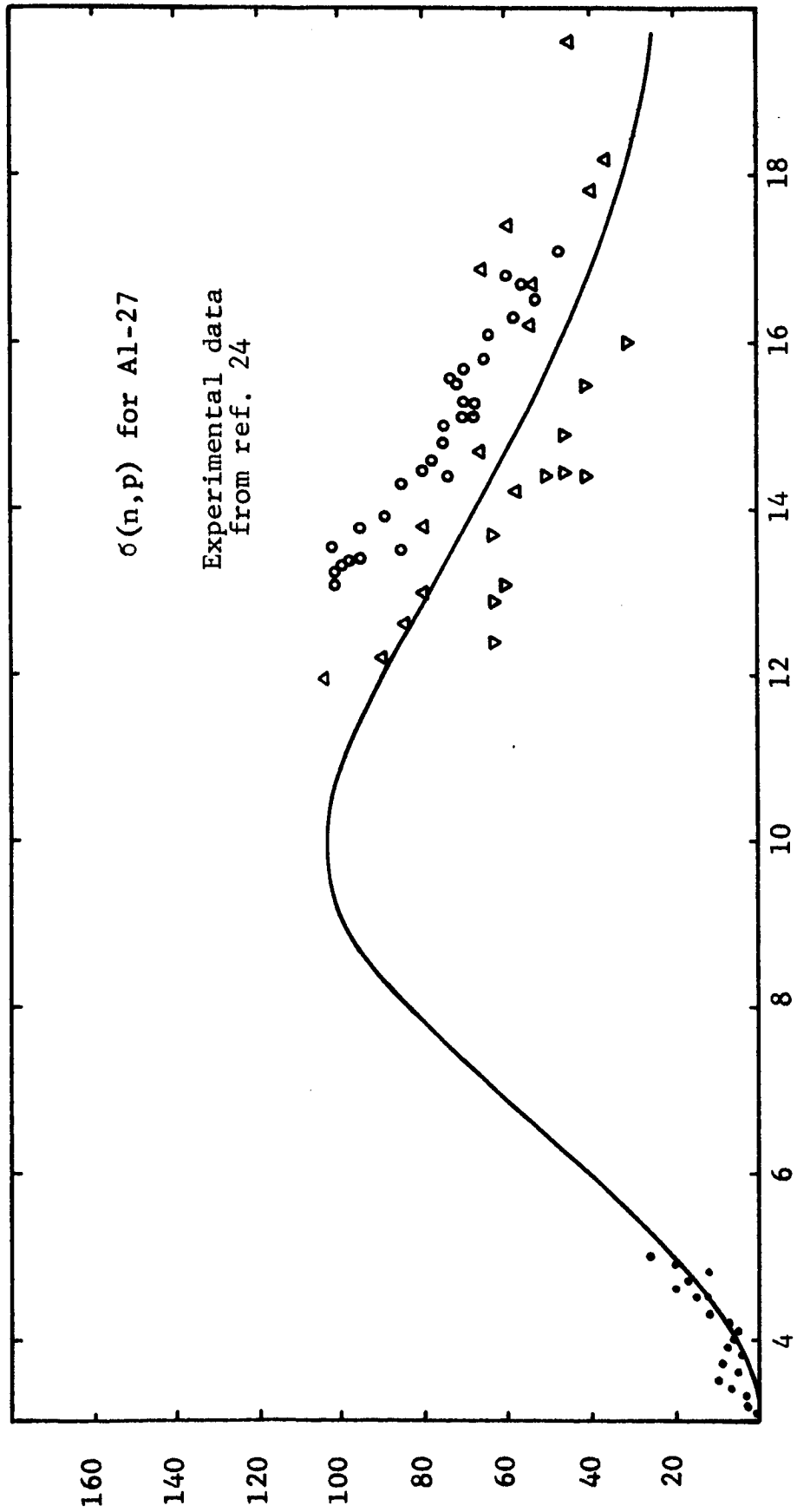
σ(n,α) for Al-27

Experimental data from ref. 24

CROSS SECTION (MILLIBARNS)

NEUTRON ENERGY (MEV)
FIGURE 18
ALUMINUM (n,α) CROSS SECTION
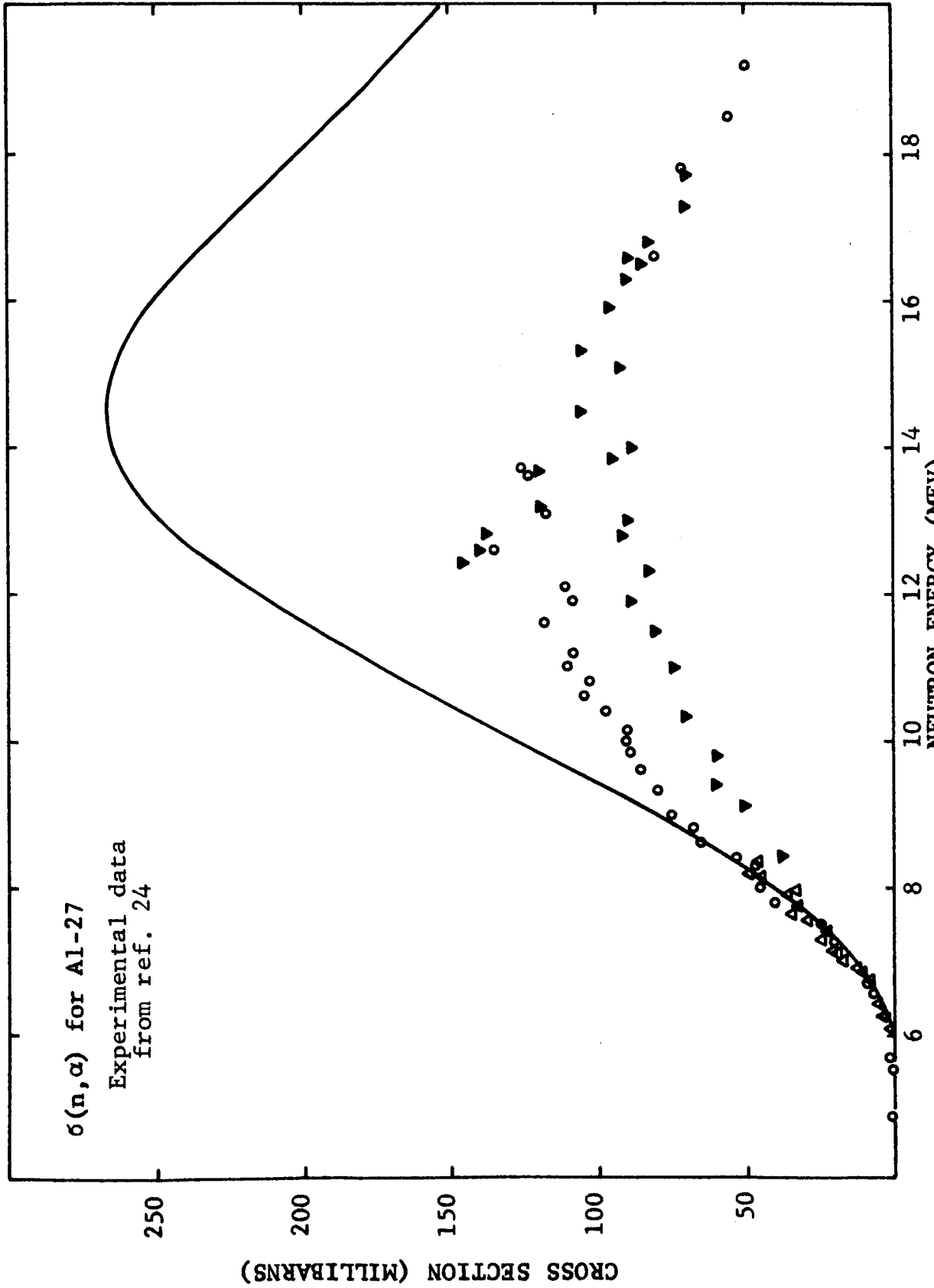
FIGURE 19

PHOSPHORUS-31 (n,α) CROSS SECTION

Experimental data from ref. 24

Neutron Energy (MeV)

Cross Section (barns)

69

Experimental data from ref. 30

Neutron Energy (MeV)

Cross Section (barns)

FIGURE 20

SULFUR-34 (n, α) CROSS SECTION

FIGURE 21

POTASSIUM-39 (n,α) CROSS SECTION

Experimental data from ref. 24

71
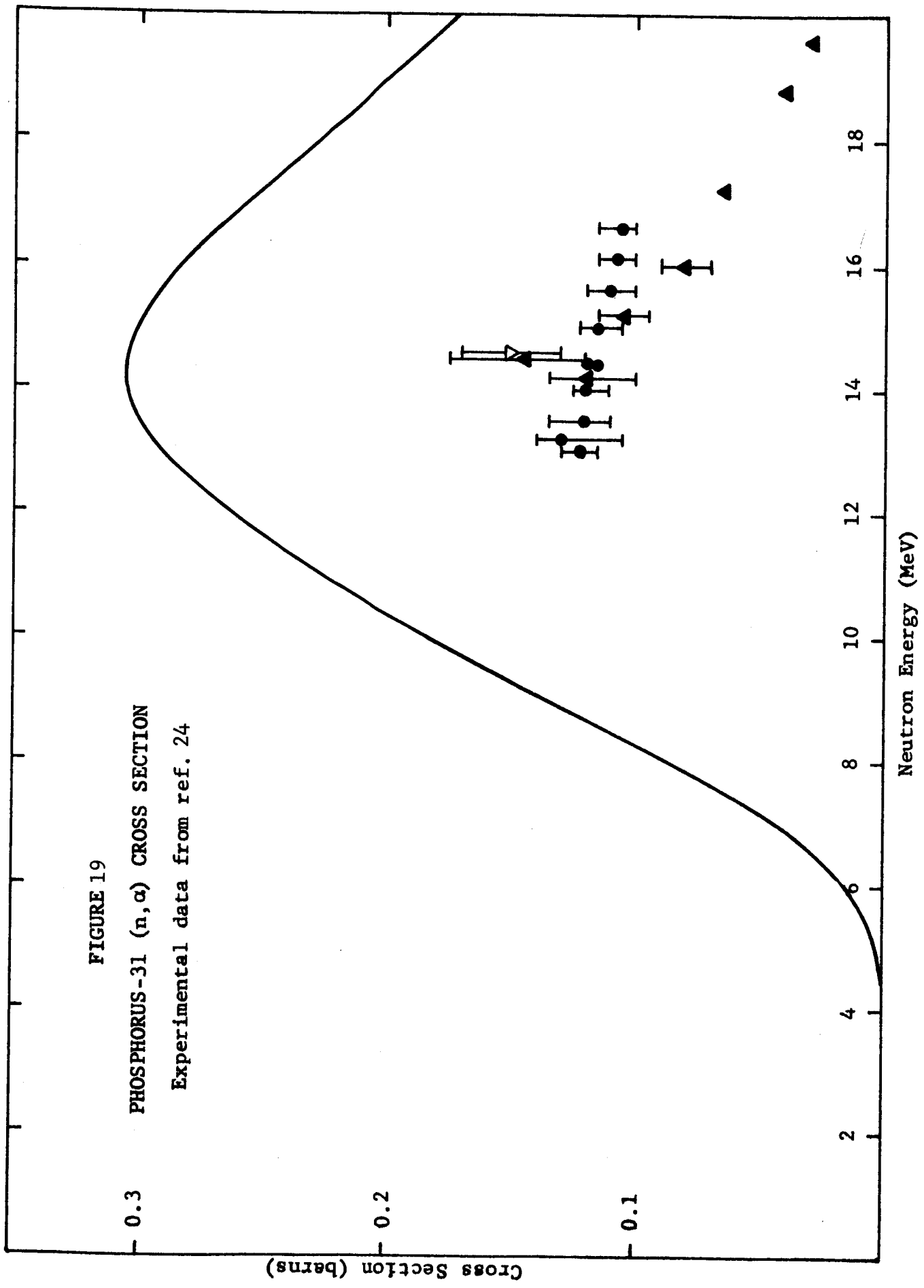
3.   (n,2n) Cross Sections

NAP calculations of (n,2n) cross sections, using the computational model discussed in section II-C-1, are compared with measured data in Figures 22-25.

Figure 22 compares the calculated and measured Al^{27} (n,2n) cross sections. The measured data are from Mani et al.(ref.31). Both the figure and Table 6 show that the threshold energy is calculated satisfactorily. The calculated cross section is in fair agreement with experiment, though somewhat high through much of the applicable energy range.

Figure 23 shows calculated and measured values of the (n,2n) cross section for Ni^{58}. The experimental data are quoted from both Jeronymo (ref. 27) and BNL-325 (ref. 32). The two sets of experimental data do not appear to be in good agreement with one another, and the calculated values do not agree well with either set of measured data. The calculated shape of the cross section is in qualitative agreement with the data. This disagreement is the worst found for (n,2n) cross sections, and may be due to closed shell effects as suggested by Barry (ref. 26) as in the case of the Ni^{58} (n,p) cross section.

Much better agreement is found in the case of Cu^{63}, as shown in Figure 24. The measured data are from Rayburn (ref.33). Excellent agreement between the calculated and measured data is obtained near the reaction threshold. The agreement is good up to at least 20 MeV, where the calculated values are about twenty per cent larger than the measured values.

Figure 25 shows a comparison between the calculated values of the (n,2n) cross section for I^{127} and the measured data of Martin and Taschek (ref. 34). The calculated threshold energy appears to agree with experiment and tabulated values (see Table 6), but the calculated cross sections appear to be about twice as large as the measured data away from the threshold. In any case, it appears that the NAP calculations of (n,2n) cross sections agree with experiment within a factor of two.

72
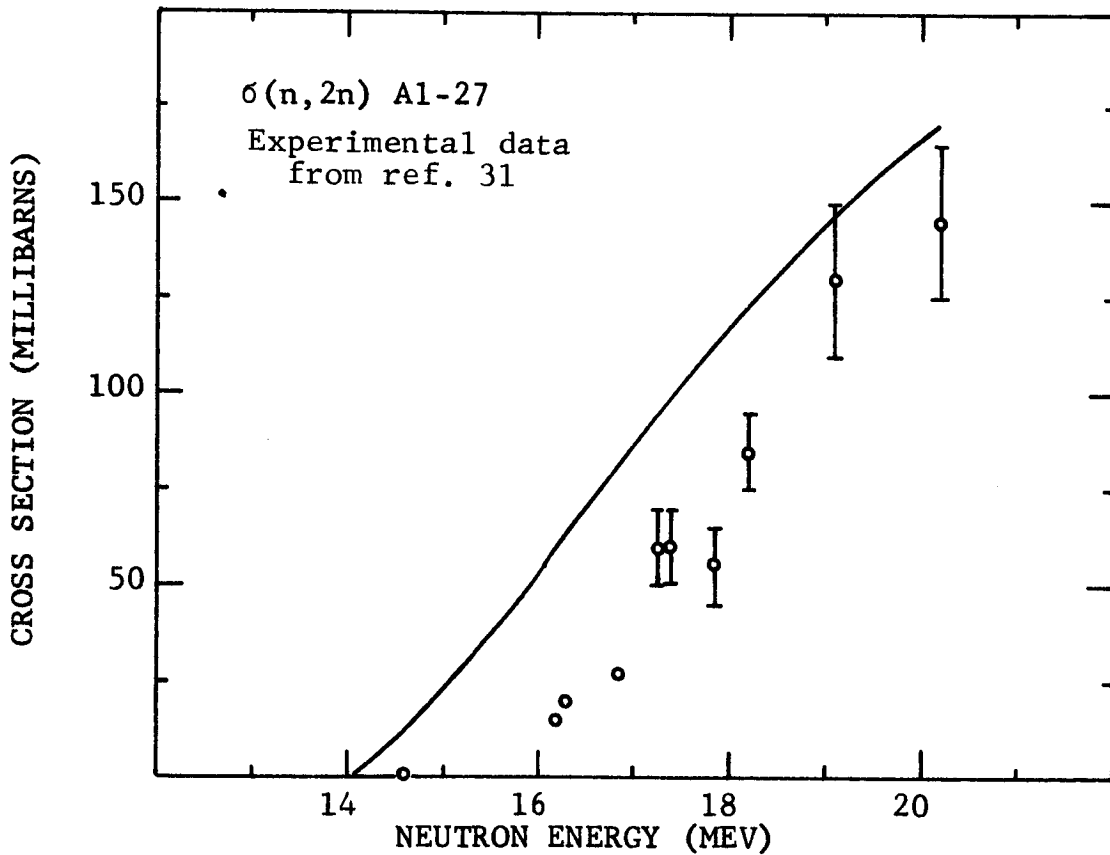
FIGURE 22

ALUMINUM (n,2n) CROSS SECTION
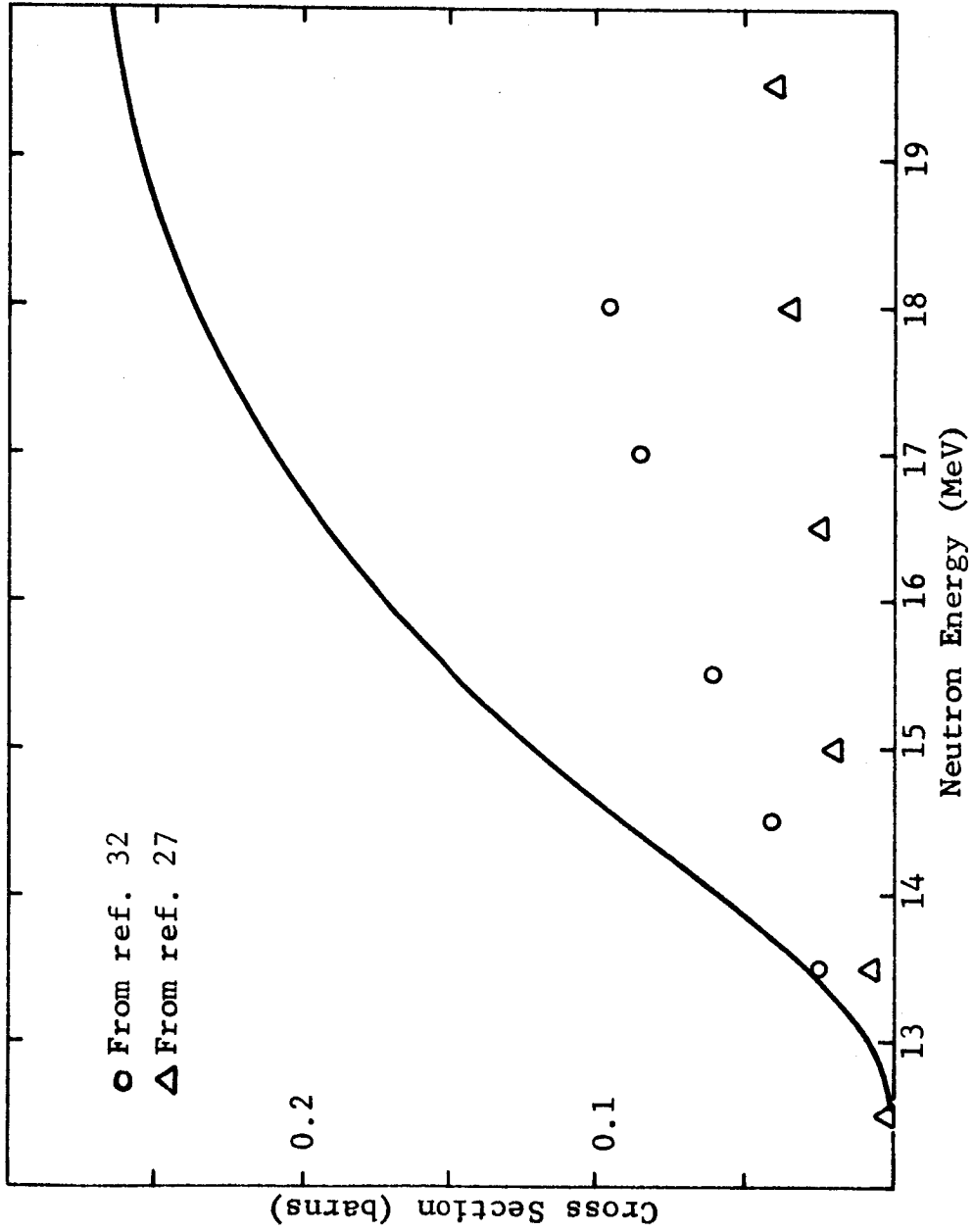
FIGURE 23

NICKEL-58 (n,2n) CROSS SECTION

74

σ(n,2n) Copper-63

Experimental data
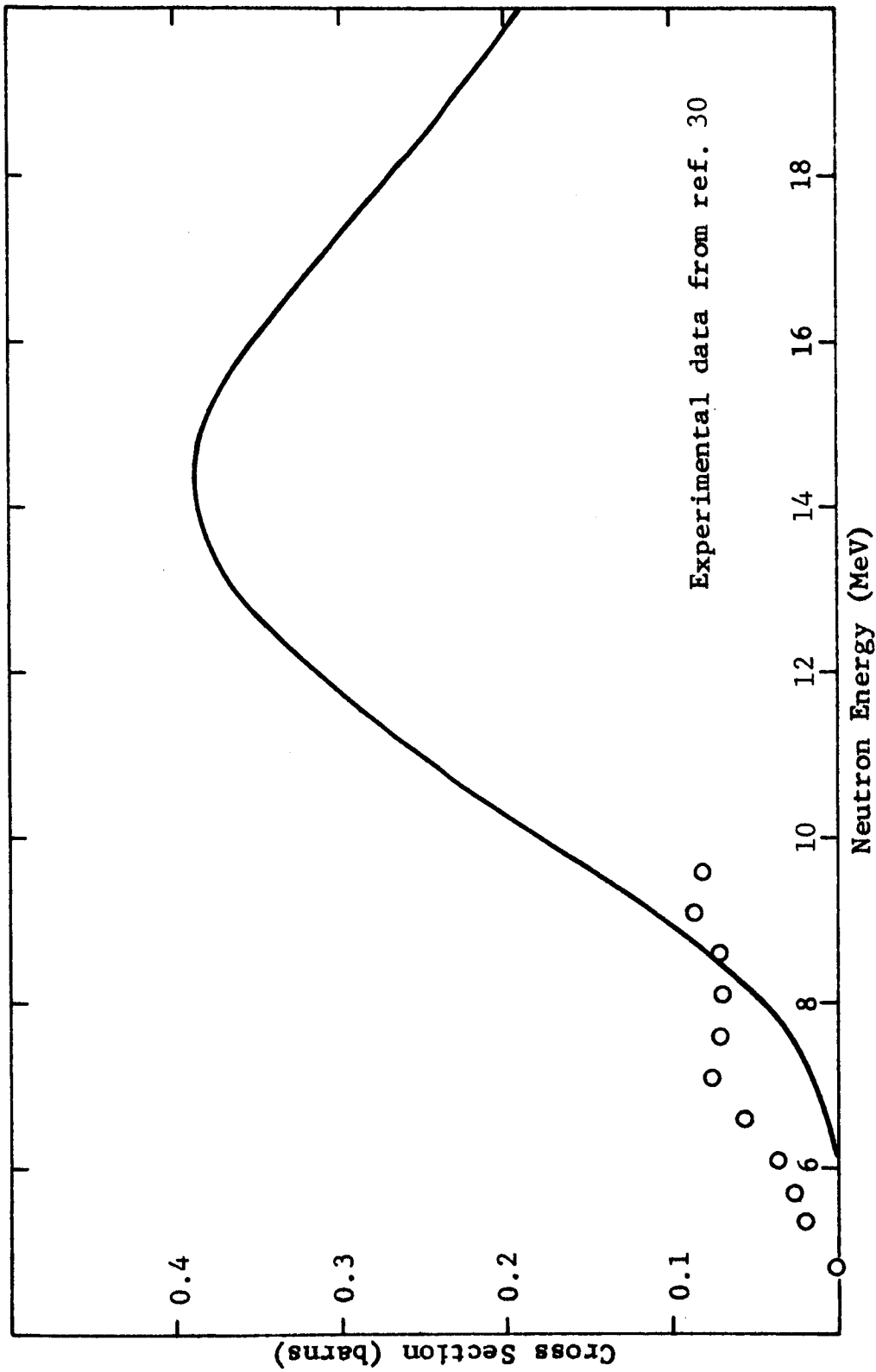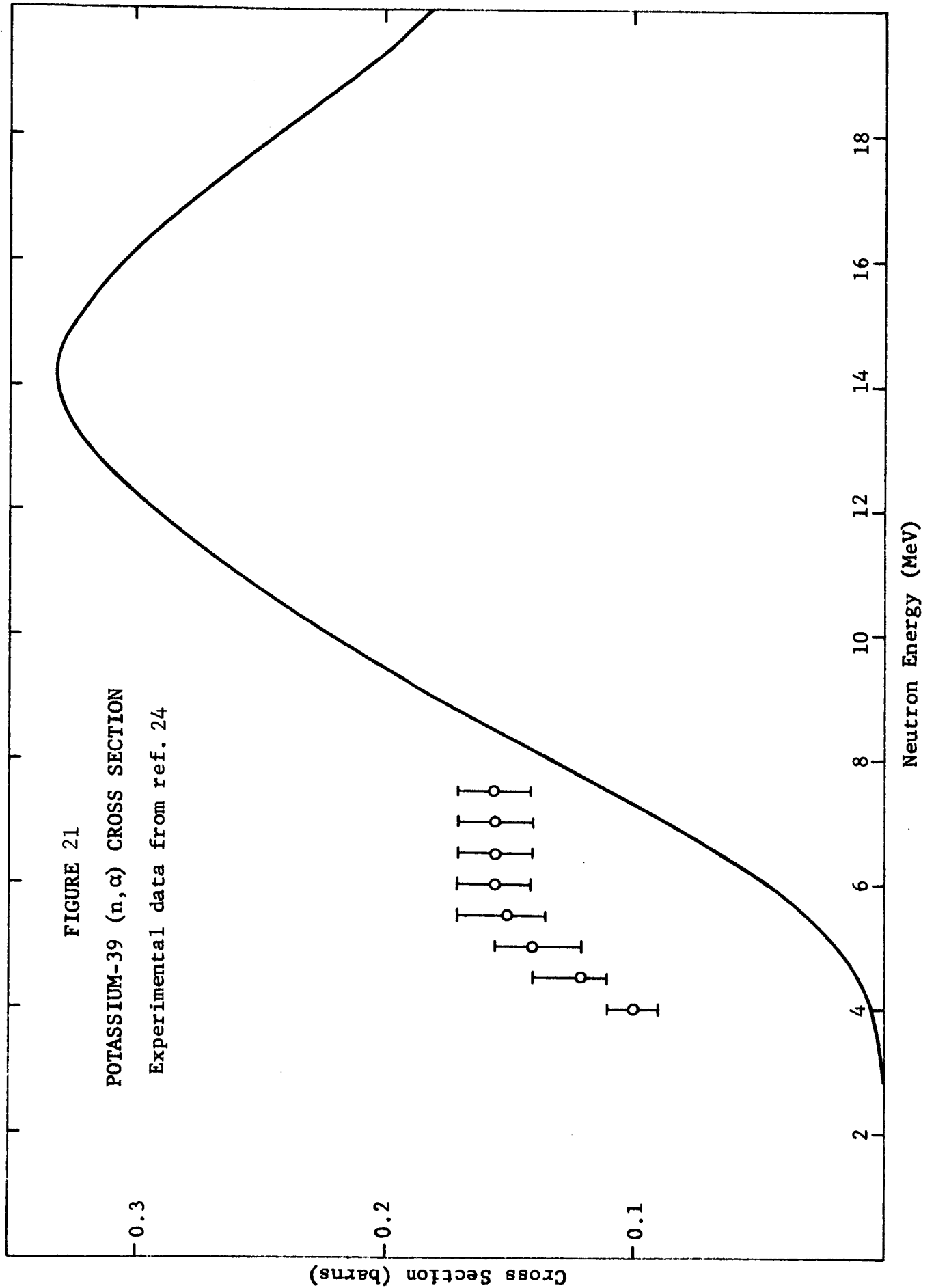from ref. 33
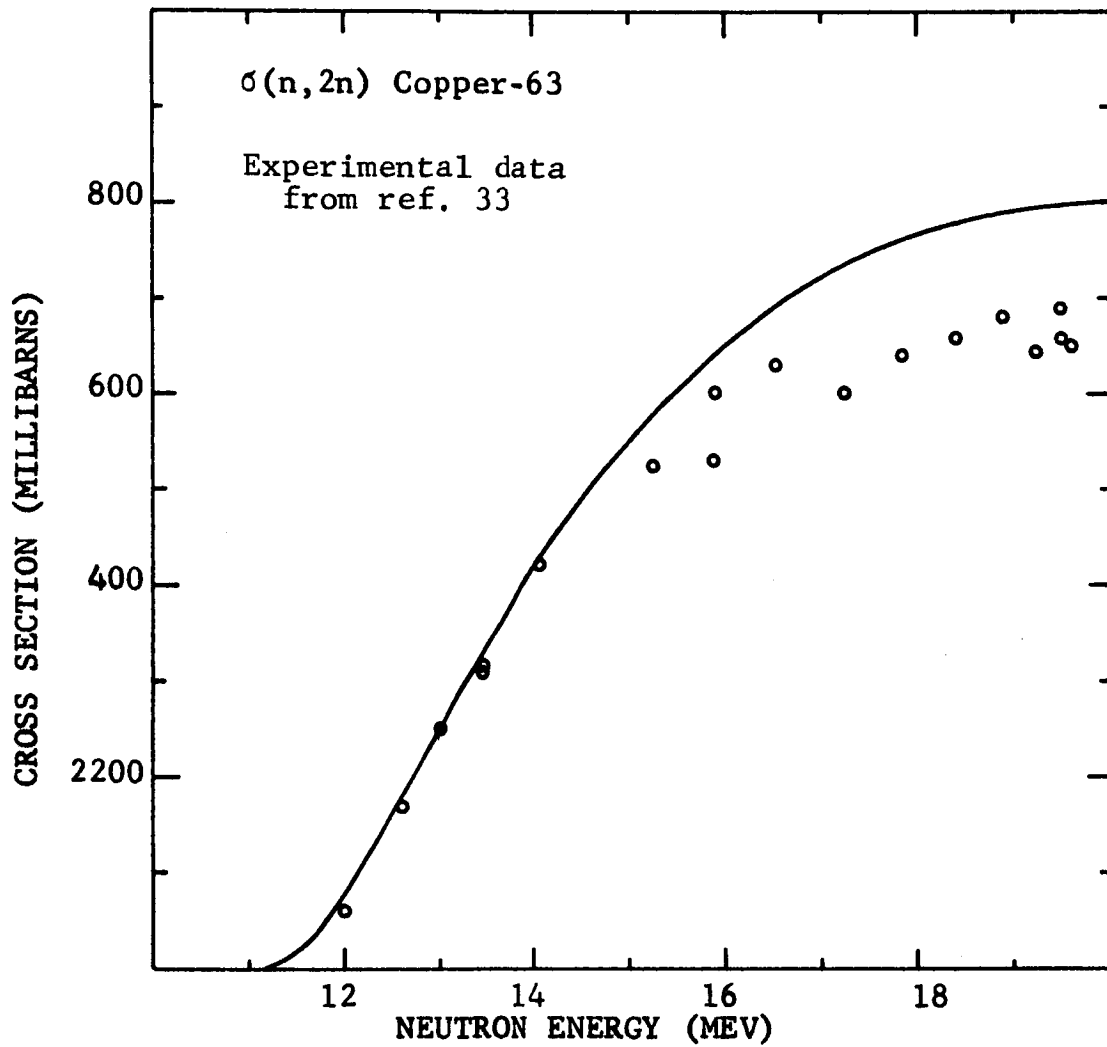
FIGURE 24

COPPER-63 (n,2n) CROSS SECTION

75
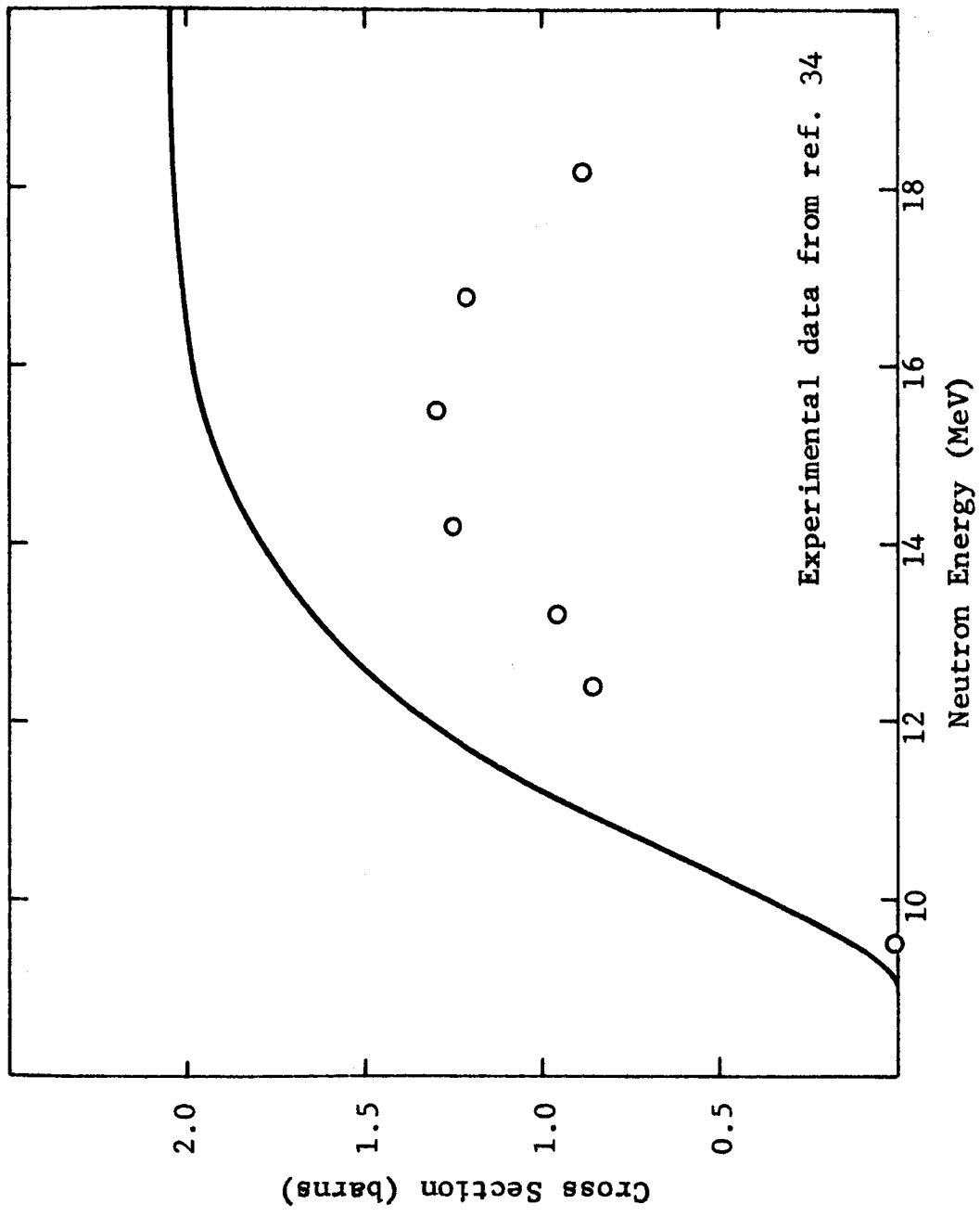
FIGURE 25

IODINE-127 (n,2n) CROSS SECTION

4. (n,γ) Cross Sections

NAP calculations of (n,γ) cross sections, using the computational model described in Section II-C-2, are compared with measured data for arbitrarily selected isotopes in Table 7. The calculated resonance integral has been obtained by using equation (91) and summing over all non-thermal neutron energy groups.

Table 7 indicates that neither thermal nor epithermal (n,γ) cross sections can be estimated with any accuracy using the methods outlined above. The measured thermal (n,γ) cross sections and resonance integrals span such a range of magnitude that any very simple systematic estimation scheme seems doomed to poor accuracy. In a sense, the inaccuracies of the (n,γ) estimation methods outlined here demonstrate that least squares is no substitute for physical insight. Nevertheless, for many isotopes, the thermal (n,γ) cross section can be estimated to within an order of magnitude. No similar statement can be made concerning epithermal (n,γ) cross sections, depsite the fact that the expressions given for f, D, and Γ_γ seem to fit the experimental data fairly well. It appears that no simple scheme involving only Z, A, and the even-odd character of the nucleus will provide good estimates of resonance integrals, at least until more experimental data become available.

In summary, unknown (n,p), (n,α), and (n,2n) cross sections can be estimated using the method summarized above. Comparison of calculated values to experimental data indicates that the method is accurate to a factor of two or so, for most isotopes. Similarly, unknown thermal (n,γ) cross sections can be estimated within one order of magnitude for many isotopes, and two orders of magnitude for most isotopes. It should be emphasized that the only input to the NAP computer subroutines using the simple formalism presented here consists of the Z and A of the target nucleus, and it must be emphasized that the resulting cross section estimates are used only to supplement measured data contained on the Cross Section Library tape.

Table 7

COMPARISON OF (n, γ) CROSS SECTIONS

	Thermal (n, γ) Cross Section (barns)		Resonance Integral (barns)	
Isotopes	Measured	Estimated	Measured	Estimated
Mn-55	13.2	11	14.2	675
Co-59	37.0	11	72.3	820
Cu-63	4.5	11	5.1	920
Ga-69	2.0	10	9.2	960
As-75	4.1	8	36.8	930
Br-79	10.4	6	147	870
Y-89	1.3	5	0.9	630
Nb-93	1.1	17	14	550
Mo-98	0.5	3	10.8	390
Rh-103	150.0	45	656	430
Ag-107	30.0	50	74	420
Ag-109	84.0	54	1160	420
In-115	200	57	2640	440
Sb-121	5.7	52	162	540
I-127	5.5	41	140	660
Cs-133	28	22	400	800
Pr-141	11.3	215	15.5	1050
Sm-152	216	160	2740	1200
Dy-164	2800	250	482	1400
W-186	34	210	396	1280
Au-197	99	120	1533	1060
Tl-203	11	22	129	870

C. Activation Calculations

1. Reactor Irradiations

The NAP computer program has been used to compute neutron
activation data for foils of gold, indium, and nickel. These
NAP calculation results were then compared to measured activa-
tion data obtained by irradiating gold, indium, and nickel foils
in the IITRI Research Reactor. These comparisons are essential
to the experimental validation of the NAP computer program.
The NAP calculations and comparisons with experimental data
are presented and discussed in Section a below, the experimental
details in Section b, and the determination of the neutron flux
incident upon the foils in Section c.

a.) NAP Calculations and Comparison with Experiment

Seven metal foils were exposed to a reactor neutron flux
by placement in Port "O" of the IITRI Research Reactor. Four
of these foils were gold, two indium, and one nickel. Two of
the gold foils and one of the indium foils were completely
enclosed by 0.035 inch of cadmium. All of the foils were high
purity 99+ %) natural elemental composition foils. The gross
physical properties of the foils are summarized in Table 8.
Each foil was individually placed in Port "O" and irradiated
for one minute, except the nickel foil, which was irradiated
for ten minutes. The reactor power was maintained at 60 kW
(kilowatts) and continuously monitored during the irradiation
period by observation of the power meter on the reactor operating
console.

A NAP activation calculation was performed for each of the
irradiated foils. The atom density used in the calculations
were obtained by using the measured masses and foil volumes
given in Table 8. All the calculations were single region
calculations using the Table 8 data for regional volumes and
thicknesses. It may be noted that the total number of atoms

Table 8

DESCRIPTION OF REACTOR-IRRADIATED FOILS

Foil	Shape	Area (cm^2)	Thickness (mils)	Mass (mg)	Cadmium Covered
Au #25	round	1.0	2.1	104.6	yes
Au #26	square	0.25	2.6	32.1	no
Au #27	square	0.25	2.7	33.3	yes
Au #28	round	1.0	2.0	100.3	no
In #13	square	0.25	2.0	9.4	no
In #14	square	0.25	1.7	8.0	yes
Ni #1	round	1.0	20.0	451.4	no

in the foil (or region) is then independent of the measured foil volume, and depends only upon the measured foil masses and assumed atomic weights.

The neutron flux at port "O" had been previously determined, and is given in Table 9. Ten neutron energy groups were used in most of the calculations. Since the flux shown in the table is based on reactor power level of 65 kW, while the foil irradiations were performed at 60 kW, the relative power level used in the calculations was taken as 60/65 or 0.9231. The absolute magnitude of the flux given in the table is accurate to $\pm$ 10 percent. Because of this error in the incident flux, the experimental error in the measured activation data and the size of the foils, use of the NAP neutron transport option to obtain thermal neutron self-shielding factors is ostentatious. Thermal neutron self-shielding was accounted for by multiplying the thermal flux given in Table 9 by the self-shielding factor given in equation (108) above, and using the resultant corrected thermal flux as input to the NAP calculations. Thus the thermal self-shielding factor was determined as 0.9357 for gold foil no. 26, 0.9468 for gold foil no. 28, and 0.9232 for indium foil no. 13. All other group fluxes were taken as shown in Table 9. However, for NAP calculations of the cadmium-covered foils, the thermal flux was taken as zero.

Results of the NAP calculations are displayed in Figures 26-32 which show selected gamma ray source strengths as a function of time after the foil irradiation. The NAP gamma ray energy structure was chosen to isolate the energy of the measured gamma photopeak. Measured gamma ray source strengths are indicated by the small circles and associated error bars. The error bars shown represent the nine-tenths error, i.e., if it is assumed that the errors follow the Gaussian law, there is a 90% probability that the correct value lies with the range indicated by the error bars. It should be emphasized that the NAP calculations are only as accurate as the incident flux and the cross sections used in the calculations. Since the incident

Table 9

NEUTRON FLUX SPECTRUM AT 65 KW

Group Number	Lower Energy Limit		$\int_{E_i}^{E_{i-1}} \emptyset(E)dE$ (neutrons/cm^2-sec
0	21.17	MeV	0
1	10.00	MeV	1.0×10^8
2	1.054	MeV	1.429×10^{11}
3	183.16	keV	1.721×10^{11}
4	24.788	keV	1.385×10^{11}
5	1.2341	keV	1.700×10^{11}
6	167.02	eV	1.021×10^{11}
7	22.603	eV	0.951×10^{11}
8	3.9728	eV	0.786×10^{11}
9	0.53138	eV	0.843×10^{11}
10	0.001	eV	7.763×10^{11}

Figure 26

GOLD FOIL No. 25
(cadmium-covered)

83
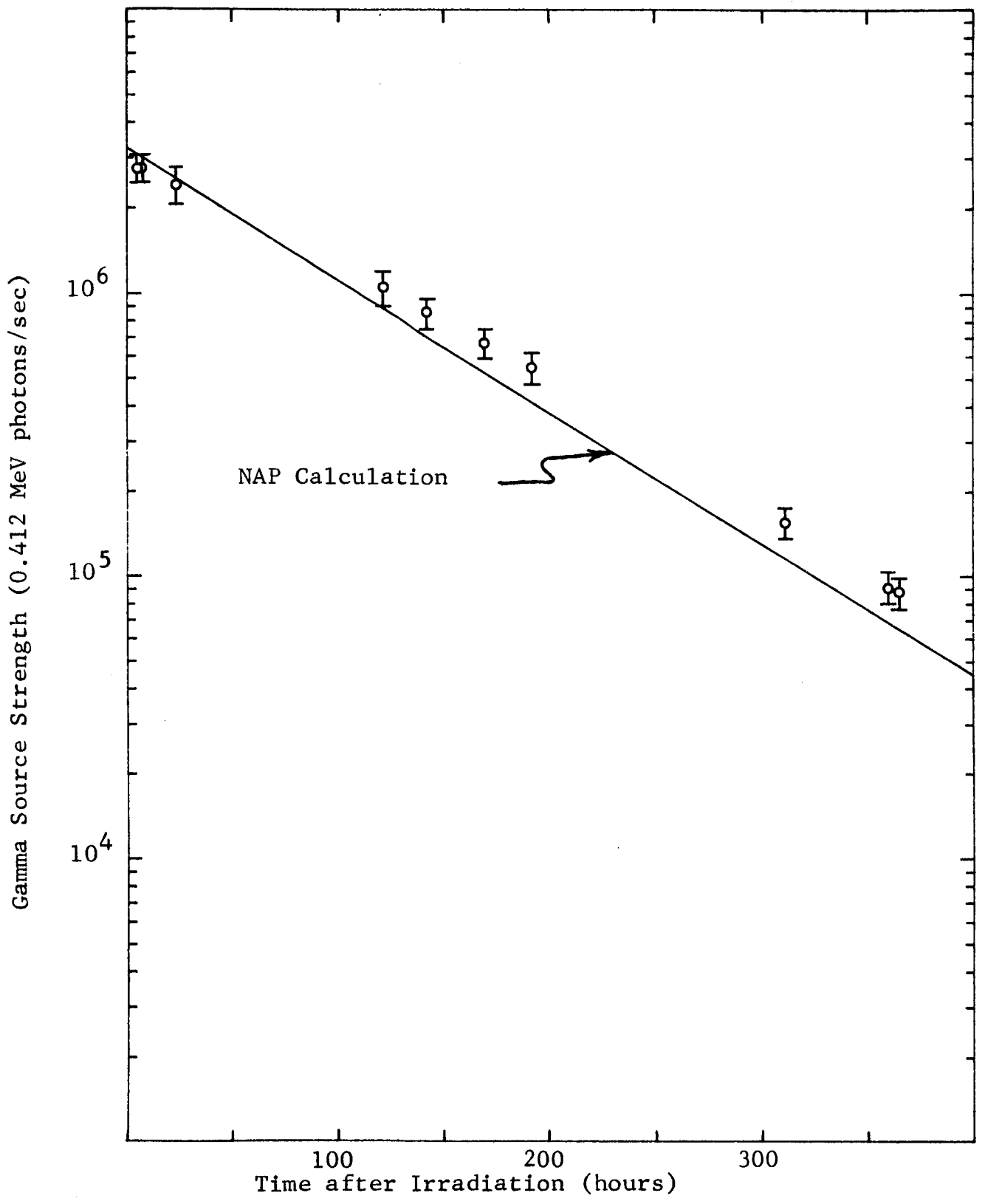
Figure 27

GOLD FOIL No. 28
(bare)

84
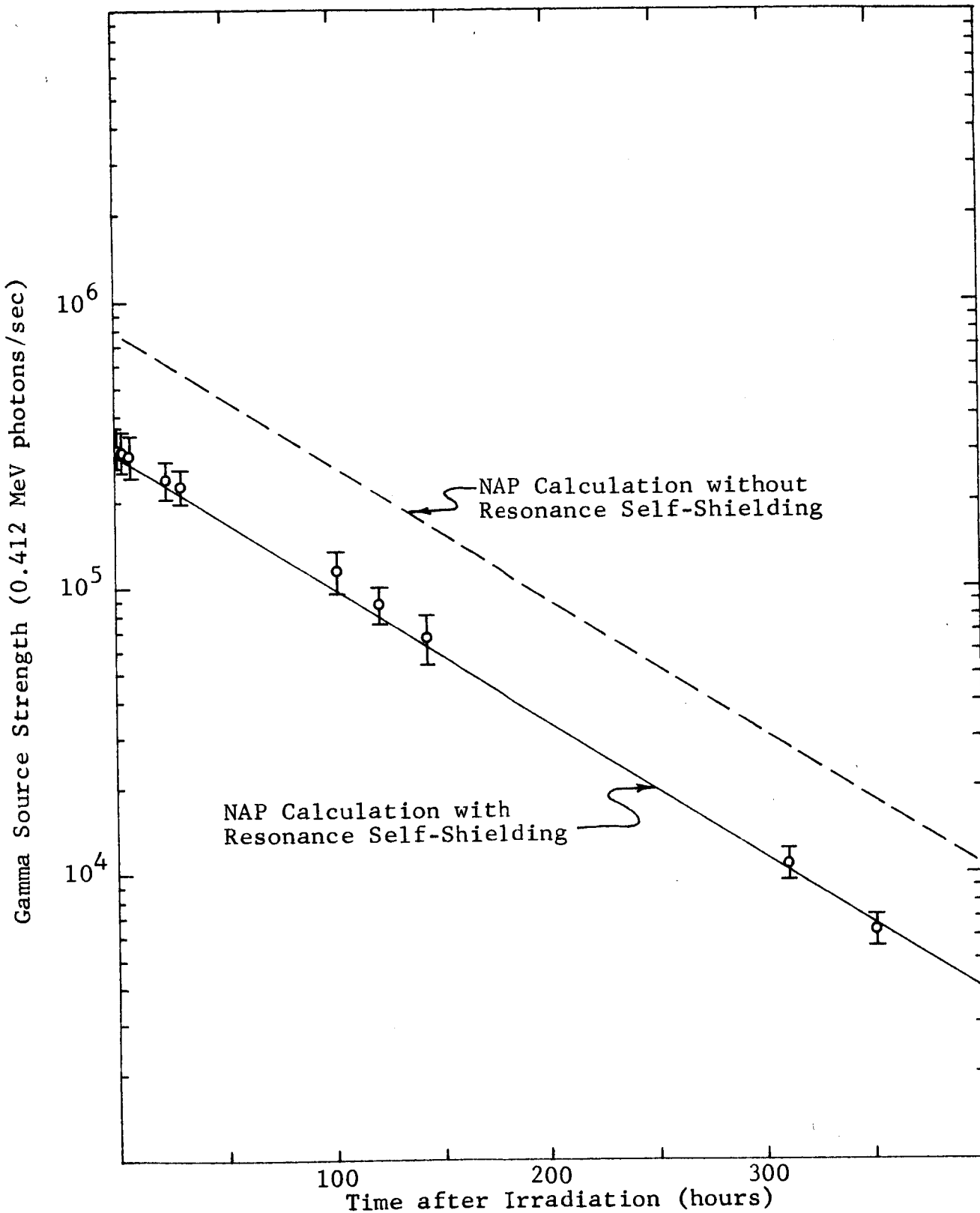
Figure 28

GOLD FOIL No. 27
(cadmium-covered)

Figure 29

GOLD FOIL No. 26
(bare)
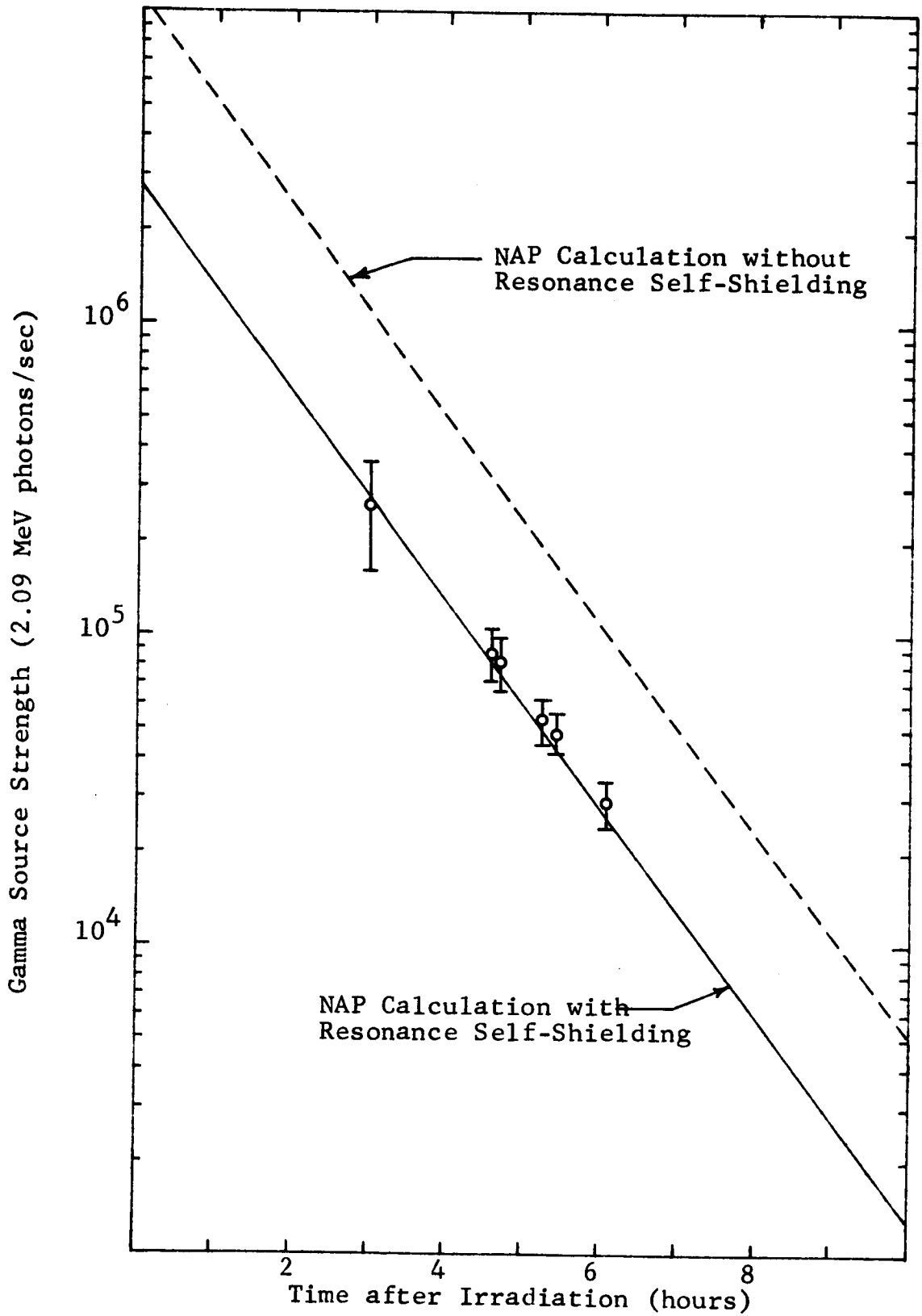
Figure 30

INDIUM FOIL No. 14
(cadmium-covered)
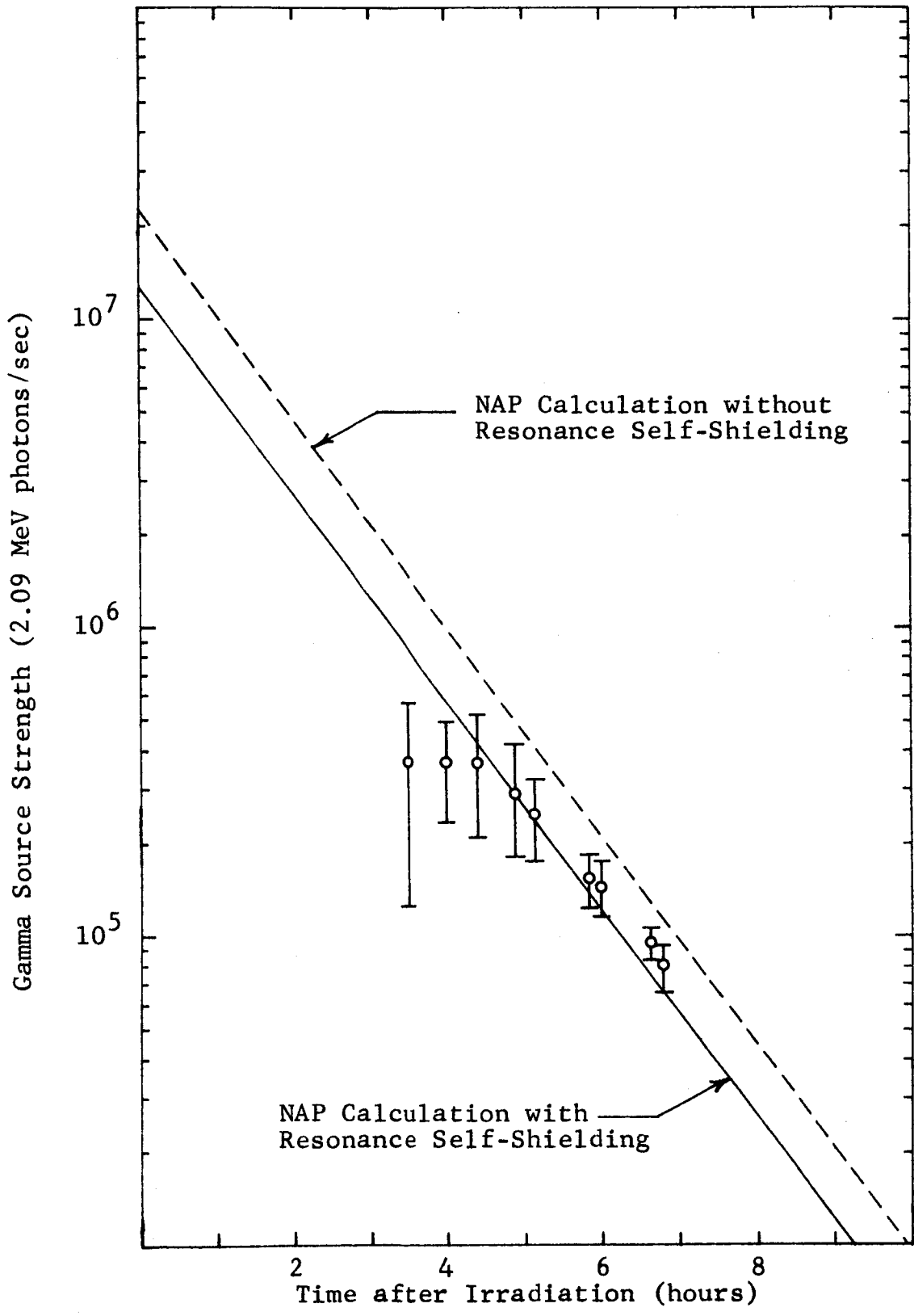
Figure 31

INDIUM FOIL No. 13
(bare)
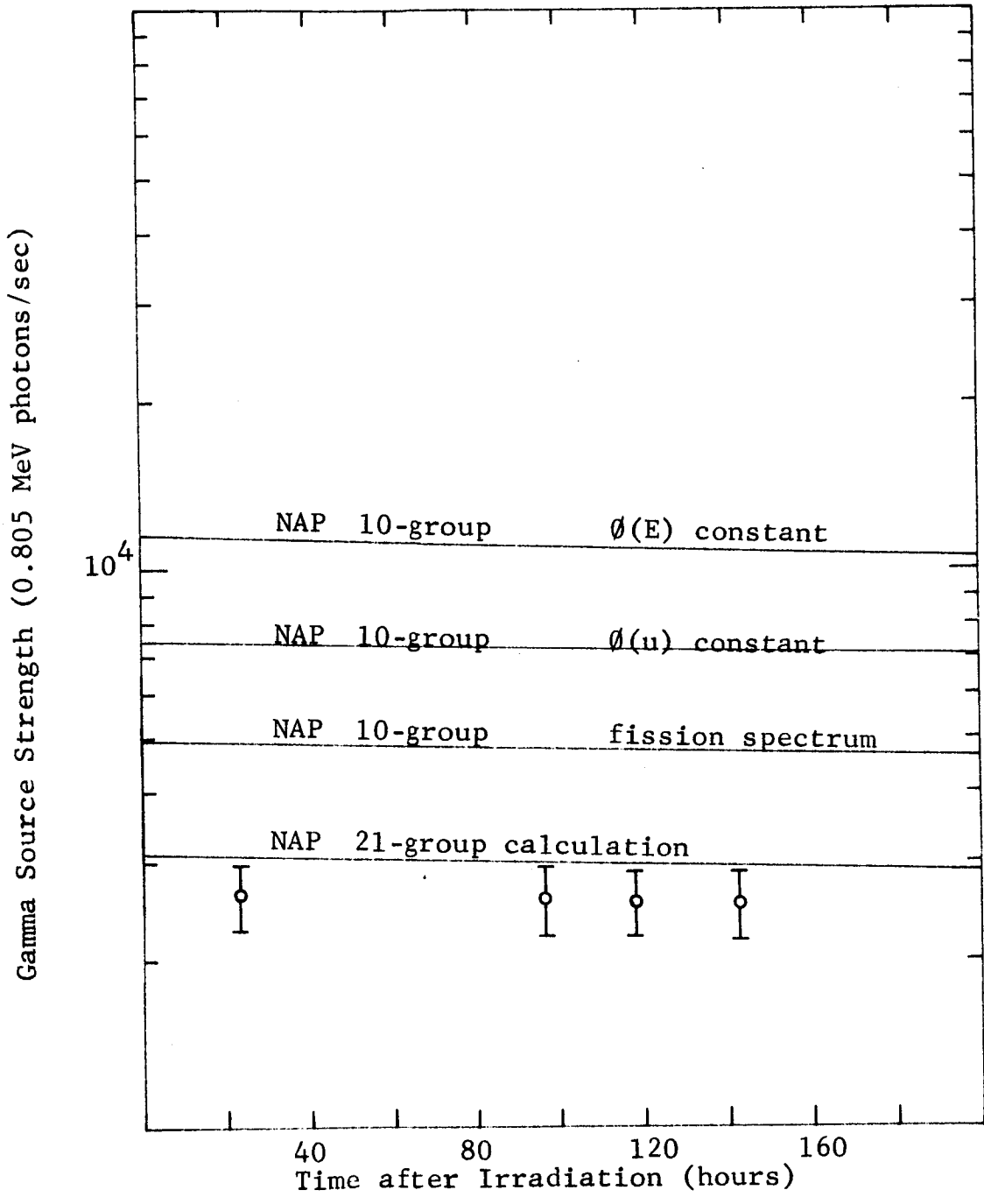
Figure 32

NICKEL FOIL No. 1

89

flux is assumed to be known to ± 10 percent, the NAP calculations are accurate to ± 10 percent, _if_ the cross sections are assumed to have no error. Thus if the NAP calculations agree with the measured data to within 10 percent, the NAP calculations may be said to agree with the measured data within the experimental error. With this in mind, excellent agreement is obtained between the NAP calculations and the measured data.

Comparison of Figure 26 with 27, 28 with 29, and 30 with 31 show that both thermal and epithermal neutron activations are properly accounted for by the NAP computer program. Each pair of comparisons deals with nearly identical foils, except that one foil was enclosed by cadmium during the irradiation while the other foil was not. The cadmium-covered foils are subject only to epithermal activation, while the bare foils are subject to both thermal and epithermal activation. The apparent lack of agreement between the NAP calculations and the measurements for indium foil no. 13 at less than five hours after irradiation is due to pulse pile-up at high counting rates and uncertainty in the background correction. This is discussed further in Section b.

Some difficulty was encountered during preliminary NAP calculations of epithermal neutron activation. In particular, the NAP code as originally programmed did not account properly for resonance neutron self-shielding effects. These effects can be very significant, even for thin foils. The dashed line in Figure 28 shows the results of preliminary NAP calculations, which ignored resonance self-shielding effects, of induced activation in the cadmium-covered gold foil no. 27. The original results are seen to be in error by almost a factor of three. The cadmium cover enclosing the foil results in an emphasis of effects of resonance self-shielding, since virturally all of the induced activity is due to epithermal neutron capture. Figure 29 shows similar results for gold foil no. 26, which was not enclosed by cadmium. In this case,

90

there is a significant activity contribution from thermal
neutron capture, which is not affected by resonance self-
shielding. Consequently, the error in ignoring this self-
shielding is reduced to about a factor of two. Very similar
results are shown in Figures 30 and 31 for indium foils. These
comparisons of preliminary NAP calculations with experiment
indicated a need for modification of the original NAP program.

The neutron transport NAP option was not suitable for
treating resonance self-shielding in detail, and therefore
the NAP program was appreciably altered to provide automatic
computation of resonance neutron self-shielding effects. The
modifications involved both programming changes in the NAP
code itself and inclusion of resonance parameters in the NAP
Cross Section Library. The physical model used as the basis
for the modifications is discussed in detail in Section II-C-2-a.
The adequacy of this treatment is proven by the excellent
agreement between NAP calculations and experiment as shown in
Figures 26 through 31. A detailed numerical comparison showing
the effect of resonance self-shielding on the calculated
activation of gold foil no. 26 is provided by comparing Tables
10 and 11. Table 11 gives the calculated activation gamma ray
spectrum when resonance self-shielding effects are properly
accounted for, while Table 10 gives corresponding calculated
data when such effects are ignored.

The results of using the NAP program to compute activation
gamma rays resulting from a threshold reaction are shown in
Figure 32. The experimental data were obtained by irradiating
a pure elemental nickel foil in port "O" of the IITRI Research
Reactor for ten minutes at 60 kW. Most of the gamma rays
result from disintegration of Co^{58} produced by the (n,p)
reaction of Ni^{58}. This reaction has a threshold of about one
MeV and the calculated activity is quite sensitive to the input
flux spectrum above this threshold.

Table 10

CALCULATED GOLD FOIL No. 26 ACTIVITY

(unshielded)

Time after Irradiation (hours)	Photon Source Strength (photons/sec)			
	2-0.8 MeV	0.8-0.6 MeV	0.6-0.3 MeV	0.3-0.05 MeV
0	3866	2.126×10^4	1.933×10^6	0
1.050	3822	2.102×10^4	1.911×10^6	0
3.317	3731	2.052×10^4	1.865×10^6	0
6.617	3601	1.981×10^4	1.800×10^6	0
23.467	3006	1.653×10^4	1.503×10^6	0
30.700	2782	1.530×10^4	1.391×10^6	0
94.883	1398	7689	6.990×10^5	0
120.83	1059	5822	5.293×10^5	0
143.75	828.0	4554	4.140×10^5	0
311.82	136.7	751.6	6.833×10^4	0
360.50	81.1	446.1	4.055×10^4	0

Table 11

CALCULATED GOLD FOIL No. 26 ACTIVITY

(shielded)

Time after Irradiation (hours)	Photon Source Strength (photons/sec)			
	2-0.8 MeV	0.8-0.6 MeV	0.6-0.3 MeV	0.3-0.05 MeV
0	2256	1.241×10^4	1.128×10^6	0
1.050	2230	1.227×10^4	1.115×10^6	0
3.317	2177	1.197×10^4	1.088×10^6	0
6.617	2101	1.156×10^4	1.051×10^6	0
23.467	1754	9647	8.770×10^5	0
30.700	1623	8927	8.116×10^5	0
94.883	815.7	4487	4.079×10^5	0
120.83	617.7	3397	3.088×10^5	0
143.75	483.1	2657	2.416×10^5	0
311.82	79.74	438.6	3.987×10^4	0
360.50	47.32	260.3	2.366×10^4	0

Figure 32 shows NAP results using a ten-group neutron energy structure (given in Table 9) and also a 21-group neutron energy structure which was designed to provide a more accurate description of the incident neutron flux above one MeV. If the 43-group NAP Cross Section Library is utilized with a more coarse input neutron energy group structure, three options are available for averaging the library group cross sections to obtain group cross sections in an energy structure consistent with the input neutron energy group structure. In effect, these options assume that in a single input neutron energy group which is broad enough to contain more than one library neutron energy group, the input flux per unit energy is distributed among the library energy groups according to (1) a constant flux per unit energy spectrum, (2) a flux per unit energy spectrum which is distributed in energy as 1/E, and (3) a fission flux spectrum. Option two is identical with assuming a constant flux per unit lethargy. These options were provided to enhance the flexibility of the NAP code, and to simplify the input data preparation when the input flux spectrum is known to fall into one of the above three categories or to enable automatic estimation of the flux spectrum when it is only known crudely.

The results of the NAP ten-group calculations of nickel foil activity are seen in Figure 32 to be quite sensitive to the library cross section weighting option chosen. The ten-group structure used provides only a single neutron energy group from 1.054 to 10 MeV. Assuming that the flux spectrum in this energy range is a constant per unit energy is completely inadequate. Assuming that the flux per unit lethargy is constant is somewhat better, though still inadequate. Assuming that a fission spectrum is appropriate in this energy range is still better, but inadequate, because the irradiation position is in the reflector of the IITRI Research Reactor where the flux is significantly degraded from a fission spectrum. In this case, only a more finely detailed energy description of the incident

flux provides reasonable results, as shown in Figure 32 by
the results of the 21-group calculation. Here the energy
structure was selected to provide nine energy groups between
one and ten MeV. Again noting that the neutron flux incident
upon the nickel foil is known only to ten percent, the agree-
ment between the 21-group NAP calculation and the measured
data must be regarded as excellent.

The nickel foil NAP calculations may be understood in
detail by reference to Figure 33. Superimposed upon the
$Ni^{58}(n,p)$ cross section are the various assumed flux spectra.
The determining quantity in computing the gamma ray activity
is the product of the cross section and the flux. Relative
to the measured flux spectrum, the use of a constant flux per
unit energy spectrum overweighs the cross section where it is
large and underweighs the cross section where it is small.
This leads to a gross overestimate of the appropriate reaction
rate and hence an overestimate of the gamma ray activity. A
similar situation exists when a constant flux per unit lethargy
is used, or when a fission spectrum weighting is used. It is
interesting to note that the measured flux spectrum contains a
larger fraction of one to two MeV neutrons than appropriate to
a fission flux spectrum. This is presumably due to the ir-
radiation position being located in the reactor reflector,
with some three inches of graphite lying between the core and
the irradiation position. Fast neutrons arriving at the foil
have therefore originated in the reactor core and diffused
through the graphite, with the concomitant energy losses in
scattering collisions with the graphite nuclei. Had the nickel
foil been irradiated inside the reactor core, a ten-group NAP
calculation with fission spectrum weighting of the library
cross sections would have resulted in much better agreement
with experiment than shown in Figure 32.

In summary, NAP calculations of gamma activity of
selected gamma energies due to exposure of gold, indium, and
nickel foils to reactor flux spectra, both with and without a

95
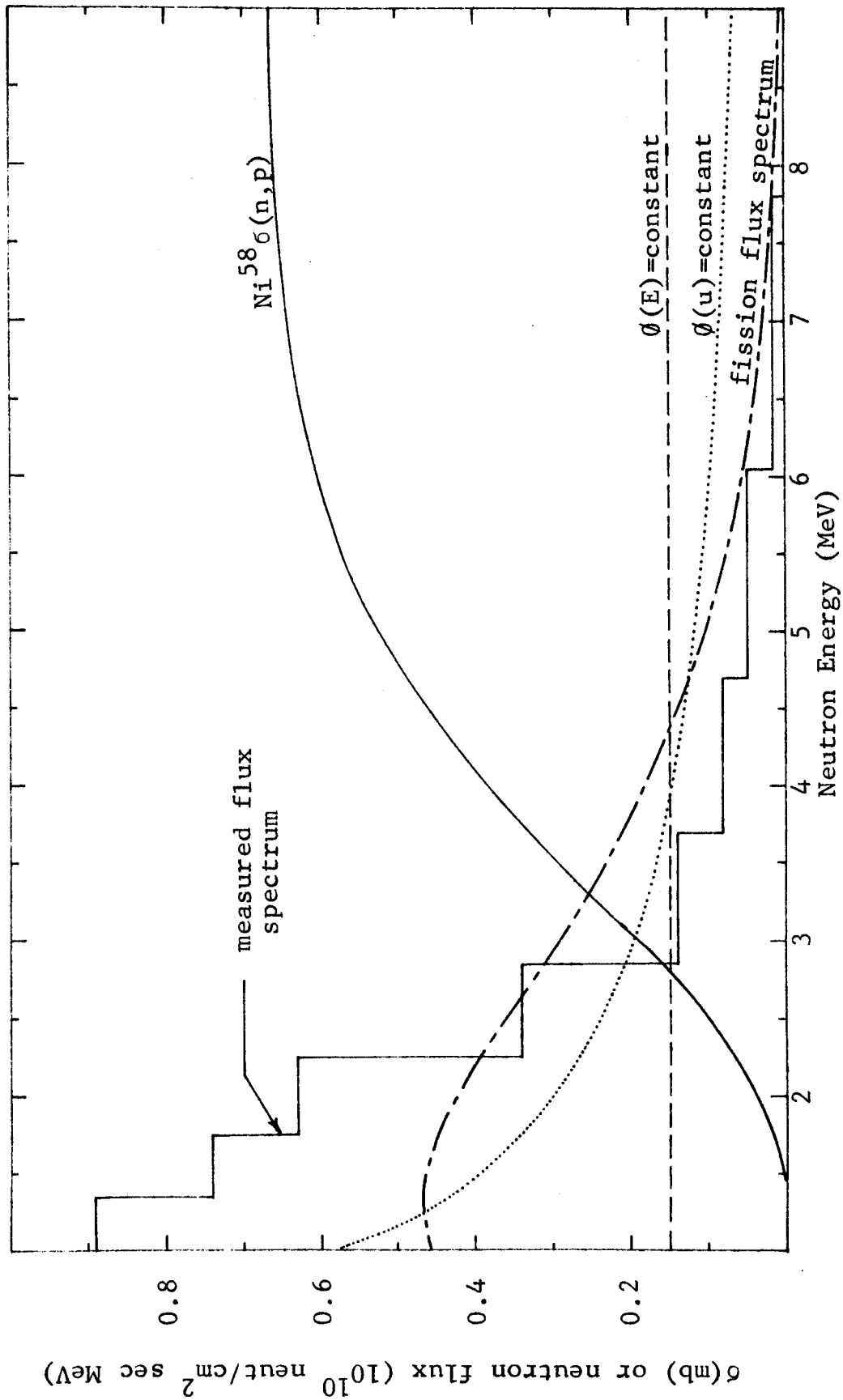
Figure 33

Ni$^{58}\sigma(n,p)$ and
NEUTRON FLUX SPECTRUM

96

thermal flux component, have shown excellent agreement with measured gamma activities. There are certain errors inherent in almost any NAP calculation. These errors are due exclusively to a lack of precise knowledge of the physical world, and are not due to deficiencies in the analytical models used in the NAP program. The most obvious source of error is lack of precise knowledge of the incident neutron flux. Clearly, the NAP results can be no more accurate than the input flux used in the calculations. The error in the flux used in the calculations reported above has been estimated as ten percent. An equally important source of error lies in the reaction cross sections used in the calculations. It has been demonstrated above that effective resonance cross sections are adequately computed. However, the basic cross section data contained in the NAP Cross Section Library contains some experimental error (sometimes large), which must be considered on an individual cross section basis. Similar comments apply to the NAP Gamma Radiation Library which contains isotopic decay schemes and pertinent data including half-lives, gamma ray energies, fractional gamma ray emission probabilities, and decay branching ratios. Detailed consideration of effects of cross section and decay data errors on the results reported above are beyond the scope of this discussion. What has been shown above is that if an input flux known to ten percent is properly used in NAP calculations of gold, indium, and nickel foil activities, the calculated data agrees with the measured data to within ten percent. Since the pertinent cross sections and gamma ray emission probabilities are not known exactly, the agreement reported above must be regarded as truly outstanding.

The experimental data summarized above are described in detail in the following two sections. This is followed by a section dealing with the experimental validation of the NAP code in the case of irradiation in a non-reactor environment and with an arbitrary time dependence.

b.) Measurement of Gamma Ray Activities

As stated above, four gold foils, two indium foils, and one nickel foil were irradiated in port "O" of the IITRI Research Reactor. NAP calculations and their comparison with experimental data has been described in the preceeding section. This section discusses the obtaining and subsequent analysis of that experimental data.

The gross physical properties of the foils have been summarized in Table 8 above. The foils were individually irradiated in port "O" (see Figure 34) between 0954 and 1037 on 11 February 1965. The reactor power level was maintained at 60 kW throughout each irradiation period. The nickel foil was irradiated for ten minutes, all other foils for one minute.

After removal from the reactor room, each foil was individually placed in a lead cave for gamma ray counting. The cave, used to reduce the level of extraneous background radiation, consisted of four-inch thick lead walls and had interior dimensions of 12 x 12 x 22 inches, the long side being vertical. The interior of the cave was lined with 0.065 inch thick cadmium sheeting and 0.0165 inch thick copper sheeting on all sides. The cadmium sheeting attenuated the lead 72 keV x-ray emanating from the cave walls, while the copper attenuated electrons arising from photoelectric x-ray absorption in the cadmium.

A 3 x 3 inch NaI detector was used to count the gamma ray activity. Each foil was mounted along the vertical axis of the NaI crystal at a distance of ten centimeters from the top fact of the crystal. An x-ray photograph of the detector indicated that the aluminum cap on the top face of the crystal was 9/64 inch thick. A 1/2 inch thick lucite slab, which acted as a beta particle absorber, was placed on the detector top. The gamma ray spectra were counted using a Nuclear Data Series One-Thirty 512-channel analyzer, although only 256 channels were used for the actual foil counting. The other 256 channels were used for continuous background monitoring

98

IIT RESEARCH INSTITUTE REACTOR

FIGURE 34

99
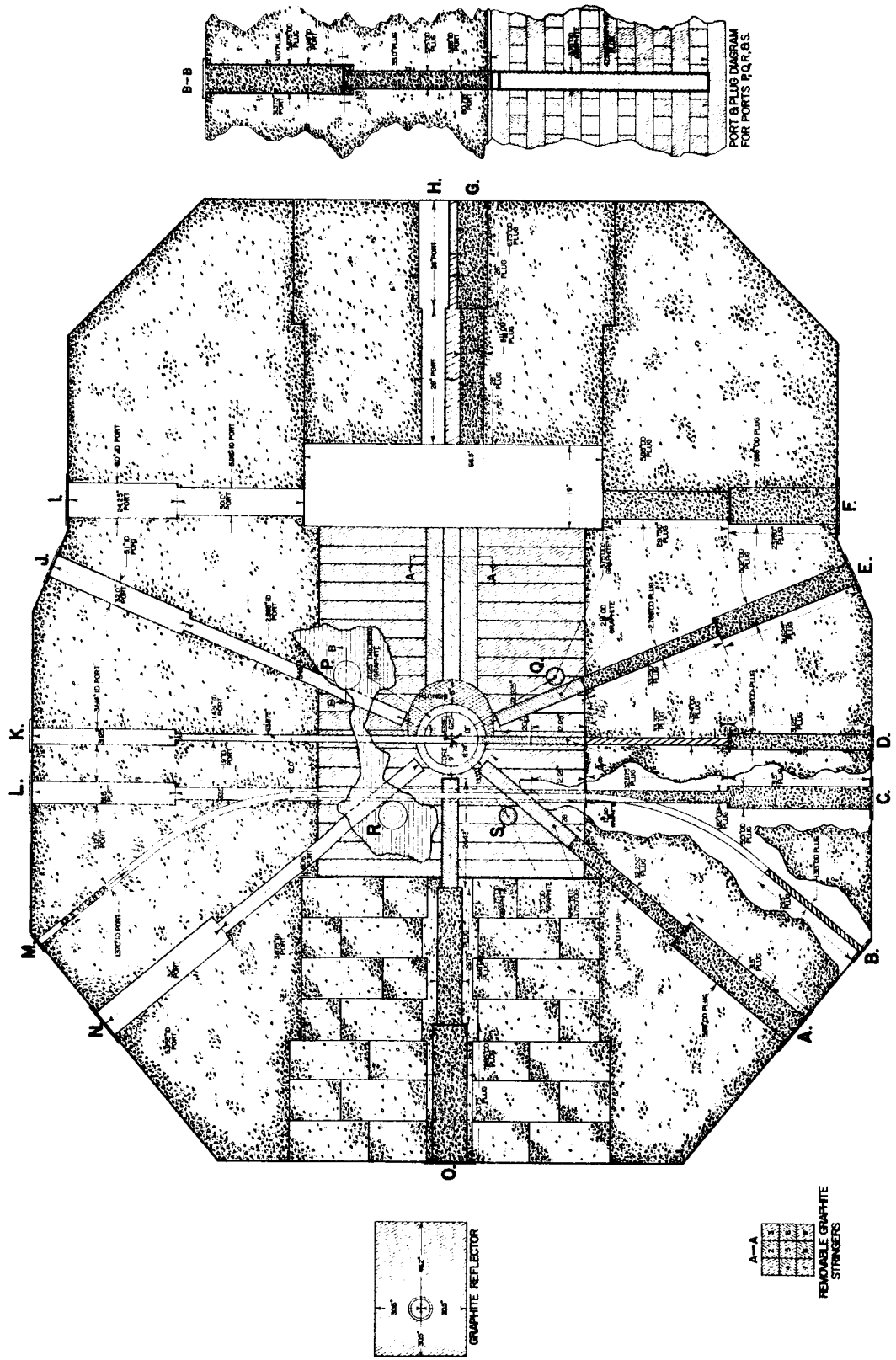
and energy calibration. A typical gamma ray spectrum obtained from one of the gold foils is shown in Figure 35.

For gamma ray photopeak analysis, a computer code (ref. 35) developed at General Atomic was modified for use on this project. The computer program first finds the low-energy bound and the high-energy bound of the peak. The channel counts near the low-energy bound are approximated by a second order polynomial, while the channel counts near the high-energy bound are approximated by a Gaussian function. The total area under the peak is obtained by simply adding up all the counts between the low-energy bound and the high-energy bound. In previously reported preliminary results, the background was defined as that trapezoidal area under the straight line (on a semilogarithmic scale) connecting the low-energy and high-energy bounds (the cross-hatched area B in Figure 36). This background area was then subtracted from the total area to obtain the peak area. This popular technique provides no estimate of the error in the background correction. An alternative definition of background is shown by the doubly cross-hatched area C in Figure 36. This area consists of a rectangular area of width equal to the width of the photopeak and height equal to the gamma ray count at the high-energy bound plus the triangular area of base equal to one-half the photopeak width and height equal to the gamma ray count at the low-energy bound minus the gamma ray count at the high-energy bound. For photopeak analysis of experimental data reported here, the true background has been assumed to be one-half the sum of the areas B and C with a probable error of one-half the difference of the areas B and C. That is, the true background is taken as the average of the areas B and C with a probable error of the difference between the average and either B or C. It may be noted that the semilogarithmic scale used in Figure 36 over-emphasizes the areas B and C relative to the total area or peak area. The peak area is found by subtracting the true background from the total area.

Figure 35

GOLD FOIL # 26
0848 15 Feb. 65

0.412 MeV

0.676 MeV

Random Sum

1.089 MeV

Counts per Channel

Channel Number

0.412 MeV Photopeak
Gold Foil No. 26
1314   11 Feb 65

Area B is upper limit
of background correction

Area C is lower limit
of background correction

background correction
used = $\frac{1}{2}$ (B+C)
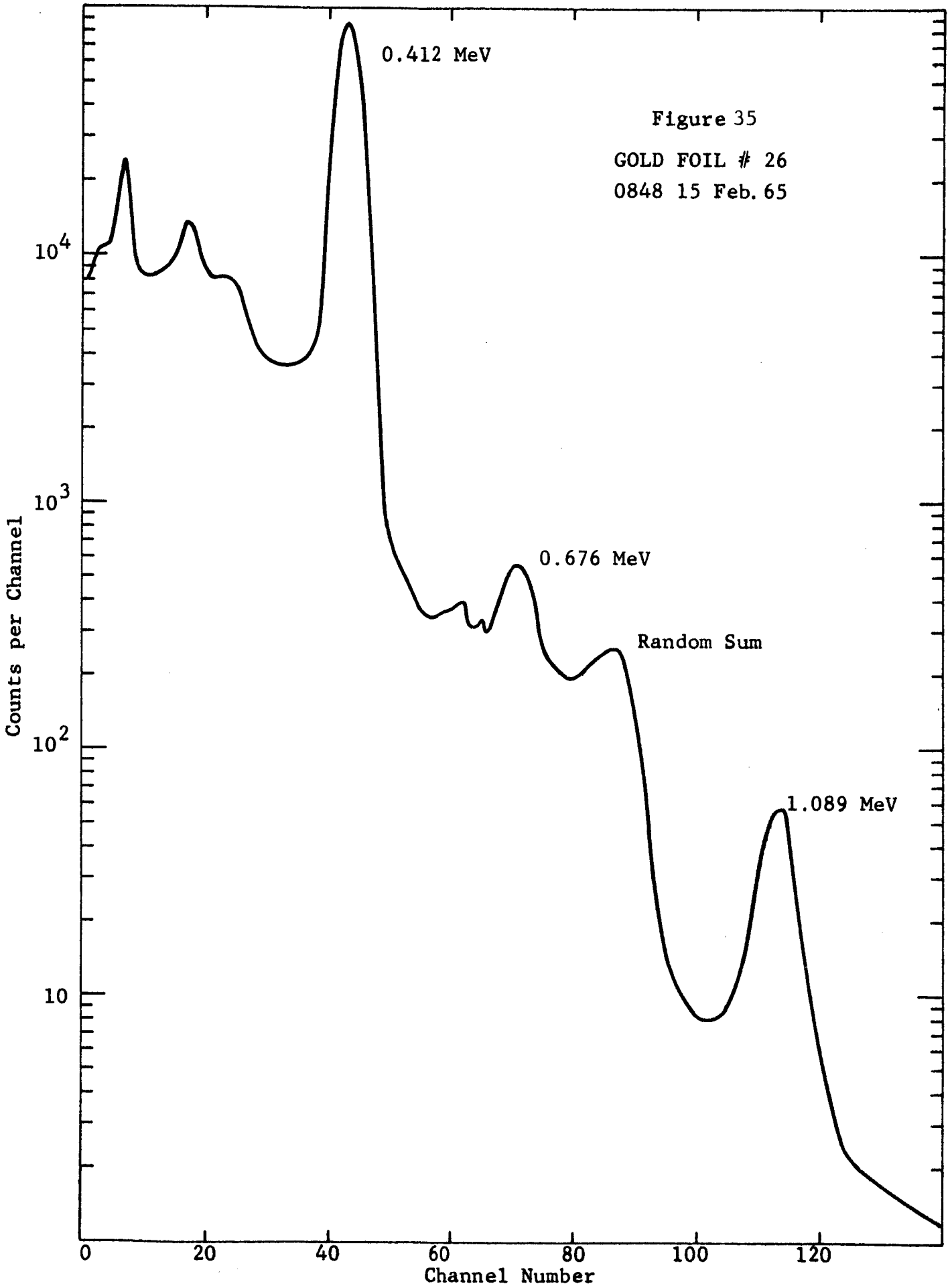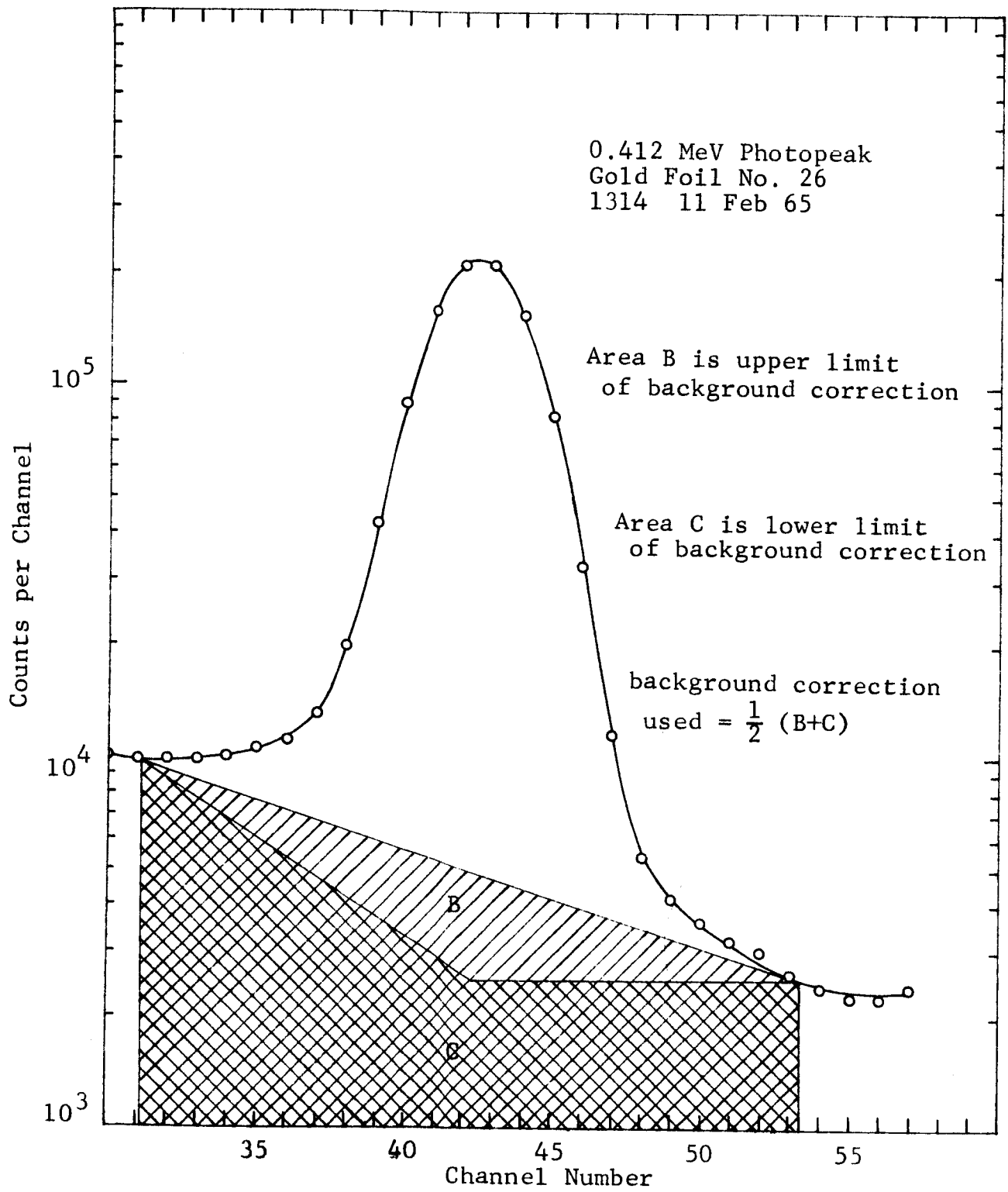
Figure 36

TYPICAL PHOTOPEAK

Having obtained the peak area, the computer program computes the gamma ray source strength at the beginning of the counting interval by

$$S = \frac{\lambda(t_L + t_D) A}{Kt_L[1-e^{-\lambda(t_L + t_D)}]} \qquad (109)$$

where

S	$=$	foil emission rate of photons of given energy
λ	$=$	decay constant of emitting radioisotope
t_L	$=$	live time during counting interval
t_D	$=$	dead time during counting interval
A	$=$	peak area
K	$=$	efficiency factor relating number of photons detected to number of photons emitted.

The counting efficiency factor K is defined as

$$K = T\ T_L\ T_C\ P\ f \qquad (110)$$

where

T	$=$	total absolute detection efficiency
T_L	$=$	beta absorber transmission factor
T_C	$=$	detector cap transmission factor
P	$=$	peak-to-total ratio
f	$=$	foil transmission factor

Detection efficiencies have been calculated by Heath (ref. 36) as a function of gamma ray energy, detector size, and foil-detector separation for point and disk sources. The transmission factor for the Lucite beta particle absorber was calculated using total gamma ray absorption cross sections for elements present in Lucite. Since such cross sections

found in the literature are generally appropriate only for a highly collimated geometry, calculated and measured transmission factors are not in exact agreement, particularly at low gamma ray energies. To account for this effect, the calculated Lucite transmission factors were corrected by the ratio of observed to calculated beryllium transmission factors as reported by Heath. The results are shown in Figure 37 which gives Lucite transmission factors as a function of gamma energy. The detector cap transmission factors were calculated in a similar manner, but because the values obtained were nearly unity no further correction was made. The peak-to-total ratio, or that fraction of the total number of events in the pulse height spectrum which appear in the photopeak, has been determined experimentaly as a function of gamma ray energy by Heath. Finally, the fraction of gamma rays of a selected energy which succeed in escaping from the foil is given by

$$f = \frac{1}{2\mu t} \left[1 - 2E_3(\mu t) \right] \tag{111}$$

where t is the foil thickness and μ is the gamma absorption coefficient of the foil material for gammas of the selected energy. A more complicated appearing equation has been reported by Lewis (ref. 37), but the equation above is mathematically equivalent. It may be noted that the equation above has the same form as equation (108) for the neutron self-shielding factor. This is a consequence of the neutron transport reciprocity theorem. The efficiencies and transmission factors entering into the computation of the counter efficiency K are given in Table 12.

Measured data obtained for each foil is given in Tables 13 through 19. In each case, the background, peak area, and source strength obtained as described above is shown together with the associated standard error or deviation. As stated

104
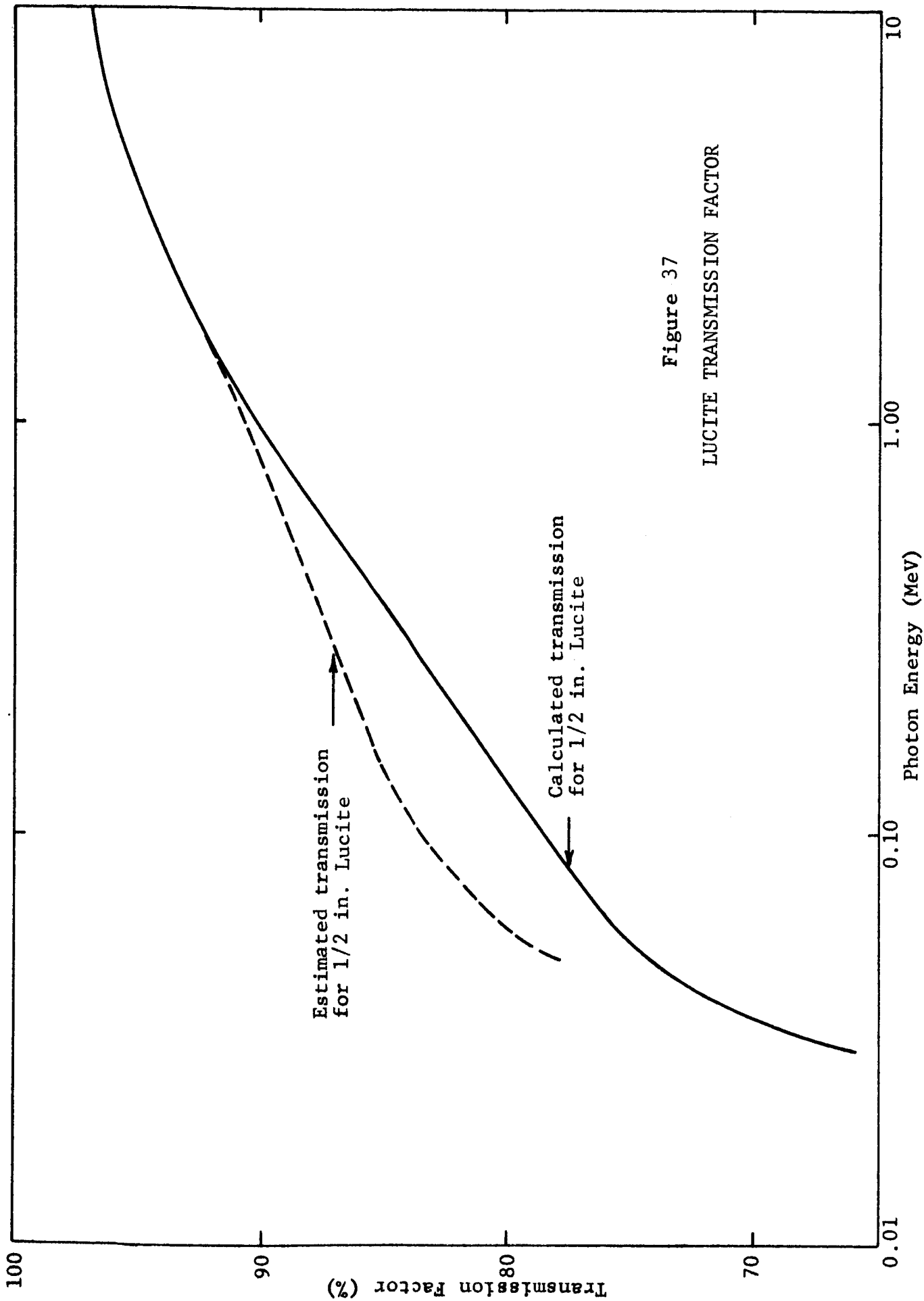
Figure 37

LUCITE TRANSMISSION FACTOR

Estimated transmission for 1/2 in. Lucite

Calculated transmission for 1/2 in. Lucite

Photon Energy (MeV)

Transmission Factor (%)

105

Table 12

EFFICIENCIES AND TRANSMISSION FACTORS

Foil	Detection Efficiency	Transmission Factors			Peak-to- Total Ratio	Counting Efficiency
		Lucite	Cap	Foil		
Au #25	0.0234(3)	0.880(4.5)	0.978(1.5)	0.947(2)	0.737(2)	0.0141(6.3)
Au #26	0.0234(3)	0.880(4.5)	0.978(1.5)	0.938(2.1)	0.737(2)	0.0139(6.3)
Au #27	0.0234(3)	0.880(4.5)	0.978(1.5)	0.937(2.2)	0.737(2)	0.0139(6.3)
Au #28	0.0234(3)	0.880(4.5)	0.978(1.5)	0.949(2)	0.737(2)	0.0141(6.3)
In #13	0.0147(6)	0.932(3)	0.990(1.5)	0.972(1.8)	0.266(2)	0.00351(7.4)
In #14	0.0147(6)	0.932(3)	0.990(1.5)	0.972(1.8)	0.266(2)	0.00351(7.4)
Ni #1	0.0193(5)	0.887(4.4)	0.981(1.5)	0.934(2.2)	0.482(2)	0.00756(7.5)

NOTE: Values enclosed by parentheses indicate assumed standard error in percent.

106

Table 13

MEASURED ACTIVITY-GOLD FOIL NO. 25

Time After Irradiation (hours)	Peak Area (10^3 γ/min)	Background (10^3 γ/min)	Source Strength (0.412 MeV) (10^3 γ/sec)
5.76	744 $\pm$ 51	63 $\pm$ 51	879 $\pm$ 81
6.59	738 $\pm$ 51	59 $\pm$ 51	872 $\pm$ 80
23.39	613 $\pm$ 44	48 $\pm$ 44	725 $\pm$ 68
120.79	227 $\pm$ 16	16 $\pm$ 16	268 $\pm$ 25
143.94	180 $\pm$ 12	11 $\pm$ 11	212 $\pm$ 19
192.32	108 $\pm$ 7	7 $\pm$ 7	127 $\pm$ 12
311.41	30 $\pm$ 2	2 $\pm$ 2	35.7 $\pm$ 3.1
364.51	16.9 $\pm$ 1.2	1.2 $\pm$ 1.2	20.0 $\pm$ 1.8

Table 14

MEASURED ACTIVITY-GOLD FOIL NO. 26

Time After Irradiation (hours)	Peak Area (10^3 γ/min)	Background (10^3 γ/min)	Source Strength (0.412 MeV) (10^3 γ/sec)
1.05	1008 $\pm$ 75	86 $\pm$ 75	1210 $\pm$ 116
3.32	1011 $\pm$ 57	97 $\pm$ 57	1212 $\pm$ 100
6.62	972 $\pm$ 71	81 $\pm$ 71	1166 $\pm$ 111
23.47	793 $\pm$ 54	65 $\pm$ 54	951 $\pm$ 87
30.70	747 $\pm$ 46	64 $\pm$ 46	896 $\pm$ 78
94.88	390 $\pm$ 29	29 $\pm$ 29	468 $\pm$ 45
120.83	300 $\pm$ 22	24 $\pm$ 22	359 $\pm$ 34
143.75	340 $\pm$ 17	17 $\pm$ 17	288 $\pm$ 27
311.82	40.4 $\pm$ 2.9	2.7 $\pm$ 2.7	48.5 $\pm$ 4.5
360.50	23.4 $\pm$ 1.0	1.0 $\pm$ 1.0	28.1 $\pm$ 2.1

Table 15

MEASURED ACTIVITY-GOLD FOIL NO. 27

Time After Irradiation (hours)	Peak Area (10^3 γ/min)	Background (10^3 γ/min)	Source Strength (0.412 MeV) (10^3 γ/sec)
0.77	258 ± 18	19 ± 18	309 ± 28
3.17	256 ± 17	17 ± 17	307 ± 27
6.64	243 ± 17	17 ± 17	291 ± 27
23.26	202 ± 14	14 ± 14	242 ± 22
30.80	191 ± 11	11 ± 11	229 ± 19
94.72	96 ± 6	7 ± 6	115 ± 11
120.55	73 ± 5	5 ± 5	88 ± 8
143.79	57 ± 3	3 ± 3	68 ± 8
311.80	9.1 ± 0.3	0.4 ± 0.3	10.9 ± 0.8
352.69	5.3 ± 0.2	0.3 ± 0.2	6.4 ± 0.5

Table 16

MEASURED ACTIVITY-GOLD FOIL NO. 28

Time After Irradiation (hours)	Peak Area (10^3 γ/min)	Background (10^3 γ/min)	Source Strength (0.412 MeV) (10^3 γ/sec)
5.92	2330 $\pm$ 72	480 $\pm$ 72	2756 $\pm$ 188
6.72	2331 $\pm$ 73	489 $\pm$ 73	2756 $\pm$ 188
23.53	2024 $\pm$ 70	356 $\pm$ 70	2394 $\pm$ 167
120.93	896 $\pm$ 45	81 $\pm$ 45	1059 $\pm$ 83
143.85	725 $\pm$ 35	59 $\pm$ 35	857 $\pm$ 66
169.43	568 $\pm$ 28	41 $\pm$ 28	672 $\pm$ 52
191.47	465 $\pm$ 23	30 $\pm$ 23	550 $\pm$ 43
311.60	132 $\pm$ 7	7.0 $\pm$ 6.4	156 $\pm$ 12
360.72	77.6 $\pm$ 4.0	4.3 $\pm$ 4.0	91.8 $\pm$ 7.3
364.50	74.5 $\pm$ 3.8	4.1 $\pm$ 3.7	88.1 $\pm$ 6.8

Table 17

MEASURED ACTIVITY-INDIUM FOIL NO. 13

Time After Irradiation (hours)	Peak Area (10^3 γ/min)	Background (10^3 γ/min)	Source Strength (2.09 MeV) (10^3 γ/sec)
3.49	66 $\pm$ 21	290 $\pm$ 21	366 $\pm$ 122
3.99	68 $\pm$ 14	178 $\pm$ 14	365 $\pm$ 80
4.39	70 $\pm$ 17	114 $\pm$ 17	364 $\pm$ 94
4.92	59 $\pm$ 14	60 $\pm$ 14	297 $\pm$ 71
5.14	50 $\pm$ 8	42 $\pm$ 8	250 $\pm$ 44
5.86	31.4 $\pm$ 3.1	15.6 $\pm$ 3.1	154 $\pm$ 19
6.01	30.0 $\pm$ 2.8	13.0 $\pm$ 2.8	147 $\pm$ 18
6.66	19.8 $\pm$ 0.5	5.2 $\pm$ 0.5	95.7 $\pm$ 7.4
6.79	16.7 $\pm$ 1.3	4.8 $\pm$ 1.2	80.6 $\pm$ 8.5

Table 18

MEASURED ACTIVITY-INDIUM FOIL NO. 14

Time After Irradiation (hours)	Peak Area $(10^3 \, \gamma/\text{min})$	Background $(10^3 \, \gamma/\text{min})$	Source Strength (2.09 MeV) $(10^3 \, \gamma/\text{sec})$
3.00	52 $\pm$ 11	47 $\pm$ 11	261 $\pm$ 59
4.58	18.1 $\pm$ 1.7	5.5 $\pm$ 1.7	87.7 $\pm$ 10.4
4.72	17.0 $\pm$ 1.6	5.0 $\pm$ 1.6	82.3 $\pm$ 9.8
5.25	11.1 $\pm$ 0.8	2.3 $\pm$ 0.8	53.4 $\pm$ 5.5
5.43	10.0 $\pm$ 0.8	2.1 $\pm$ 0.7	48.0 $\pm$ 5.1
6.10	6.06 $\pm$ 0.41	0.99 $\pm$ 0.30	29.0 $\pm$ 2.9

Table 19

MEASURED ACTIVITY-NICKEL FOIL NO. 1

Time After Irradiation (hours)	Peak Area (10^3 γ/min)	Background (10^3 γ/min)	Source Strength (0.805 MeV) (10^3 γ/sec)
24.08	47.5 $\pm$ 1.6	7.4 $\pm$ 1.6	2.62 $\pm$ 0.21
95.90	46.6 $\pm$ 1.9	3.0 $\pm$ 1.8	2.57 $\pm$ 0.22
118.20	46.0 $\pm$ 1.3	2.8 $\pm$ 1.3	2.54 $\pm$ 0.20
143.75	45.6 $\pm$ 1.5	2.8 $\pm$ 1.5	2.52 $\pm$ 0.21

previously, the probable error in the background is taken as
the difference between the average of the areas B and C and
either the area B or C. The standard error is assumed to be
1.6449 times the probable error. The error in the peak area
is obtained from the error in the background and the random
statistical errors in counting. Since the peak area is
obtained by subtracting the background area from the total
area, the random statistical error in the peak area is simply
the square root of the sum of the total area and the background.
The non-random error in the background has been treated as
an additional statistical error. That is, the standard error
in the peak area is taken as

$$\sigma(A) = \sqrt{(A + B') + B' + \sigma^2(B')}$$
(112)

where B' is the assumed true background, i.e. 0.5(B+C), A is
the peak area, and $\sigma(B')$ is 1.6449 times the probable error
in B'. In almost every case, the error in the background
entirely dominates the random statistical errors, and thus
the error in the peak area is essentially the non-random
error in the background.

The standard error in the counting efficiency K is
obtained from

$$\frac{\sigma^2(K)}{K^2} = \frac{\sigma^2(T)}{T^2} + \frac{\sigma^2(T_L)}{T_L^2} + \frac{\sigma^2(T_C)}{T_C^2} + \frac{\sigma^2(P)}{P^2} + \frac{\sigma^2(f)}{f^2}$$
(113)

where $\sigma(K)$ is the standard error in K, etc. The "error" in
the detection efficiency T has been given by Heath as a
function of gamma ray energy and the uncertainty in the NaI
absorption coefficient. Heath notes that a ten percent
uncertainty in the absorption coefficient is "considerably
larger" than can be expected reasonably. The error in K has

114

been obtained here by assuming an eight percent uncertainty
in the absorption coefficient and interpreting the "error"
given by Heath as a standard deviation or standard error.
Similarly, the peak-to-total ratios as given by Heath are
stated to be good to within two percent. This value has also
been interpreted as a standard error. Probable errors for the
other factors entering into the counting efficiency have been
estimated and multiplied by the factor 1.6449 to yield a standard
deviation. Fractional standard errors for all these factors
have been shown by the parenthesized values in Table 12.

Finally, the standard error in the source strength has
been obtained from

$$\frac{\sigma^2(S)}{S^2} = \frac{\sigma^2(K)}{K^2} + \frac{\sigma^2(A)}{A^2} \tag{114}$$

This standard error is given in Tables 13 through 19, as are
the standard errors in the background and peak area. No error
has been assigned to the determination of dead time during the
counting interval or uncertainty in the known half-life. Both
these quantities are well known and enter the analysis only in
correcting the activity to account for decay during the counting
interval.

c.) Neutron Flux Determination

The neutron flux at port "O", which was required for
the NAP calculations discussed above, was determined by both
measurements and calculation. Through past project experience,
the Health Physics Section at IITRI has developed a convenient
and reasonably accurate foil activation method for determination
of reactor neutron fluxes. This method was used to assist in
determination of the neutron flux at port "O". The flux spectrum,
but not the absolute magnitude, was also determined by a multi-
group diffusion theory calculation.

115

The IITRI Health Physics Section was given sole responsibility for measurement of the neutron flux as a function of energy in port "O" of the IITRI Research Reactor. The foil activation technique measures the integral of the flux per unit energy above a threshold energy which is dependent upon the detector reaction. The detector reactions, threshold energies, and resultant integral fluxes are shown in Table 20. In addition to the flux measurements given in Table 20, the thermal flux (i.e. the integral of the flux per unit energy below 0.4 eV) was measured in two seaprate trials as 7.69×10^{11} and 7.45×10^{11} neutrons/cm^2-sec. The total integrated flux implied by the measurements is 1.76×10^{12} neutrons/cm^2-sec.

To provide more detailed information on the energy dependence of $\emptyset(E)$, the flux per unit energy, a multigroup diffusion theory calculation was performed using the CRAM computer code (ref. 38). This calculation was done in spherical geometry using 23 neutron energy groups. By normalizing the total integrated flux to 1.76×10^{12} neutrons/cm^2-sec at the radial position of port "O", the neutron energy spectrum may be obtained from the CRAM results. The resultant flux spectrum is given in Table 21. In obtaining input for the CRAM calculation, the epithermal group constants were generated by use of the GAM computer code (ref. 39), the thermal group constants by use of the TEMPEST computer code (ref. 40). The normalized integral flux as obtained from the CRAM calculation is in good agreement with the measured values, as shown in Figure 38. It is seen that the CRAM calculation is necessary to provide adequate detail in the flux spectrum between ten eV and one MeV. The error bars associated with the measured values shown in the figure indicate reliability, and do not account for any systematic errors.

The neutron flux spectrum used in the NAP calculations reported in Section II-C-1-a was obtained from the data in Table 21. These data are regarded as accurate to $\pm$ 10 percent. The neutron energy group structure used in the ten-group NAP

Table 20

EXPERIMENTAL FLUX DETERMINATION

Reaction	Threshold Energy		Integral Flux Above Threshold $(10^{10} n/cm \ sec)$	
			First Trial	Second Trial
$Zr^{90}(n,2n)$	13.3	MeV	0.00122	————
$I^{127}(n,2n)$	9.90	MeV	0.0365	0.0354
$Al^{27}(n,\alpha)$	6.61	MeV	0.166	0.178
$Mg^{24}(n,p)$	6.55	MeV	0.151	0.152
$Si^{28}(n,p)$	5.43	MeV	0.215	0.198
$Fe^{56}(n,p)$	5.30	MeV	3.43	3.51
$Al^{27}(n,p)$	3.48	MeV	4.08	4.20
$S^{32}(n,p)$	2.28	MeV	3.46	3.47
$Ni^{58}(n,p)$	2.01	MeV	4.03	3.81
$Fe^{54}(n,p)$	1.59	MeV	5.10	4.66
$U^{238}(n,f)$	1.52	MeV	9.01	11.04
$Th(n,f)$	1.51	MeV	10.7	————
$In^{115}(n,n')$	1.14	MeV	9.67	9.17
$Ba^{137}(n,n')$	0.902	MeV	15.4	14.8
$U^{238}(n,\gamma)$	6.30	eV	32.3	————
$Au^{197}(n,\gamma)$	4.12	eV	77.6	81.1
$Th^{232}(n,\gamma)$	1.60	eV	153	113
$Co^{59}(n,\gamma)$	0.70	eV	96.1	————
$Na^{23}(n,\gamma)$	0.50	eV	119	————

Table 21

23-GROUP NEUTRON FLUX AT PORT "O" (65 kW)

Group Number	Group Lower Energy	Neutron Flux $= \int_{E_{2j-1}}^{E_j} \phi(E)\,dE$ (neutrons/cm^2 sec)
0	10 MeV	————
1	7.788	7.22×10^8
2	6.065	2.76×10^9
3	4.724	6.80×10^9
4	3.679	9.14×10^9
5	2.865	1.24×10^{10}
6	2.231	2.33×10^{10}
7	1.738	2.82×10^{10}
8	1.353	3.08×10^{10}
9	1.054	2.89×10^{10}
10	820.8 keV	2.75×10^{10}
11	639.3	2.73×10^{10}
12	497.9	2.60×10^{10}
13	387.7	2.45×10^{10}
14	302.0	2.33×10^{10}
15	235.2	2.22×10^{10}
16	183.2	2.12×10^{10}
17	24.79	1.38×10^{11}
18	1.234	1.70×10^{11}
19	167.0 eV	1.02×10^{11}
20	22.60	9.51×10^{10}
21	3.928	7.86×10^{10}
22	0.5316	8.44×10^{10}
23	0.001	7.76×10^{11}

Figure 38
Port "O"

INTEGRAL FLUX SPECTRUM
65 kw

119
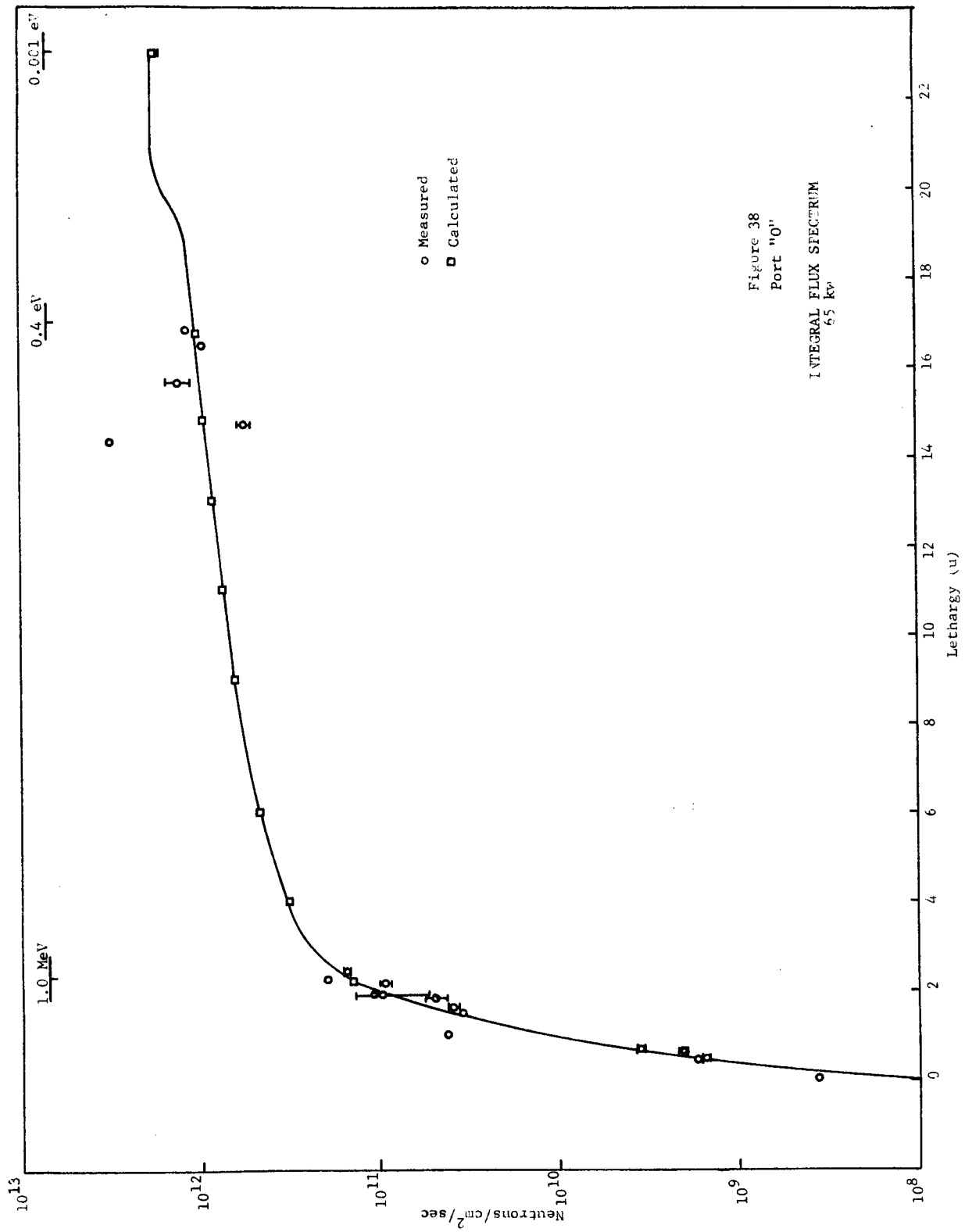
calculations, groups 11 and 12 in Table 21 were combined into
a single group, as were groups 13 and 14, and groups 15 and 16.
The addition of an energy group from 10 to 21 MeV results in
a 21-group neutron energy structure.

It may be noted that because fission products are
periodically removed from the reactor fuel solution, the
neutron flux values reported here should remain constant
(at a power level of 65 kW) over an extended period of time.

2. Van de Graaff Irradiations

The NAP computer program has been used to compute neutron
activation data for foils of iron, nickel, magnesium, zinc,
and zirconium and a silicon pill. These NAP calculation results
were then compared to measured activation data obtained by
irradiating these materials in the IITRI Van de Graaff facility.
These Van de Graaff irradiations supplement the reactor ir-
radiations discussed above by dealing with neutrons of an
entirely different energy range. The NAP calculations and
their comparison to the experimental data are presented and
discussed in Section a below, the experimental details and
data in Section b, and the determination of the incident
neutron flux in Section c.

a.) NAP Calculations and Comparison to Experiment

Four separate Van de Graaff irradiations were performed,
measured data obtained, and the experimental results compared
to appropriate NAP calculations. The first experiment was a
ten-minute irradiation of a small silicon pill, the second a
60-minute irradiation of an iron foil, the third a 61-minute
irradiation of a nickel foil, zirconium foil, magnesium foil,
and a zinc foil, and the the fourth a 30-minute irradiation
of the magnesium foil and zinc foil used in the third
experiment. The materials irradiated were all of high purity

(99 + %) elemental composition. The physical properties of the irradiated samples are summarized in Table 22. The silicon pill was cylindrical in shape with height 0.225 cm and diameter 0.30 cm. The respective aluminum samples were used as flux monitors during the four irradiations and were continuous lengths of twenty-mil wire, which had been coiled to approximate a thin, flat disc.

In all four experiments, the neutron source was provided by bombardment of a tritium target with a 600 keV deuteron beam. The beam current varied significantly from one experiment to the next, but throughout each individual irradiation the beam current was relatively constant. The samples to be irradiated were placed behind the tritium target, on the back of the target holder along the axis of the deuteron beam. There was 0.875 inch of water and 0.250 inch of stainless steel between the neutron source and the samples. An approximate calculation, discussed in Section c below, indicated that about half the neutrons resulting from the $T(d,n)He^4$ reaction were degraded in energy by scattering in the water coolant and steel target holder before reaching the foils. A kinematical calculation shows that 600 keV deuterons impinging upon an infinitely thin tritium target will produce neutrons of 14.1 MeV, corresponding to the peak of the $T(d,n)He^4$ cross section. In the NAP calculations, the neutron energy group structure was such that all neutrons reaching the foils directly from the tritium targer were treated in a single neutron energy group from 12.84 MeV to 16.49 MeV. The NAP neutron energy group structure was chosen to be consistent with the NAP Cross Section Library neutron energy group structure. This energy structure and the neutron energy spectrum used in the NAP calculations is shown in Table 23. The flux spectrum given there is normalized to a total (integrated over energy) flux of unity.

121

Table 22

VAN DE GRAAFF IRRADIATION SAMPLES

Sample	Mass (mg)	Area (cm^2)	Thickness (mils)
Silicon	40.8	—	—
Iron	303.7	1.00	15
Nickel #2	457.8	1.00	21
Zirconium	320.6	1.00	20
Magnesium	22.1	1.00	5.5
Zinc	339.4	1.00	20
Al wire #1	136.4	1.13	20
Al wire #2	136.4	1.23	20
Al wire #3	103.4	0.785	20
Al wire #4	136.7	1.33	20

Table 23

VAN DE GRAAFF NEUTRON FLUX SPECTRUM

Group No.	Lower Energy Limit (MeV) (E_j)	$\int_{E_j}^{E_{j-1}} \phi(E)dE$
0	21.17	————
1	16.49	0
2	12.84	0.4605
3	10.00	0.0061
4	7.788	0.0251
5	6.065	0.0411
6	4.724	0.0576
7	3.679	0.0675
8	2.865	0.0690
9	2.231	0.0632
10	1.738	0.0526
11	1.353	0.0411
12	1.054	0.0310
13	0.498	0.0473
14	0	0.0379

In the first Van de Graaff experiment, Al wire #1 was placed on the back of the target holder, along the axis of the deuteron beam. The silicon pill was placed immediately behind the coil of aluminum wire. The beam current was turned on at 1815 hours, 19 August 1965, was maintained at constant current, and turned off at 1825 hours. The aluminum wire and silicon pill were then removed from the back of the target holder, and gamma-counted using the detection system described in Section b below.

NAP calculations were performed for the aluminum wire using the 14-group neutron energy spectrum given in Table 23. The gamma ray energy group structure was chosen to isolate the Mg^{27} 0.842 MeV and 1.01 MeV photopeaks and the Na^{24} 1.368 MeV photopeak. The NAP Cross Section Library was used in this calculation, and in all other NAP calculations unless specifically stated otherwise. A comparison of the measured gamma activity with the NAP calculation implied that the total neutron flux incident upon the aluminum wire was 3.55 ± 0.47 x 10^8 neutrons/cm^2-sec. The quoted standard error in this value is based upon the standard errors, or deviations, in the gamma-counting together with an assumed ten percent standard deviation in the aluminum (n,p) and (n,α) cross sections.

A NAP calculation was performed for the silicon pill using the 14-group neutron energy spectrum and the total flux value given above. The silicon pill was represented by a slab region of thickness 0.225 cm and volume 0.0159 cm^3. The total number of silicon atoms present in the region was based on the measured mass and known atomic weight. Thus the calculated regional activation source strength (but not the source strength density) is independent of the regional dimensions, as long as neutron self-shielding effects can be ignored. Because of the small size of the irradiated samples relative to the neutron mean free path, the NAP neutron self-shielding option was not

124

used in any of these calculations of induced activity. The
NAP gamma ray energy group structure in the silicon calcula-
tion was chosen to isolate the Al^{28} 1.80 MeV gamma ray activity.
The results of the NAP calculation are compared to experiment
in Figure 39. The error bars associated with the measured
data represent the nine-tenths error. Since the incident total
flux is known only to $\pm$ 13 percent, the absolute flux spectrum
used in the NAP silicon calculation is accurate to roughly 25
percent. The calculated activity of the silicon pill is then
accurate to about 25 percent, if one ignores all errors per-
taining to silicon cross sections, decay branching ratios,
fractional gamma ray emission probabilities, etc. With this
in mind, the calculated activity of the silicon pill shows
excellent agreement with the measured data.

In the second Van de Graaff experiment, the iron foil
and Al wire #2 were irradiated. The deuteron beam current
was turned on at 1932 hours 19 August 1965, maintained at a
constant value, and turned off at 2032 hours. As with the
previous experiment, a comparison with the experimental data
of NAP calculations of the Mg^{27} 0.842 MeV and 1.01 MeV activ-
ities induced in the aluminum wire indicated a total flux
during the irradiation of 7.8 $\pm$ 1.6 x 10^7 neutrons/cm^2-sec.
In this experiment there was insufficient activity to permit
accurate counting of the 1.368 MeV photopeak. Using this total
flux value and a 14-group neutron energy group structure, a
NAP calculation of the induced activity in the iron foil was
made. The gamma energy group structure was chosen to isolate
the Mn^{56} 0.84 MeV and 1.81 MeV gamma activities. The results
of this calculation are compared with the measured data in
Figure 40. As with the silicon pill, excellent agreement
between the experiment and the NAP calculation is achieved.

In the third Van de Graaff experiment, a nickel foil,
zirconium foil, magnesium foil, zinc foil, and Al wire #3
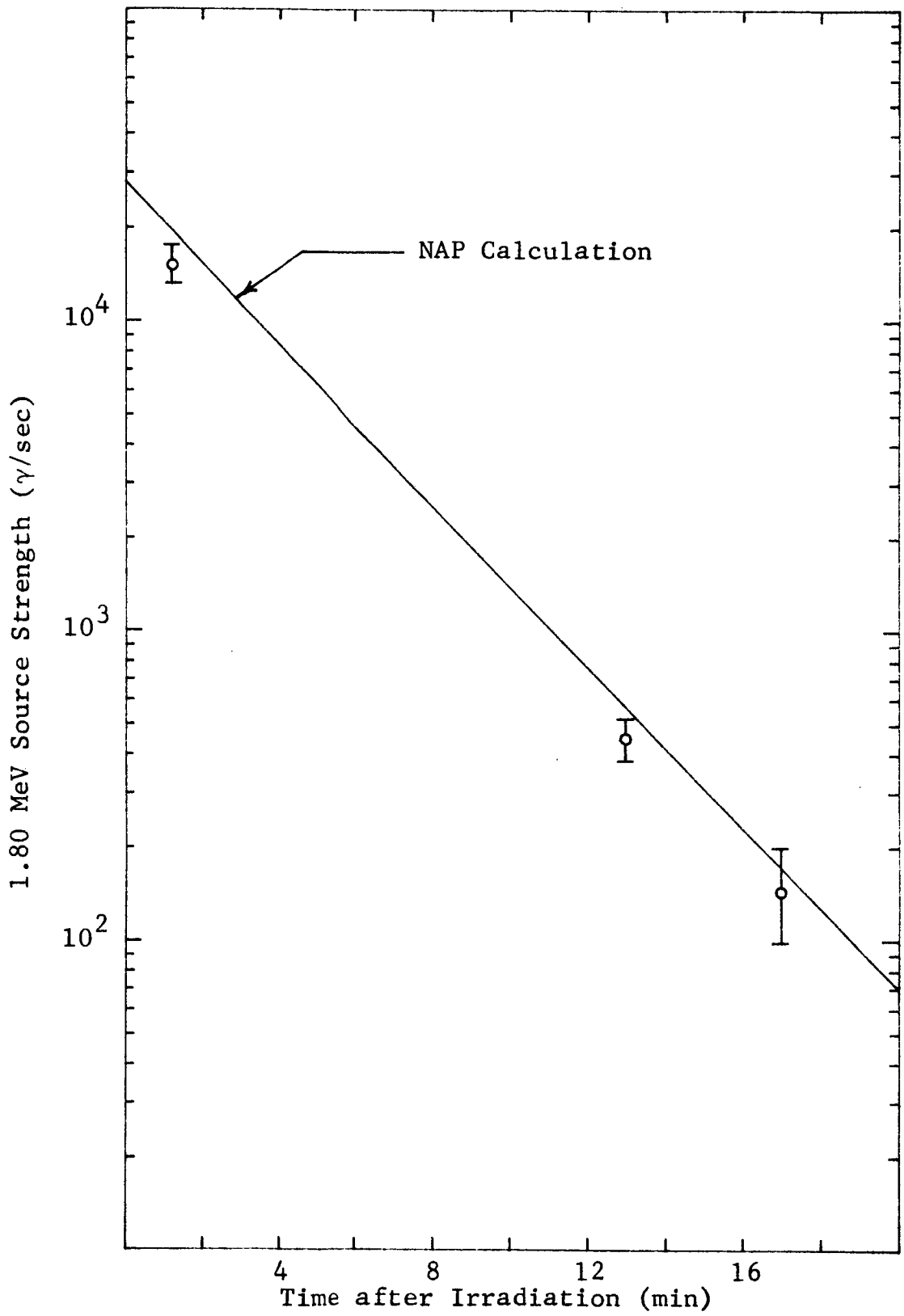were placed simultaneously on the target holder, along the
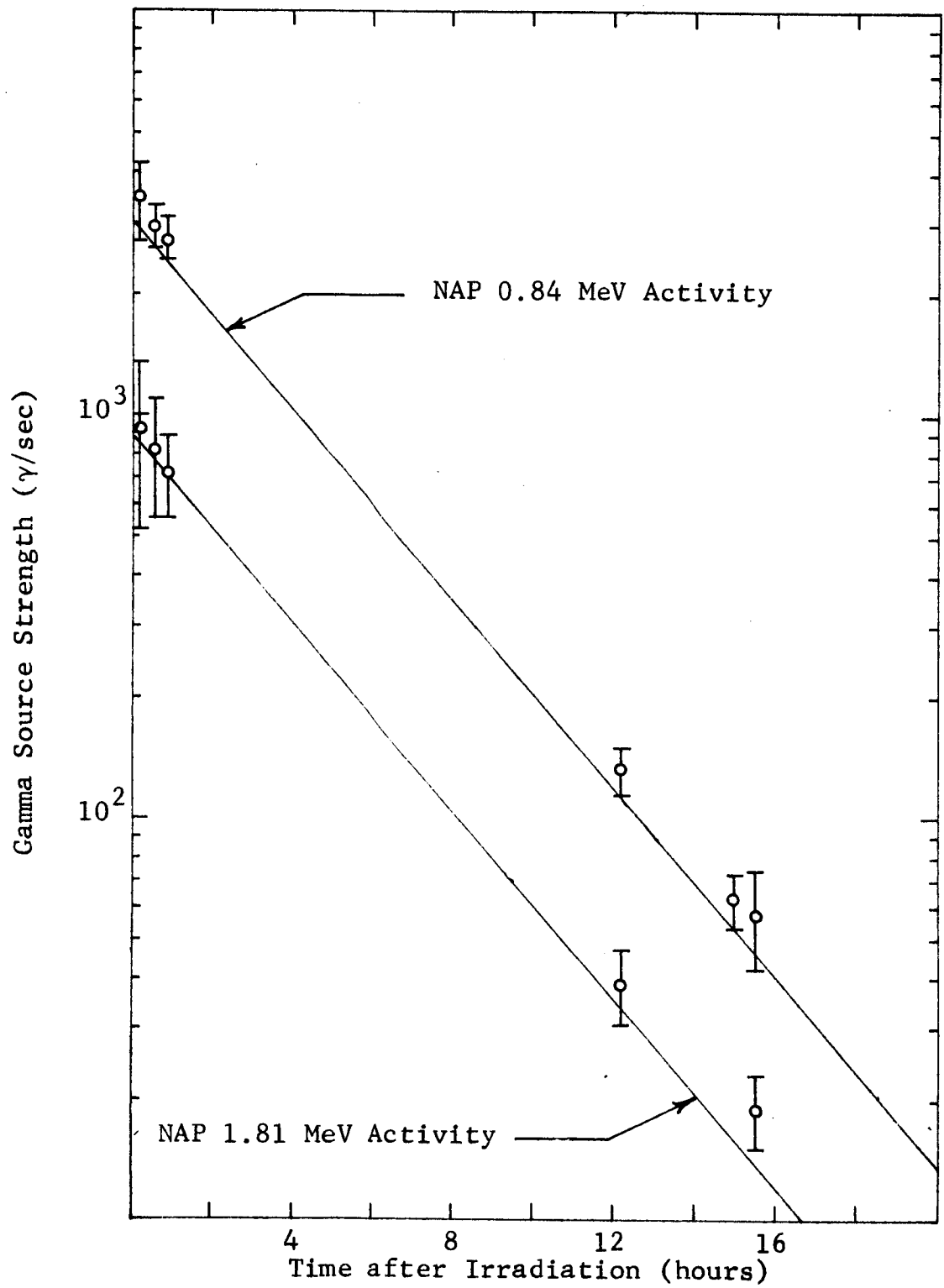
Figure 39

SILICON PILL

Figure 40

IRON FOIL

beam axis, in the order named from front to rear. The beam
current was turned on at 1808 hours 14 December 1965, main-
tained at constant current, and turned off at 1909 hours. A
total flux of 6.17 ± 0.78 x 10^7 was indicated by comparison
with experiment of NAP calculations of the 0.842 MeV, 1.01 MeV,
and 1.368 MeV activities in the aluminum wire. Using this
total flux value, a NAP calculation of the nickel and zircon-
ium foil irradiations was made. The results are compared to
experiment in Figures 41 and 42. The NAP gamma ray energy
group structure was selected to combine the 0.805 MeV and
0.808 MeV Co^{58} gamma ray activities in the nickel foil into
a single gamma ray energy group (since the two activities
cannot be resolved experimentally) and to isolate the 0.915
MeV Y^{89} gamma ray activity in the zirconium foil. The calcu-
lated Co^{58} activity is about thirty percent higher than the
measured activity, while the calculated Y^{89} activity is about
thirty percent lower than the measured activity. Although this
error is not much larger than the accuracy with which the
absolute flux spectrum is known, the error is of opposite
sign in the two cases and any consistent renormalization of
the incident flux would not improve the overall agreement.

Finally, in the last Van de Graaff experiment, data were
obtained and comparisons were made which validate the use of
the NAP computer code in the case of non-uniform cyclic irrad-
iations. Here the magnesium and zinc foils used in the third
Van de Graaff experiment were re-irradiated after a 69-minute
decay period. The previously irradiated magnesium and zinc
foils were placed on the target holder in the same position
as before, except that the nickel and zirconium foils were
absent. Al wire #4 was used as a flux monitor. The Van de
Graaff was switched on at 2018 hours, maintained at constant
beam current, and turned off at 2048 hours. Comparison of
a NAP calculation with the measured 0.842 MeV, 1.01 MeV, and
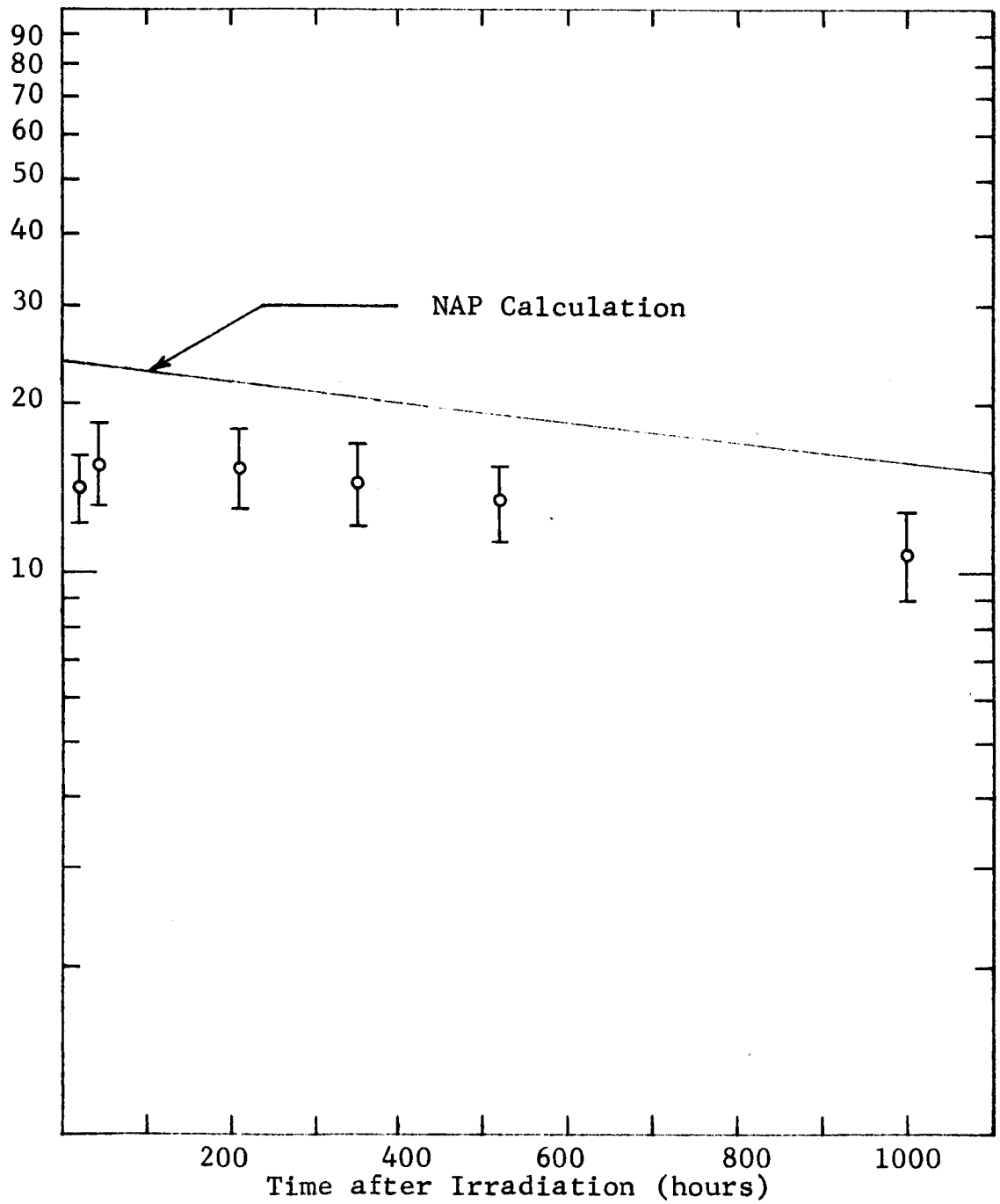1.368 MeV activities in the aluminum wire indicated a total
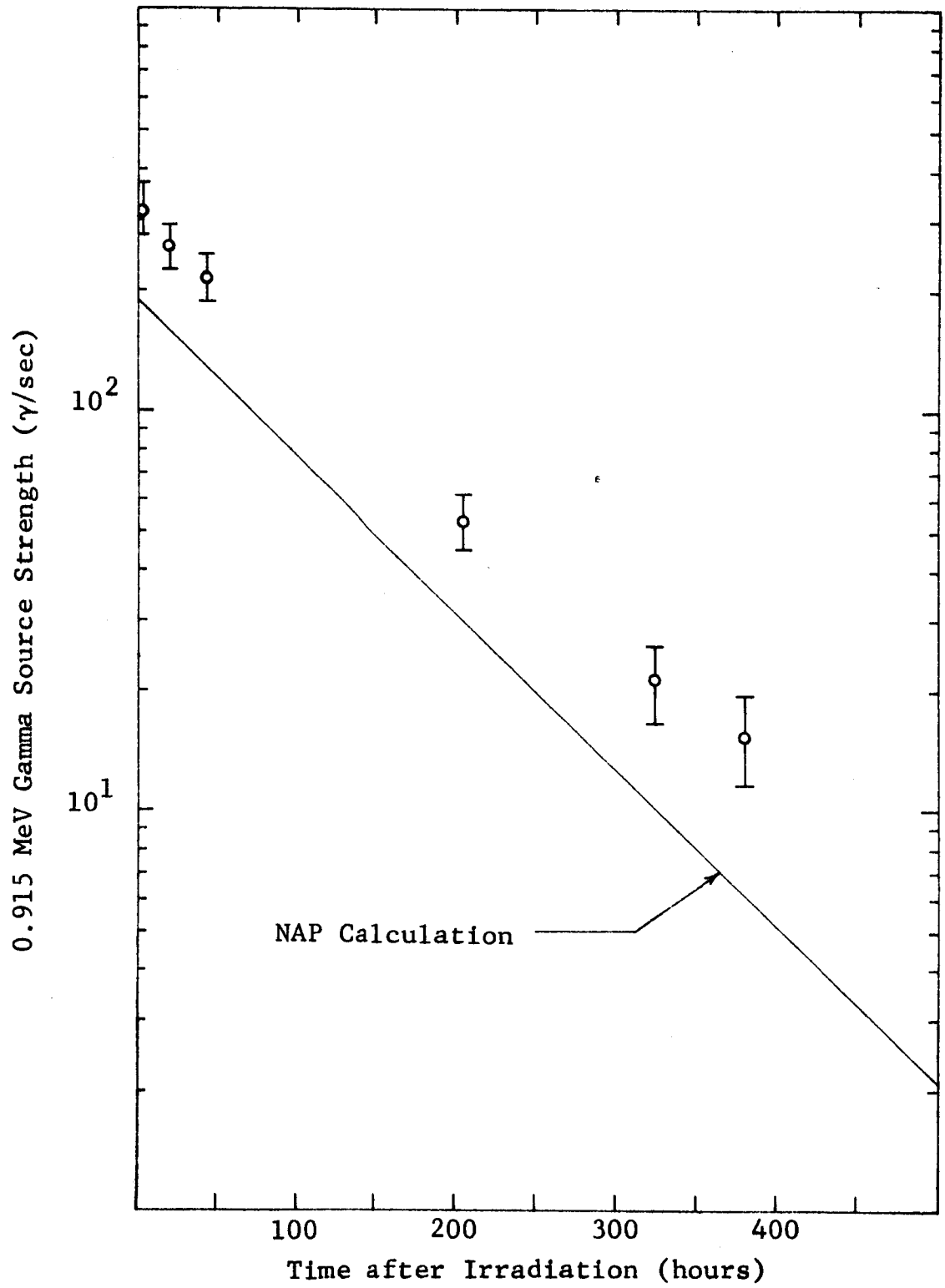
Figure 41

NICKEL FOIL

Figure 42

ZIRCONIUM FOIL

flux of $7.05 \pm 0.94 \times 10^7$ neutrons/cm^2-sec. Using this flux value for the second irradiation period and the previous flux value of 6.17×10^7 for the first irradiation period, a NAP calculation of the activity induced in the magnesium and zinc foils was performed. The gamma ray energy group structure was chosen to isolate the Na^{24} 1.368 MeV activity in the magnesium foil and the Zn^{63} 0.97 MeV activity in the zinc foil. The NAP results are compared to experiment in Figures 43 and 44. The calculated activity of the magnesium foil appears to be somewhat lower than the measured values, particularly two or three days after the irradiations. The shape of the measured decay, together with the shape of the measured gamma ray emission spectrum, suggests that there may be an activity contribution from a long-lived 1.47 MeV gamma emitter. No such contribution was calculated by the NAP code. The calculation 0.97 MeV activity of the zinc foil, however, shows excellent agreement with the experimental data.

It was mentioned above that there is some uncertainty in the energy of the neutrons reaching the sample directly from the tritium target without scattering in the intervening material. The energy of these "direct" neutrons could be as high as 16 MeV or as low as 14.1 MeV. For NAP calculations using the neutron energy group structure given in Table 23 above, the distinction is immaterial since both these energies fall within neutron energy group two. However, if the energy of this sharp peak in the incident neutron energy spectrum were known exactly, the accuracy of the NAP calculations could be improved by utilizing the NAP program option which permits the program user to substitute his own set of neutron reaction cross sections in preference to the standard NAP Cross Section Library. That is, instead of using the NAP group two cross sections, which represent an average cross section between 12.84 MeV and 16.49 MeV, a cross section set in which the group two cross sections correspond to the cross sections at the exact energy of the spectrum peak could be used.
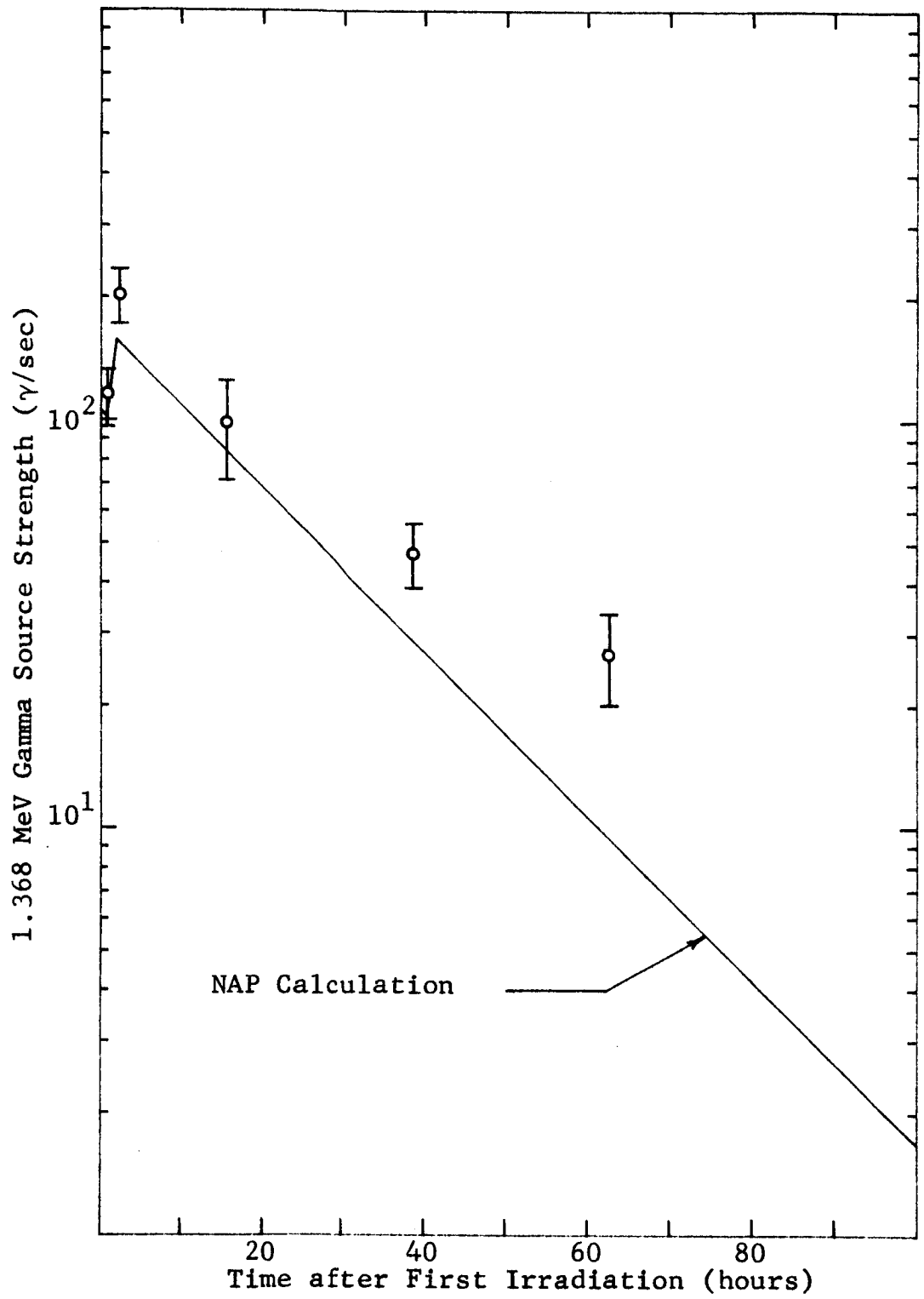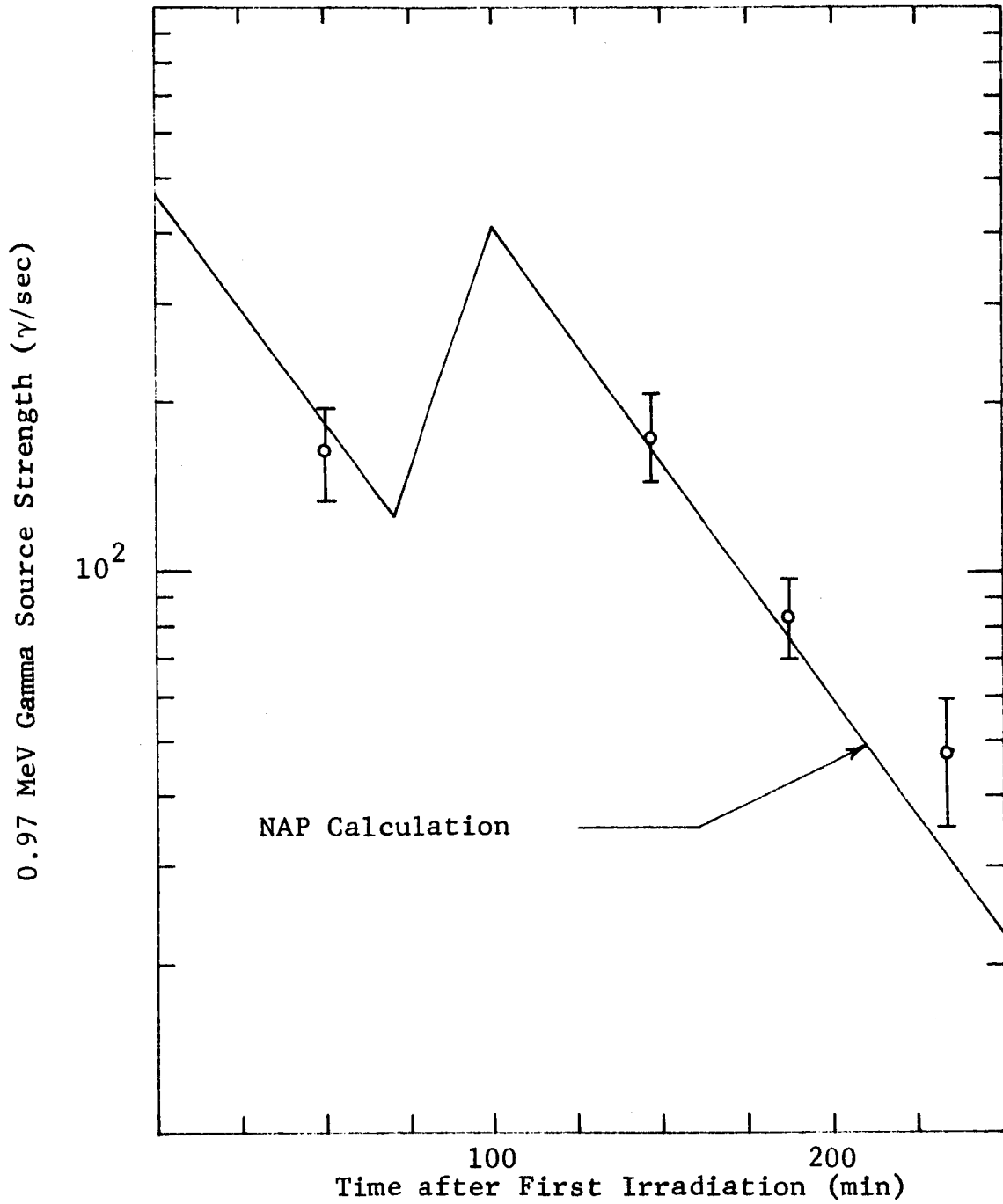
131

Figure 43

MAGNESIUM FOIL

Figure 44

ZINC FOIL

133

To indicate the sensitivity of the NAP calculations reported above to the cross sections used, and to demonstrate the flexibility of the NAP program, the NAP calculations discussed above were repeated using two different cross section sets. In the first set, the group two cross sections were appropriate to a neutron energy of 14.1 MeV. In the second set, the group two cross sections were appropriate to a neutron energy of 16.0 MeV. In both sets, the cross sections for energy groups other than group two were identical to the cross sections in the NAP Library. The results of NAP calculations using these two cross section sets are shown in Figure 45 through 50. In order to provide a consistent comparison to the measured data, it was necessary to renormalize the total flux by additional NAP calculations of the activity induced in the aluminum wires. The new total flux values are indicated on the figures. This procedure is exactly equivalent to assuming the peak in the neutron flux spectrum is at 14.1 MeV or 16.0 MeV.

Figures 45, 46, 47, and 49 show that the calculated activities of the silicon, iron, nickel, and magnesium samples are not very sensitive to the exact energy of the peak in the neutron flux spectrum, provided that the incident flux is re-normalized to reflect the energy shift of the spectrum peak. This is because the (n,p) cross sections for Si^{28}, Fe^{56}, Ni^{58}, and Mg^{24} have roughly the same neutron energy dependence as the Al^{27} (n,p) and Al^{27} (n,α) cross sections used to monitor the flux. This is not the case for the Zr^{90} (n,2n) and Zn^{64} (n,2n) cross sections. Consequently, Figures 48 and 50 show that the comparison of calculation to experiment for the zir- conium foil and the zinc foil is sensitive to the assumed energy of the spectrum peak. Note, however, that while assuming a peak energy of 16 MeV improves the comparison of calculation to experiment for the zirconium foil, it detracts from the comparison for the zinc foil. Similar comments are applicable
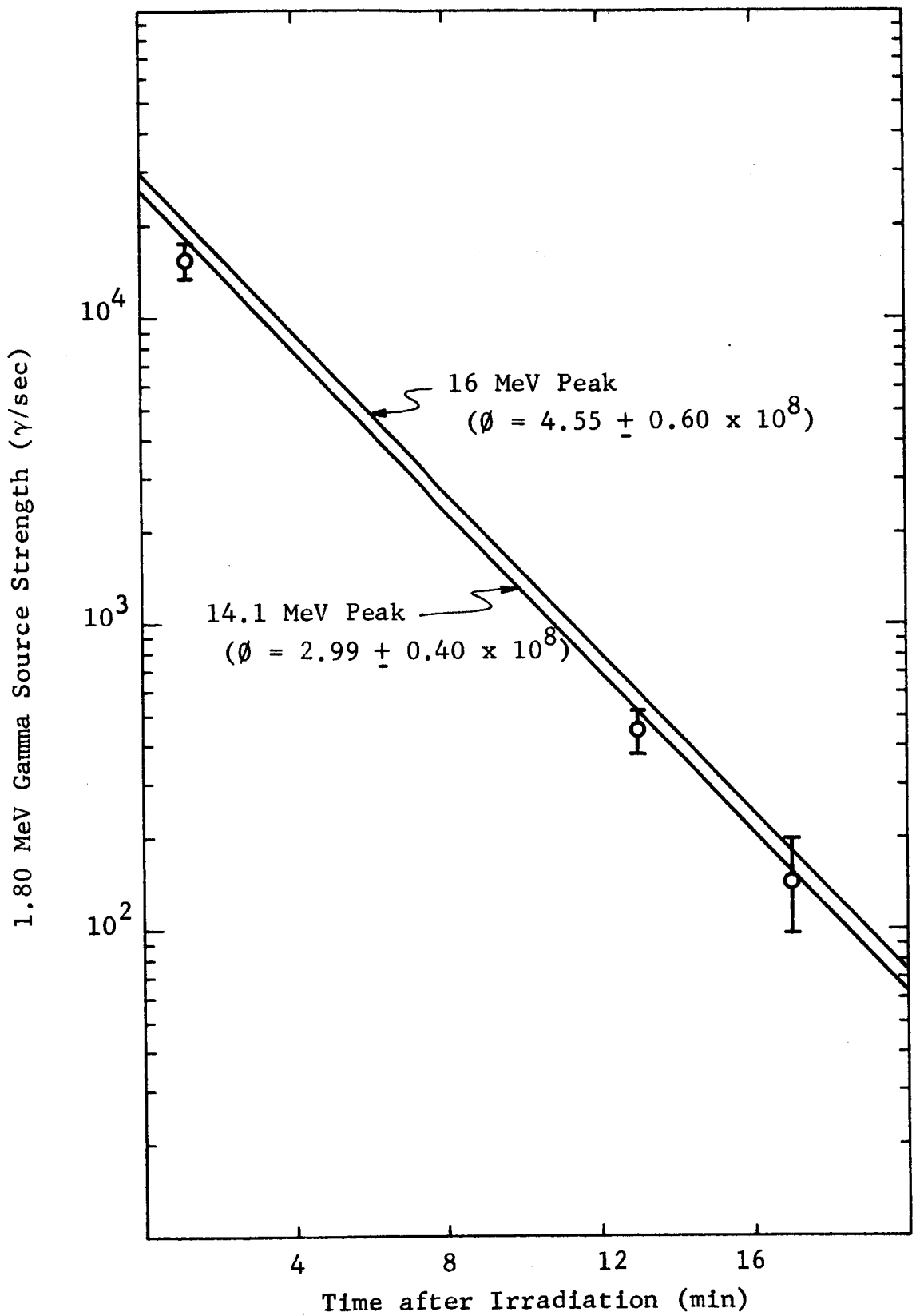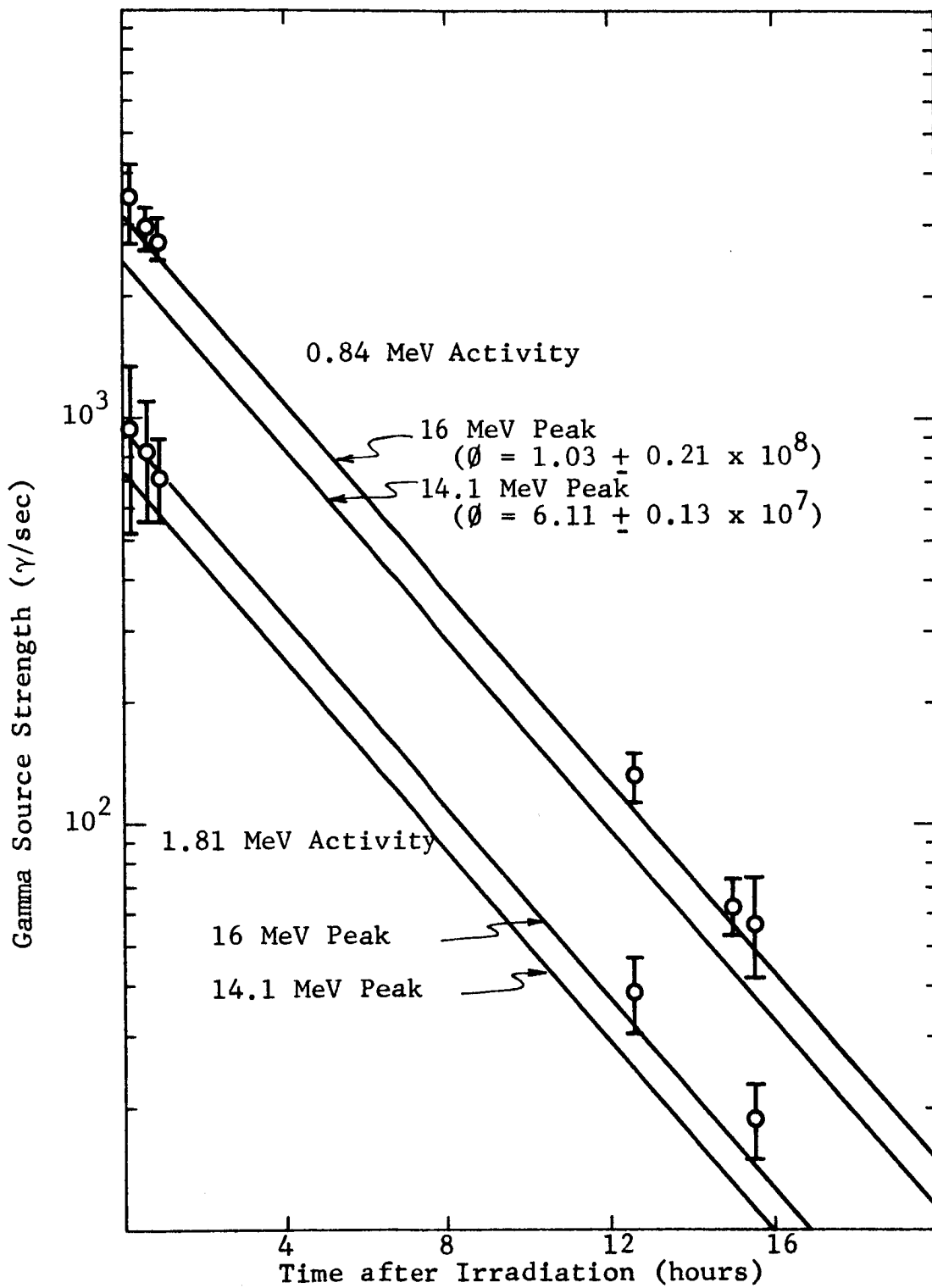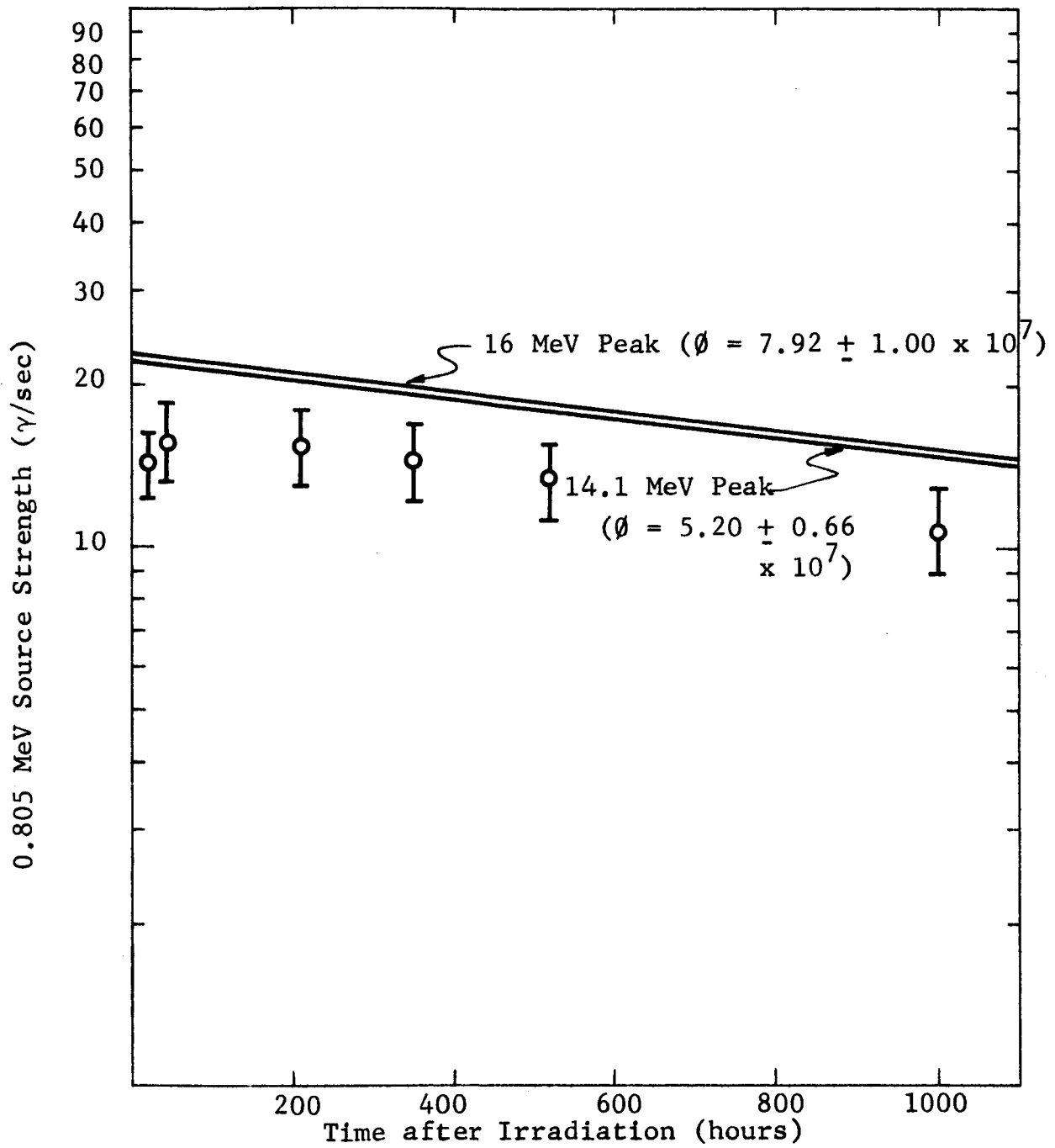
Figure 45

SILICON PILL

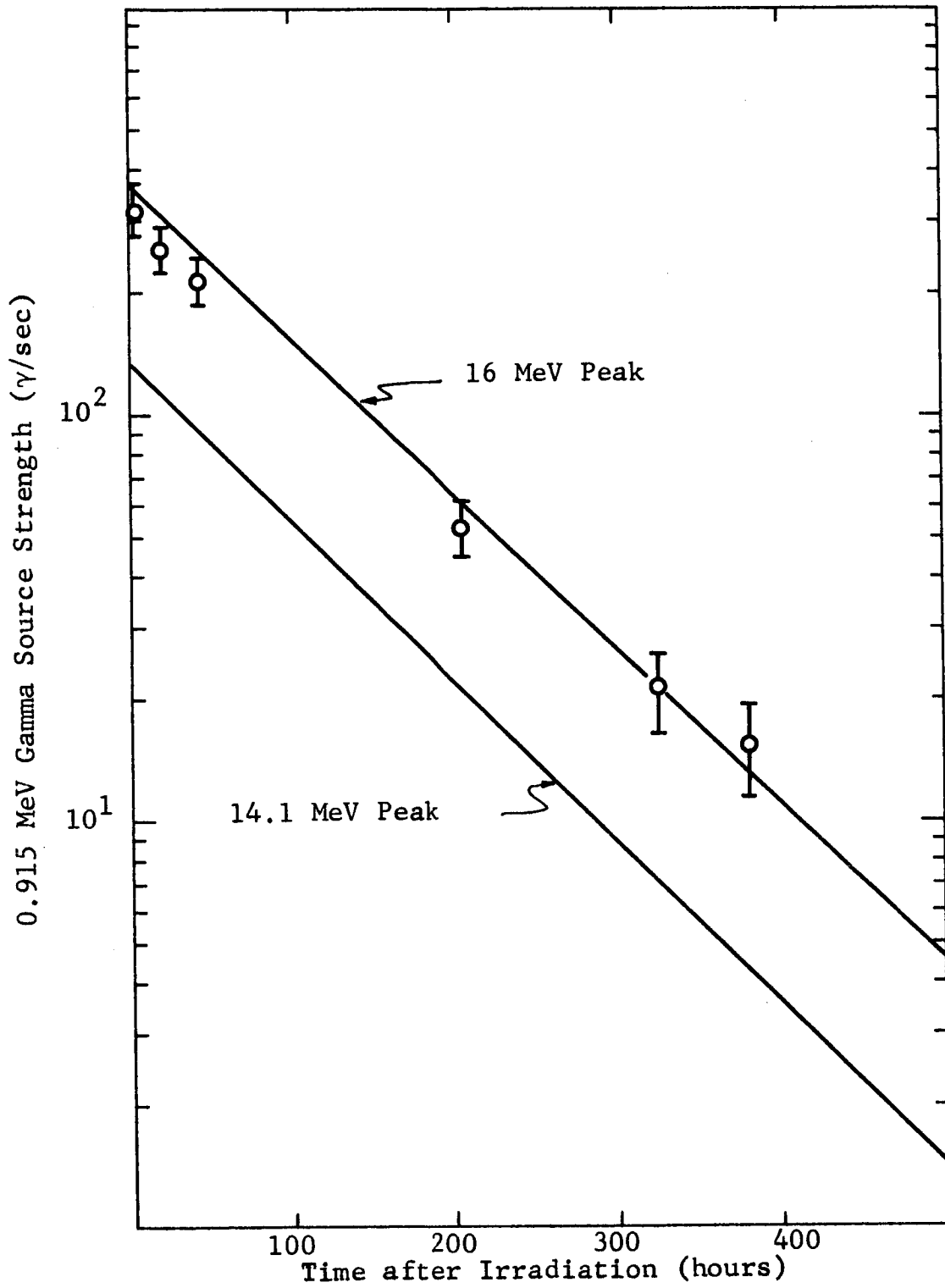Figure 46

IRON FOIL

136

Figure 47
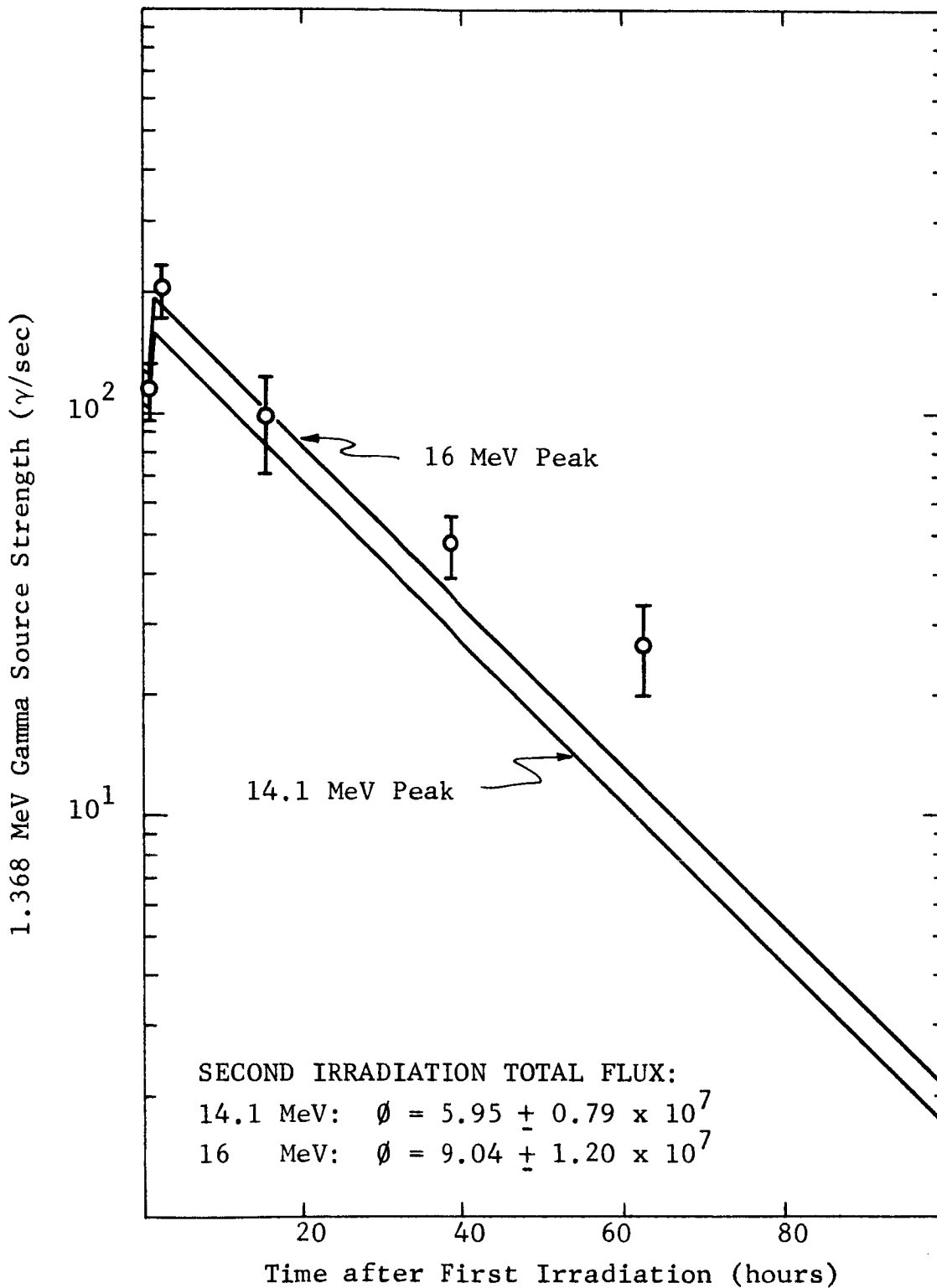
NICKEL FOIL

137

Figure 48
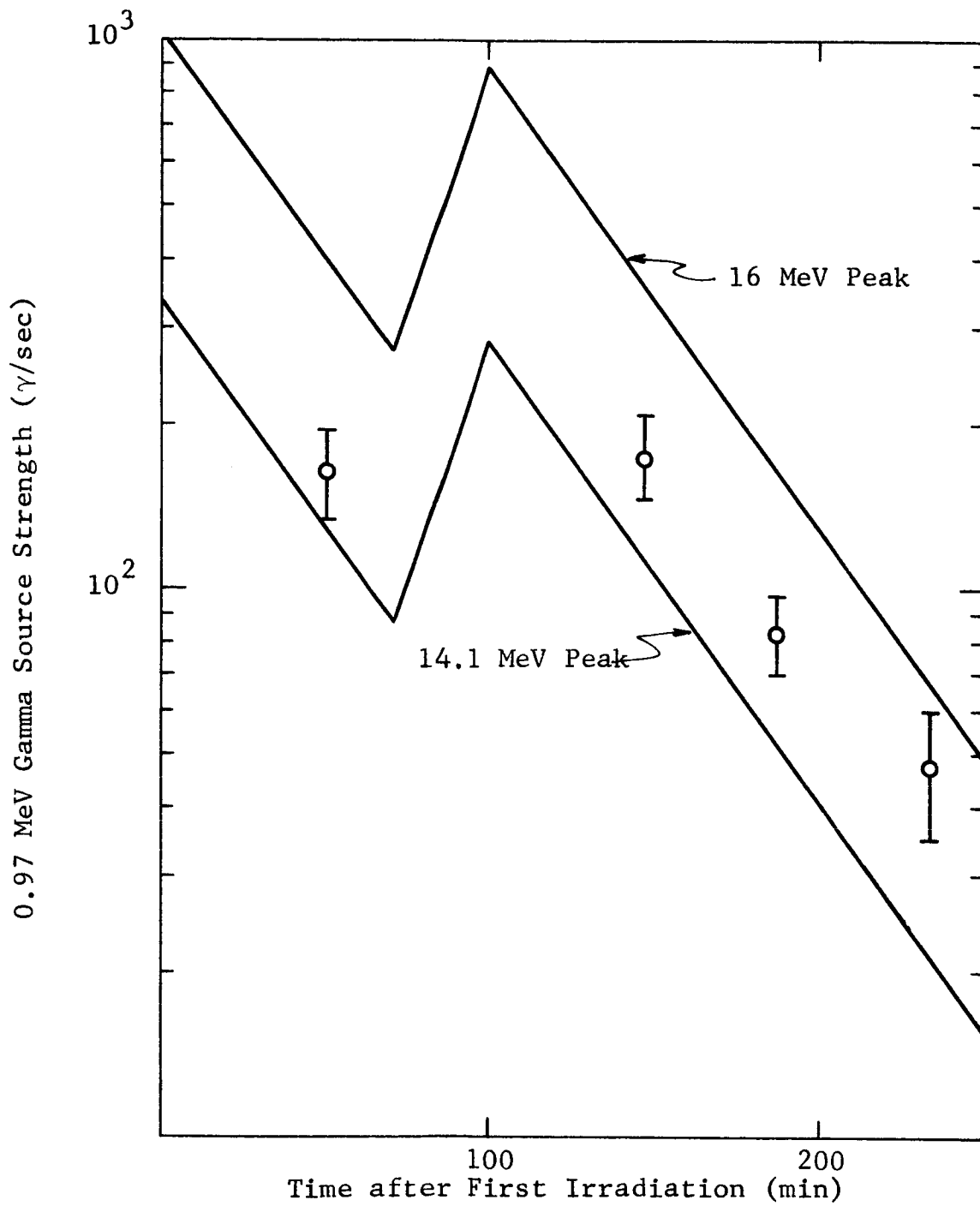
ZIRCONIUM FOIL

Figure 49

MAGNESIUM FOIL

Figure 50

ZINC FOIL

if the spectrum peak is shifted to 14.1 MeV. It appears that accurate knowledge of the energy of the neutron spectrum peak would not alter materially the reported agreement between NAP calculations and the measured gamma activities.

In concluding this last section dealing specifically with comparisons of NAP calculations to experimental data, a few recapitulations are appropriate. The NAP computer program has been shown to provide reliable and accurate neutron-induced activation data for a variety of materials exposed to significantly different neutron flux spectra, including the case of non-uniform cyclic irradiation. It has also been shown that both thermal and resonance neutron self-shielding effects can be accounted for adequately. In those cases where the required neutron reaction cross sections are unknown, the NAP program can provide reasonable, and in many instances accurate, estimation of the necessary cross sections. However, gamma ray activities calculated by use of the NAP code can be no more accurate than the description of the incident neutron flux supplied to the program, the reaction cross sections provided by the program, the library, or the user, and the decay scheme data supplied by the library. The NAP Cross Section Library and the NAP Gamma Radiation Library have been constructed in as comprehensive and accurate a manner as possible within the temporal and financial constraints of the research program. For these reasons, use of the NAP program does not guarantee accurate neutron-induced gamma ray activation calculations. For well-known incident fluxes, well-known reaction cross sections, and well-known decay scheme data, the NAP program has been proven to provide a comprehensive, flexible, reliable, and accurate computation of neutron-induced activation.

b.) Measurement of Gamma Ray Activities

This section describes the procedure used in obtaining the measured gamma ray activities which are compared to NAP

141

calculations in the preceding section. Measured data for the silicon pill and the iron, nickel, zirconium, magnesium, and zinc foils are given. Measured data for the aluminum wires used for flux monitoring are given in the next section.

As stated above, the samples were irradiated while placed on the back of the target holder, along the axis of the deuteron beam. After irradiation, each sample was removed from the Van de Graaff room and taken to an adjacent room for gamma-counting. A lead cave, identical in construction to that described in Section III-C-1-b, was used to reduce the extraneous background. The same 3 x 3 inch NaI crystal used in detecting gamma ray activity of the reactor-irradiated foils was utilized in these experiments. To increase the counting system efficiency, the samples were placed two centimeters above the face of the crystal during counting, rather than ten centimeters as used in the reactor experiments. The same beta absorber and the same 512-channel analyzer were used in all experiments.

The procedures for photopeak analysis were identical, in every respect, to those described in detail in Section III-C-1-b. The counting efficiencies, and associated factors, are given in Table 24. Measured data obtained for each sample are given in Tables 25 through 30. In each case, the peak area, background, and source strength are shown with their associated standard error (deviation).

c.) Determination of Neutron Flux

This section discusses the calculation of the neutron flux energy spectrum incident upon the samples in the Van de Graaff experiments, and the experimental determination of the total flux.

The flux spectrum was calculated by an approximate method suggested by Ricci (ref. 41). Ricci's method has been extended to include inelastic scattering effects. The irradiated samples

Table 24

EFFICIENCIES AND TRANSMISSION FACTORS

Sample (γ Energy)	Detection Efficiency	Transmission Factors			Peak-to-Total Ratio	Counting Efficiency
		Lucite	Cap	Foil		
Si(1.8 MeV)	0.104(6)	0.927(3.4)	0.988(1.5)	0.974(1.7)	0.291(2)	0.0269(7.5)
Fe(0.84 MeV)	0.132(5)	0.903(4.4)	0.981(1.5)	0.952(2.0)	0.457(2)	0.0509(7.4)
Fe(1.81 MeV)	0.103(6)	0.927(3.4)	0.990(1.5)	0.961(1.9)	0.290(2)	0.0263(7.6)
Ni(0.805 MeV)	0.134(5)	0.887(4.4)	0.981(1.5)	0.931(2.2)	0.482(2)	0.0523(7.5)
Zr(0.915 MeV)	0.128(5)	0.903(4.3)	0.980(1.5)	0.945(2.1)	0.438(2)	0.0469(7.4)
Mg(1.368 MeV)	0.112(6)	0.917(4.0)	0.990(1.5)	0.972(1.8)	0.348(2)	0.0339(7.2)
Zn(0.97 MeV)	0.125(5)	0.905(4.3)	0.985(1.5)	0.947(2.0)	0.421(2)	0.0444(7.3)

Note: Values enclosed by parentheses indicate assumed standard error in percent.

143

Table 25

MEASURED ACTIVITY - SILICON PILL

Time After Irradiation (min)	Peak Area (γ/min)	Background (γ/min)	1.80 MeV Source Strength (10^3 γ/sec)
1.25	21240 $\pm$ 168	1858 $\pm$ 56	924 $\pm$ 68
13.00	624 $\pm$ 31	54 $\pm$ 15	27.1 $\pm$ 2.4
17.00	205 $\pm$ 42	62 $\pm$ 38	8.88 $\pm$ 1.94

Table 26

MEASURED ACTIVITY - IRON FOIL

Time after Irradiation (hours)	Peak Area (γ/min)	Background (γ/min)	Source Strength (γ/sec)
	0.84 MeV Activity		
0.183	2650 $+$ 348	516 $+$ 347	3480 $+$ 526
0.550	2245 $+$ 77	349 $+$ 72	2947 $+$ 240
0.875	2105 $+$ 54	277 $+$ 49	2764 $+$ 216
12.21	404 $+$ 21	105 $+$ 17	134 $+$ 12
15.03	190 $+$ 13	98 $+$ 38	63.0 $+$ 6.2
15.48	147 $+$ 11	94 $+$ 11	57.7 $+$ 6.1
	1.81 MeV Activity		
0.183	374 $+$ 99	172 $+$ 98	934 $+$ 256
0.550	340 $+$ 63	119 $+$ 62	825 $+$ 170
0.875	290 $+$ 39	100 $+$ 38	707 $+$ 112
12.21	61.2 $+$ 7.0	41.8 $+$ 3.8	38.5 $+$ 5.3
15.48	25.4 $+$ 3.5	18.7 $+$ 2.9	18.9 $+$ 2.7

Table 27

MEASURED ACTIVITY - NICKEL FOIL

Time after Irradiation (hours)	Peak Area (γ/min)	Background (γ/min)	0.805 MeV Source Strength (γ/sec)
21.08	44.4 ± 1.7	113.7 ± 1.5	14.2 ± 1.2
45.85	49.3 ± 3.2	110.9 ± 3.1	15.7 ± 1.6
213.17	48.2 ± 3.1	84.4 ± 3.1	15.4 ± 1.5
349.35	45.9 ± 3.1	81.6 ± 3.1	14.6 ± 1.5
521.87	42.4 ± 2.5	73.0 ± 2.5	13.5 ± 1.3
1003.05	34.2 ± 2.5	69.0 ± 2.5	10.9 ± 1.2

Table 28

MEASURED ACTIVITY - ZIRCONIUM FOIL

Time after Irradiation (hours)	Peak Area (γ/min)	Background (γ/min)	0.915 MeV Source Strength (γ/sec)
2.98	890 $\pm$ 28	147 $\pm$ 23	315 $\pm$ 25
19.08	715 $\pm$ 16	101 $\pm$ 16	256 $\pm$ 19
42.05	603 $\pm$ 15	86 $\pm$ 13	215 $\pm$ 16
206.18	145 $\pm$ 9	76 $\pm$ 9	53.2 $\pm$ 5.0
325.27	56.7 $\pm$ 6.4	67.2 $\pm$ 6.3	21.4 $\pm$ 2.8
378.92	41.0 $\pm$ 5.7	67.4 $\pm$ 5.6	15.4 $\pm$ 2.4

Table 29

MEASURED ACTIVITY - MAGNESIUM FOIL

Time after First Irrad. (hours)	Peak Area (γ/min)	Background (γ/min)	1.368 MeV Source Strength (γ/sec)
0.984	232 $\pm$ 15	142 $\pm$ 10	114 $\pm$ 11
2.627	410 $\pm$ 25	132 $\pm$ 22	202 $\pm$ 18
15.533	186 $\pm$ 29	104 $\pm$ 15	99.0 $\pm$ 16.8
38.550	95.6 $\pm$ 8.7	64.4 $\pm$ 8.0	47.4 $\pm$ 5.3
62.484	50.5 $\pm$ 7.2	43.9 $\pm$ 7.0	26.8 $\pm$ 4.2

Table 30

MEASURED ACTIVITY - ZINC FOIL

Time after First Irrad. (min)	Peak Area (γ/min)	Background (γ/min)	0.97 MeV Source Strength (γ/sec)
50.5	420 ± 37	432 ± 32	164 ± 19
147.0	439 ± 46	388 ± 42	172 ± 22
187.0	205 ± 18	219 ± 15	83.5 ± 9.4
234.0	87.5 ± 12.5	151 ± 12	47.2 ± 7.5

were assumed to be cylindrical discs attached to the center of the rear face of the target holder. The deuteron beam was assumed to be cylindrical, 0.25 inch in diameter, with axis normal to the tritium target at its center. The deuteron energy was 600 keV. The target holder was assumed to be iron of thickness 0.25 inch, and the water coolant between the tritium target and the target holder was assumed to be 0.875 inch thick. The neutrons which reach the sample are conceptually divided into six groups. These are non-scattered (or direct) neutrons directly from the tritium target, neutrons that reach the sample after a single elastic scattering collision with hydrogen, oxygen, or iron nuclei, and neutrons that reach the sample after a single inelastic scattering collision with oxygen or iron nuclei. The incident neutron spectrum was estimated by a consideration of the energy range for each of these six groups, and the relative abundance of neutrons in each of these six groups.

The energy range of the direct neutrons was obtained from the energy balance in the $T(d,n)He^4$ reaction and the solid angle subtended, at the target, by the sample. Thus the direct neutrons which reach the sample lie in the energy range from 15.98 to 16.03 MeV, assuming a thin target. For elastic scattering, the energy E' of the scattered neutron is related to the energy E of the incident neutron and the scattering angle θ by

$$E' = E \ \frac{A^2 + 2A\cos\theta + 1}{(A+1)^2} \tag{115}$$

where A is the mass of the scatterer. From known elastic scattering angular distributions, it is found that essentially all of the neutrons scattered by oxygen nuclei have $\theta \leqslant 60°$, essentially all of the neutrons scattered by iron nuclei have $\theta \leqslant 37°$, and all angles are possible for scattering by hydrogen nuclei. These maximum scattering angles, together with geo-

150

metrical considerations, permitted a determination of the
maximum angles to the normal with which a neutron can be
emitted from the tritium target and reach the sample after a
single elastic scattering. This, in turn, permitted calcu-
lation of the minimum energy of neutrons reaching the sample
after a single elastic scattering collision. Thus, neutrons
reaching the sample after a single elastic scattering collision
with an iron nucleus have an energy range from 15.80 to 16.03
MeV, neutrons reaching the sample after a single elastic
scattering with an oxygen nucleus have an energy range from
13.47 to 16.03 MeV, and neutrons reaching the sample after a
single collision with an hydrogen nucleus have an energy range
from zero to 16.03 MeV. For the iron and oxygen elastic
scattering, the number of neutrons reaching the sample was
assumed to be proportional to their energies, because the prob-
ability for scattering by these elements increases sharply
for small values of θ, leading to high energies E'.

For inelastic scattering, the scattered neutron emission
was assumed to be isotropic. If the neutrons emerging from
the tritium target are regarded as monoenergetic, and if the
energy spectrum is divided into small energy intervals of
width ΔE_j, then the relative probability that an inelastically
scattered neutron will have an energy, after scattering, in
the interval ΔE_j is (ref. 42)

$$f_j = \frac{E_j \exp(-E_j/T) \Delta E_j}{T^2}$$

(116)

where E_j is the average energy in the interval ΔE_j, and T is
the nuclear temperature of the residual nucleus at the incident
energy (16 MeV). The integral of f_j over all energy E_j is
unity. The nuclear temperature was taken as (ref. 42),

$$T = \frac{2}{B} \sqrt{16 \text{ MeV}}$$

(117)

151

with B approximately 0.62 $A^{1/2}$, where A is the mass number. In the calculation described here, the ΔE_j have been taken as 0.5 MeV.

Following Ricci, the relative abundance of the six neutrons groups (direct, iron elastic scattering, iron inelastic scattering, etc.) that reach the sample are given by

$$F_x = \frac{P_{s,x} \, P_{g,x}}{\sum\limits_x P_{s,x} P_{g,x}} \tag{118}$$

Here x signifies the group (direct, iron elastic scattering, etc.), $P_{s,x}$ is the probability that one of the neutrons emitted from the tritium target is involved in the event specified by x, and $P_{g,x}$ is the probability that a neutron reaches the sample from the point where the collision took place or from the point where the neutron was emitted. The probability $P_{s,x}$ is taken as

$$P_{s,x} = 1 - \exp(-N_x \sigma_x d_x) \tag{119}$$

where N_x is the number of nuclei of element x per unit volume, σ_x is taken as the appropriate scattering cross section for 16 MeV neutrons, and d_x is an average distance travelled by a neutron through the element x. The probability $P_{g,x}$ is taken as

$$P_{g,x} = \frac{\Omega_x}{4\pi} \tag{120}$$

where the solid angle Ω_x is approximated by the solid angle, at the center of the medium x, subtended by the sample. The results of these calculations are summarized in Table 31. By combining these relative abundance values with the previously calculated energy ranges, the neutron spectrum given previously in Table 25 is obtained.

152

Table 31

VAN DE GRAAFF NEUTRON RELATIVE ABUNDANCES

Type of Scattering Event	$P_{s,x}$	$P_{g,x}$	Relative Abundance F_x
Direct	1.0	0.00305	0.115
Ox-elastic	0.0564	0.008	0.0170
Ox-inelastic	0.0382	0.008	0.0115
Fe-elastic	0.0587	0.146	0.323
Fe-inelastic	0.0919	0.146	0.507
Hydrogen	0.0876	0.008	0.0264

The calculation described above yields a relative neutron energy spectrum. The absolute magnitude of the flux must be determined by use of flux monitor samples during the irradiation. Aluminum wires, whose gross physical properties have been summarized in Table 22, were used as flux monitors during the Van de Graaff irradiations. These flux monitors were gamma-counted in exactly the same manner as the other samples. The appropriate efficiencies and transmission factors are given in Table 32. Since all four aluminum wires were the same thickness, and approximately the same area, the detection efficiency, "foil" transmission factor, and counting efficiency was identical for all wires, for a given gamma ray energy. The measured activities are summarized in Tables 33 through 36.

Figures 51 through 54 show the extent to which the measured activities are fitted by the derived values of the total flux. The total flux values shown on the figures were derived from NAP calculations using the standard NAP Cross Section Library. Use of the alternate cross section sets discussed above, representing neutron spectrum peaks at 14.1 and 16 MeV, does not change the agreement between the NAP calculations and measured activities shown in Figures 51 through 54. The total flux values are changed, however, by use of the alternate cross section sets. In principle, the results of the relative neutron spectrum calculation given above are not valid if the neutrons emitted in the $T(d,n)He^4$ reaction have an energy of 14.1 MeV. The resultant changes in the relative neutron spectrum have been regarded as a second order effect, and thus all NAP calculations pertaining to the Van de Graaff experiments were performed using the flux spectrum given in Table 23.

154

Table 32

ALUMINUM WIRE DETECTION EFFICIENCIES

Quantity	Gamma Ray Energy		
	0.842 MeV	1.01 MeV	1.368 MeV
Detection Efficiency	0.127(5)	0.118(5)	0.109(6)
Lucite Trans. Factor	0.902(4.4)	0.907(4.3)	0.917(4.0)
Cap Trans. Factor	0.970(1.5)	0.985(1.5)	0.990(1.5)
Foil Trans. Factor	0.990(1.6)	0.990(1.6)	0.990(1.6)
Peak-to-Total Ratio	0.460(2)	0.412(2)	0.343(2)
Counting Efficiency	0.0506(7.3)	0.0431(7.2)	0.0335(7.8)

Note: Values enclosed by parentheses indicate assumed standard error in percent.

Table 33

MEASURED ACTIVITY-AL WIRE #1

Time after Irradiation (min)	Peak Area ($10^3\gamma$/min)	Background ($10^3\gamma$/min)	Source Strength ($10^3\gamma$/min)
	0.842 MeV Activity		
7.00	27.1 ± 1.0	4.27 ± 1.01	9.31 ± 0.76
21.50	9.53 ± 0.46	2.05 ± 0.44	3.27 ± 0.29
31.50	4.74 ± 0.30	1.39 ± 0.29	1.62 ± 0.16
	1.01 MeV Activity		
7.00	8.90 ± 0.42	1.49 ± 0.41	3.59 ± 0.31
21.50	3.43 ± 0.14	0.902 ± 0.118	1.38 ± 0.11
31.50	1.75 ± 0.16	0.822 ± 0.150	0.701 ± 0.081
	1.368 MeV Activity		
7.00	0.931 ± 0.054	0.458 ± 0.033	0.463 ± 0.045
21.50	0.961 ± 0.066	0.424 ± 0.051	0.478 ± 0.050
31.50	1.06 ± 0.06	0.402 ± 0.037	0.528 ± 0.051

Table 34

MEASURED ACTIVITY-AL WIRE #2

Time after Irradiation (min)	Peak Area (γ/min)	Background (γ/min)	Source Strength (γ/min)
0.842 MeV Activity			
3.00	14810 $\pm$ 460	2780 $\pm$ 440	5077 $\pm$ 343
27.00	2639 $\pm$ 229	1090 $\pm$ 65	903 $\pm$ 95
37.50	1263 $\pm$ 107	928 $\pm$ 8	431 $\pm$ 45
1.01 MeV Activity			
3.00	5059 $\pm$ 383	1138 $\pm$ 373	2037 $\pm$ 204
27.00	1176 $\pm$ 221	756 $\pm$ 215	473 $\pm$ 94
37.50	839 $\pm$ 194	640 $\pm$ 188	337 $\pm$ 81

Table 35

MEASURED ACTIVITY-AL WIRE #3

Time after Irradiation (min)	Peak Area (γ/min)	Background (γ/min)	Source Strength (γ/min)
0.842 MeV Activity			
13.00	4466 $\pm$ 182	1182 $\pm$ 172	1588 $\pm$ 115
27.00	1541 $\pm$ 40	768 $\pm$ 9	548 $\pm$ 36
42.00	490 $\pm$ 32	462 $\pm$ 26	188 $\pm$ 13
1.01 MeV Activity			
13.00	1470 $\pm$ 55	665 $\pm$ 40	614 $\pm$ 44
27.00	542 $\pm$ 48	612 $\pm$ 38	226 $\pm$ 25
42.00	279 $\pm$ 26	476 $\pm$ 18	125 $\pm$ 14
1.368 MeV Activity			
13.00	816 $\pm$ 30	303 $\pm$ 12	406 $\pm$ 30
27.00	732 $\pm$ 28	281 $\pm$ 10	364 $\pm$ 27
42.00	775 $\pm$ 32	248 $\pm$ 27	386 $\pm$ 30

$\emptyset = 3.55 \pm 0.47 \times 10^8$

0.842 MeV

1.01 MeV

1.368 MeV

Figure 51

AL WIRE #1

$$\emptyset = 7.8 \pm 1.6 \times 10^7$$

0.842 MeV

1.01 MeV

Figure 52

AL WIRE #2

$$\emptyset = 6.17 \pm 0.78 \times 10^{7}$$

0.842 MeV

1.01 MeV

1.368 MeV

Gamma Source Strength (γ/sec)

Time after Irradiation (min)
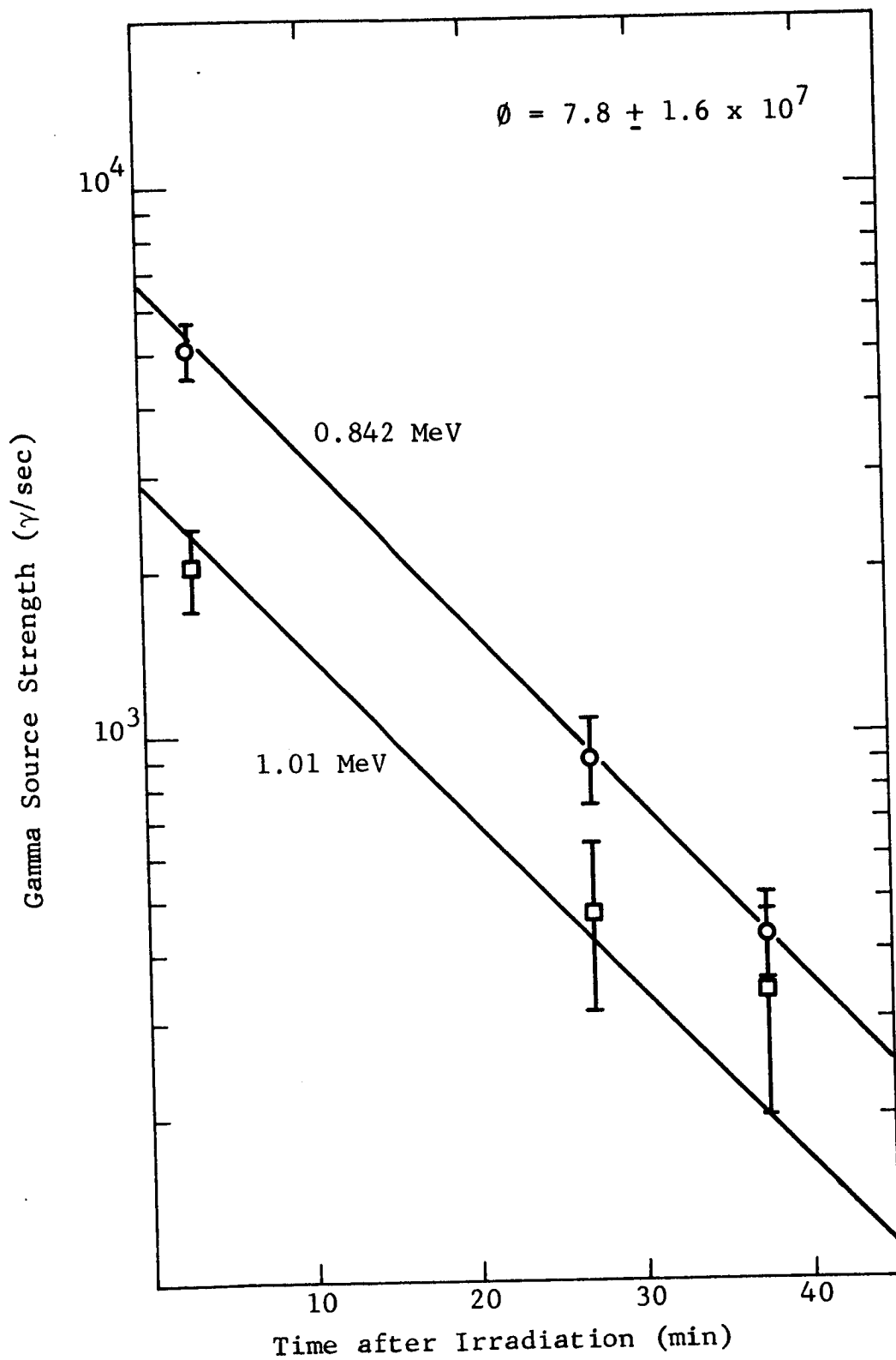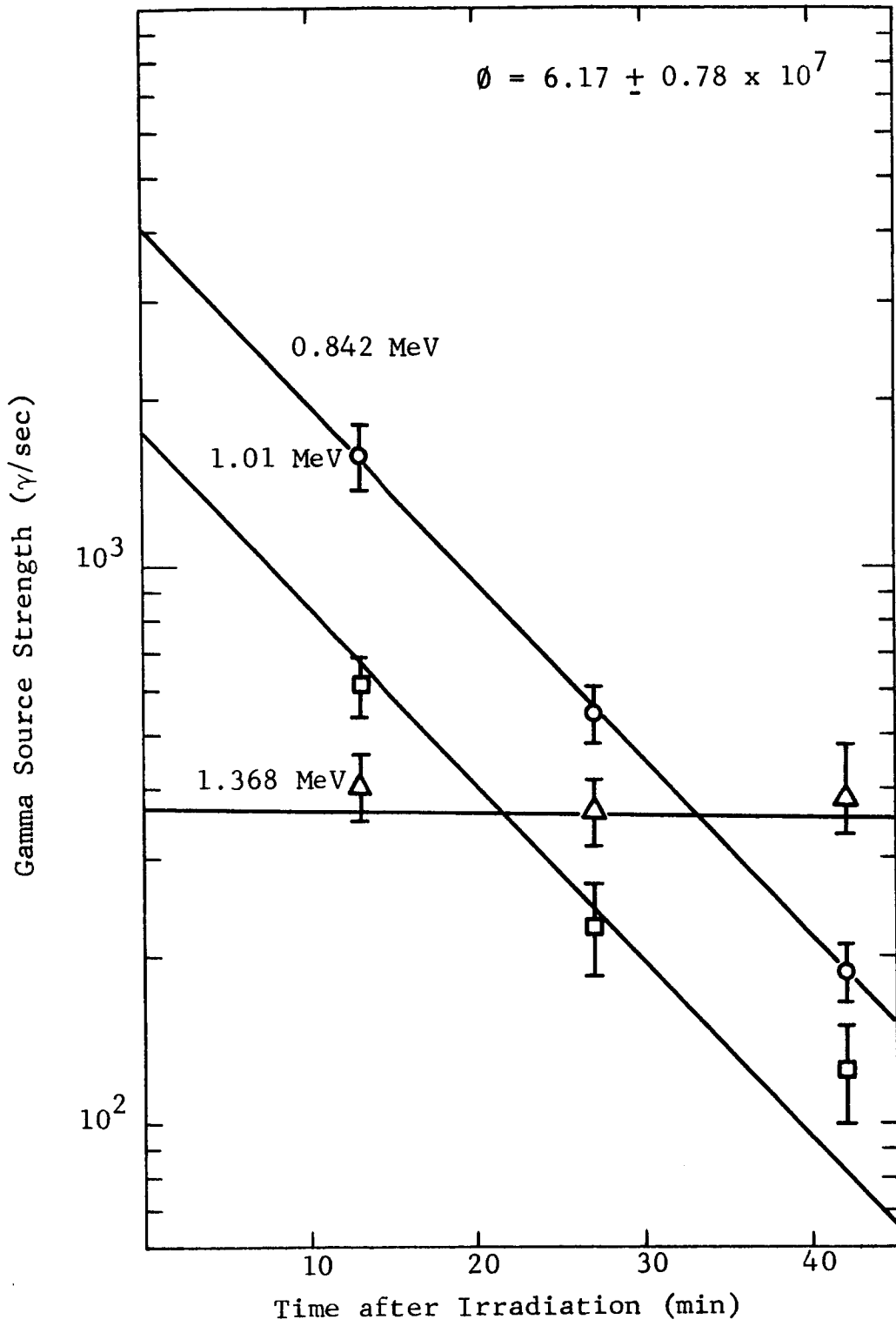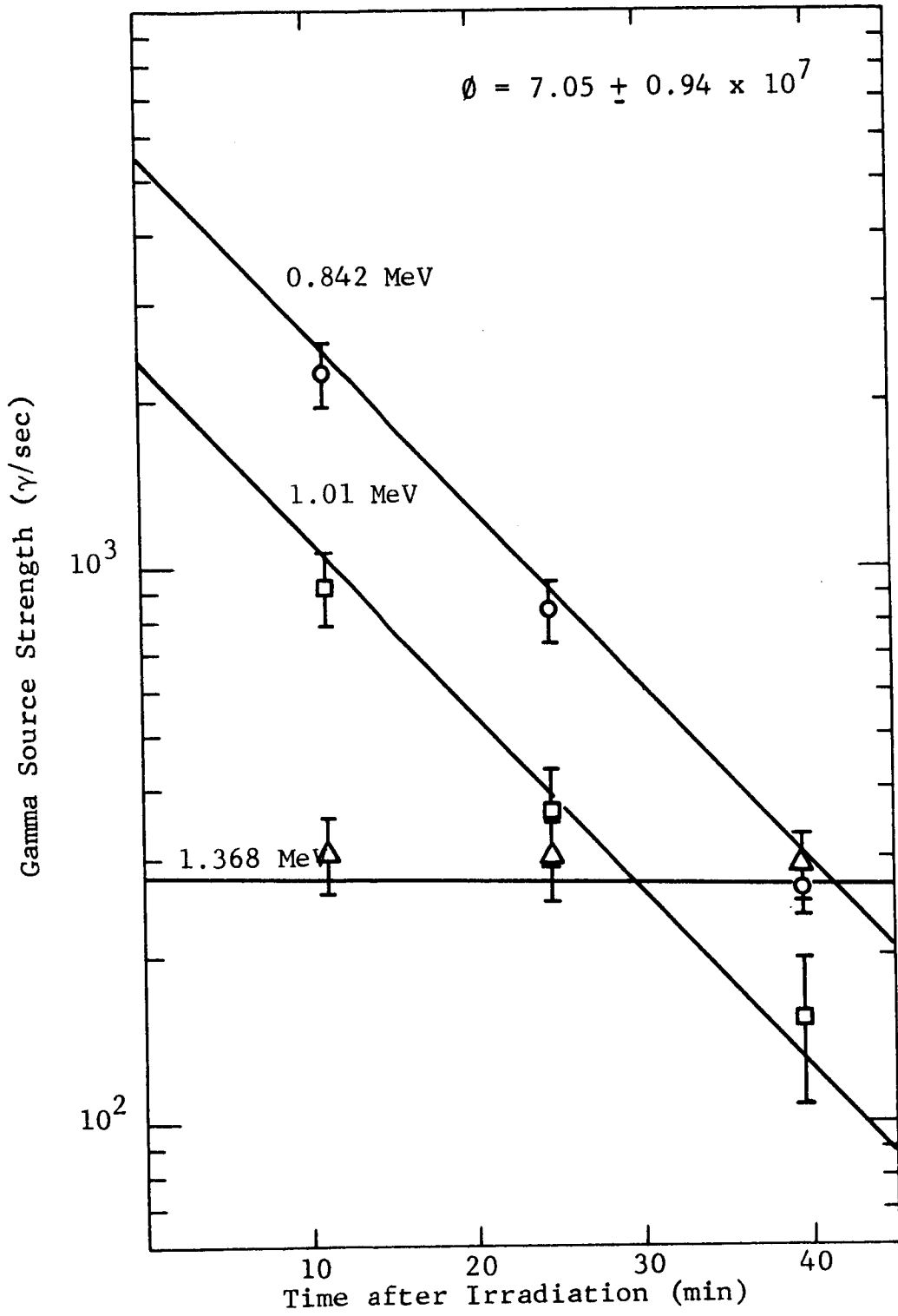
Figure 53

AL WIRE #3

161
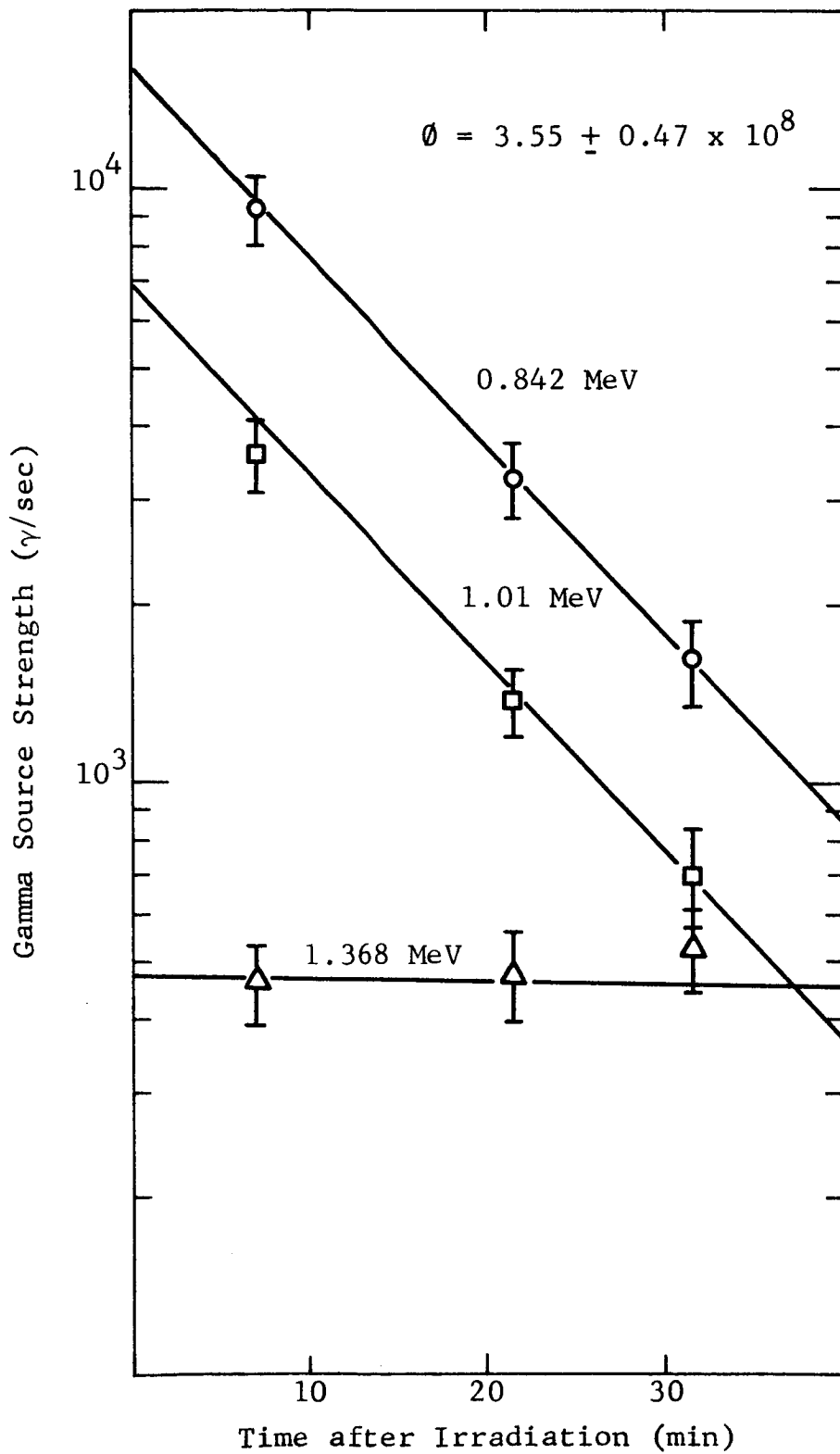
Figure 54

AL WIRE #4

Table 36

MEASURED ACTIVITY-AL WIRE #4

Time after Irradiation (min)	Peak Area (γ/min)	Background (γ/min)	Source Strength (γ/min)
0.842 MeV Activity			
11.00	6310 + 168	1110 + 154	2246 + 148
24.50	2366 + 83	686 + 71	841 + 59
39.50	692 + 23	476 + 11	265 + 17
1.01 MeV Activity			
11.00	2214 + 111	606 + 103	925 + 77
24.50	872 + 66	464 + 58	364 + 38
39.50	338 + 48	409 + 45	152 + 24
1.368 MeV Activity			
11.00	616 + 36	242 + 27	307 + 27
24.50	606 + 29	208 + 19	302 + 24
39.50	582 + 19	198 + 11	290 + 21

REFERENCES

1. A. M. Weinberg and E. P. Wigner, The Physical Theory of Neutron Chain Reactors, University of Chicago Press (1958).

2. B. Davison, Neutron Transport Theory, Oxford University Press, London (1957).

3. B. G. Carlson, Solution of the Transport Equation by S_n Approximations, AEC Report LA-1891 (1953).

4. G. C. Wick, Zeits. f. Physik, 121, 702 (1943).

5. S. Chandrasekhar, Radiative Transfer, Oxford University Press, London (1950).

6. H. S. Wilf, The Transmission of Neutrons in Multilayered Slab Geometry, Nucl. Sci. and Engr., 5, 306 (1959).

7. G. Goertzel, The Method of Discrete Ordinates, Nucl. Sci. and Engr., 4, 581 (1958).

8. J. M. Blatt and V. F. Weisskopf, Theoretical Nuclear Physics, John Wiley and Sons, Inc., New York (1952).

9. R. G. Moore, Jr., Nuclear Reaction Cross Section Theory, Rev. Mod. Phys., 32, 101 (1960).

10. J. C. Ringle, A Technique for Measuring Neutron Spectra in the Range 2.5 to 30 MeV Using Threshold Detectors, AEC Report UCRL-10732 (1963).

11. R. E. Bullock and R. G. Moore, Jr., Odd-Even Dependence of Nuclear Level Density Parameters, Phys. Rev. 119, 721 (1960).

12. M. El-Nadi and M. Wafik, Nuclear Level Density in Proceedings of the Second United Nations International Conference on the Peaceful Uses of Atomic Energy, 14, 54, United Nations, Geneva (1958).

13. J. Wing and J. D. Varley, Calculated Values of Wing-Fong's Nuclidic Mass Equation, AEC Report ANL-6886 (1964).

14. L. Dresner, Resonance Absorption in Nuclear Reactors, Pergamon Press, New York (1960).

15. G. Doherty, An Approximation to the Doppler Broadened Function $J(\theta,\beta)$. Australian AEC Report AAEC/TM 196 (1963).

16. S. Podgor and L. A. Beach, Regularities in Thermal Neutron Absorption Cross Sections, NRL Report 6124 (1964).

17. D. J. Hughes, B. A. Magurno, and M. K. Brussel, Neutron Cross Sections, AEC Report BNL-325, Second Edition, Supplement No. 1 (1960).

18. H. Newson, Neutron Resonance Phenomena in Progress in Fast Neutron Physics edited by J. B. Marion and J. R. Risser, University of Chicago Press (1963).

19. D. R. Vondy, Development of a General Method of Explicit Solution to the Nuclear Chain Equations for Digital Machine Calculations, AEC Report ORNL-TM-361 (1962).

20. Martinez, J.S.: Neutron Self-Shielding in One-Dimensional Absorbers. Aec Report UCRL-6526, 1961.

21. Westcott, C. H.: Effective Cross Section Values for Well-Moderated Thermal Reactor Spectra. Atomic Energy of Canada Limited Report CRRP-787, 1958.

22. Templin, L.S., ed.: Reactor Physics Constants. AEC Report ANL-5800, 2nd Edition, 1963.

23. De Juren, J. A. and Stooksberry, R. W.: Measurement of the O^{16} Cross Section from 11 to 19 MeV. Phys. Rev. 127, 1229 (1962).

24. Stehn, J. R. et al.: Neutron Cross Sections, Volume I, $Z = 1$ to 20. AEC Report BNL-325, Second Edition, Supplement No. 2, 1964.

25. Forbes, S. G.: Phys. Rev. 88, 1309 (1956).

26. Barry, J. F.: The Cross Section of the Ni^{58} (n,p)Co^{58} Reaction for Neutrons in the Energy Range 1.6 to 14.7 MeV, J. Nucl. Energy, 16, 467 (1962).

27. Jeronymo, J. M. F. et al.: Nucl. Phys. 47, 157 (1963).

28. Howerton, R. J. et al.: Thresholds of Neutron Induced Reactions. AEC Report UCRL-14000, 1964.

29. Konig, L. A. et al.: Nucl. Phys. <u>31</u>, 18 (1962).

30. Allen, L. et al.: Phys. Rev. <u>107</u>, 1363 (1957).

31. Mani, G. S. et al.: Nucl. Phys. <u>19</u>, 535 (1960).

32. Hughes, D. J. and Schwartz, R. B.: Neutron Cross Sections, AEC Report BNL-325, Second Edition, 1958.

33. Rayburn, L. A.: (n,2n) Reaction Cross Sections from 12 to 19 MeV, Phys. Rev. <u>130</u>, 731 (1963).

34. Martin, H. C. and Taschek, R. F.: Phys. Rev. <u>88</u>, 1302 (1953).

35. S. C. Choy and R. A. Schmitt, Gamma-Ray Spectra Analyzed by Computer Program Using the Peak Area Method, GA-5233, August 10, 1964.

36. R. L. Heath, "Scintillation Spectrometry, Gamma-Ray Spectrum Catalogue,: IDO-16880-1, August 1964.

37. Lewis, W. B.: Radiation from Neutron-Activated Slabs and Spheres. Nucleonics, Vol. 15, No. 4, p. 84, 1957.

38. Hassitt, A.: A Computer Program to Solve the Multi-Group Diffusion Equations. UKAEA Report TRG 229, 1962.

39. Joanou, G. D. and Dudek, J. S.: GAM-1, A Consistent P_1 Multigroup Code for the Calculation of Fast Neutron Spectra and Multigroup Constants. AEC Report GA-1850, 1961.

40. Shudde, R.: TEMPEST-II. NAA Program Description, 1961.

41. Ricci, E.: Output Spectrum from 14-MeV Neutron Generators. J. Inorg. Nucl. Chem. Vol. 27, pp. 41-52, 1965.

42. W. Yiftah, S., Okrent, D., and Moldauer, P. A.: Fast Reactor Cross Sections. Pergamon Press, New York, 1960.